Experimental and Theoretical Investigation of Catalyst Poisoning and Regeneration During Biogas Steam Reforming on Nickel

Srinivas Appari

A Thesis Submitted to

Indian Institute of Technology Hyderabad

In Partial Fulfillment of the Requirements for

The Degree of Doctor of Philosophy

Department of Chemical Engineering

February 2014

Declaration

I declare that this written submission represents my ideas in my own words, and where ideas or words of others have been included, I have adequately cited and referenced the original sources. I also declare that I have adhered to all principles of academic honesty and integrity and have not misrepresented or fabricated or falsified any idea/data/fact/source in my submission. I understand that any violation of the above will be a cause for disciplinary action by the Institute and can also evoke penal action from the sources that have thus not been properly cited, or from whom proper permission has not been taken when needed.

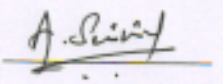

(Signature)

(Srinivas Appari)

CH09P003

(Roll No.)

Approval Sheet

This thesis entitled **Experimental and theoretical investigation of catalyst poisoning and regeneration during biogas steam reforming on nickel** by **Srinivas Appari** is approved for the degree of Doctor of Philosophy from IIT Hyderabad.

6/2/14

(Prof. Deepak Kunzru) Examiner

Department of Chemical Engineering, IIT Kanpur

06/02/2014

(Prof. Kamal K. Pant) Examiner

Department of Chemical Engineering, IIT Delhi

6/2/14

(Dr Vinod M. Janardhanan) Adviser

Department of Chemical Engineering

IIT Hyderabad

(Dr Dayadeep Monder) Examiner

Department of Chemical Engineering

IIT Hyderabad

6/2/14

(Dr Ch. Subrahmanyam) Chairman

Department of Chemistry

IIT Hyderabad

Acknowledgements

It gives me an immense pleasure to acknowledge my sincere thanks to the people who have helped me directly or indirectly for making this day possible.

I express my sincere gratitude to my research advisor Dr. Vinod M Janardhanan for his valuable guidance, support during my Ph.D program. I am extremely fortunate to have Dr. Vinod as my Ph.D advisor. I would like to express my heartfelt thanks to him for his excellent guidance, encouragement, and continuous support throughout my stay at IITH, without which, I could not have finished this dissertation. It has been an honor to be his first Ph.D student. Working on this project was an excellent opportunity and it was a beautiful trip to the Netherlands to present our work in ISCRE 22. I would like to thank Dr. Vinod for the same. It has been a great learning experience and I am certain it is something that will shape my future.

My devout thanks to Prof. Sreenivas Jayanti, IIT Madras. The cooperation extended by him in a cheerful and friendly manner is always memorable. His inclination and hunger towards research has been a source of inspiration for me.

I am heartily thankful to Dr. Debaprasad Shee, for his support and fruitful discussions on GC calibrations and catalyst characterization techniques during my experimental studies. I would like to thank Dr. Dayadeep Monder, for his revision and important suggestions for last version of my thesis.

I would like to thank my doctoral committee members, Dr. Sunil Kumar Maity, Dr. Debaprasad Shee, and Dr. Subrahmanyam Ch for their insightful comments, valuable suggestions and constructive criticism. I thank to Dr. Kirti Chandra Sahu, Dr. Chandra Shekar Sharma and faculty of chemical engineering department, IITH. My special thanks to Prof. U B Desai (director, IIT Hyderabad) for providing a conducive environment to work during my PhD program.

I would also like to thank all of my publications'co-authors, especially Prof. Olaf Deutchmann, KIT Germany, Prof. Sreenivas Jayanti, and Dr. Ranjit Bauri, IIT Madras.

Special acknowledgements to Sri K. V. Vishnu Raju, Chairman, Sri Vishnu Educational Society, whose encouragement and support during my studies. I thank my previous colleagues Dr. K S N Raju, Dr. M Ramakrishna, Dr. G B Radhika, Dr. M K Verma and Vighneshawara Rao for their valuable suggestions.

Special thanks to Sudhakara Reddy for helping in catalyst characterizations and support during the experimentation. I am fortunate to have good friends, Dr. Ramesh Babu, Ramakrishna Ch, Happy Pandurangam, Anil Kumar P, Dr. Harikishan Reddy, Dr. Kranthi Kumar M, Vandana N, Anitha M, BVRSN Prasad, Ravi kumar G, Atul Meshram, Balaraju V, Vimala D, Prasanna Rani, Praveen Kumar P, V T S R Kumar Reddy, Manohar, V C S Palla, Goutham P, Nageshwara Rao V, and Sweta Rekha Ram, who have been extremely supportive.

My infinite love and thanks are due to my parents, because all what I have accomplished in life is the result of their unconditional love and years of sacrifice. My beloved dad's desire and loving mom's affection drive me to achieve higher heights in my life. I am lucky to be blessed with loving sister Vara Lakshmi

and my uncle Nagarjuna. I am thankful to them and my brother-in-law Srinivas, my nephews Sandeep and Avinash, my in-laws Ganeshwara Rao and Sathyavathi for their affection and encouragement during all my endeavours. My heartfelt gratitude is due to my wife Sujatha and to our loving daughter Satviki for their patience during the years and especially during the past few months.

Finally, I would like to thank the ALMIGHTY for providing this opportunity and helped me in countless ways.

Srinivas Appari

DEDICATION

To

MY BELOVED PARENTS

Nomenclature

a_k	Pre-exponential constant in sticking coefficient expression
a_k^{eq}	Equilibrium activity
A_v	Active surface area (m^2)
A_i	Pre-exponential constant in Arrhenius expression (varies)
A_{CH_4}	Chromotograph area of CH_4 (mm^2)
A_{N_2}	Chromotograph area of N_2 (mm^2)
A_s	Specific area (m^{-1})
b_i	Temperature exponent in sticking coefficient expression
$B_{1/2}$	X-Ray diffraction angle (degrees)
C_p	Specif heat (J kg^{-1} K^{-1})
c_A	Concentration of A (mol m^{-3})
D	Mean size of crystallite (nm)
D_A	Gas phase dissociation energy of molecule A (kJ mol^{-1})
$\mathcal{D}$	Diffusivity (m^2 s^{-1})
$\mathcal{D}_{km}$	Axial dispersion coefficient of species k (m^2 s^{-1})
$\mathcal{D}_{kj}$	Binary diffusivity of species k in j (m^2 s^{-1})
D_0	Initial dispersion in sintering rate expression (m^2 s^{-1})
E_f	Activation energy for forward reaction (kJ mol^{-1})
E_r	Activation energy for reversed reaction (kJ mol^{-1})
F	Molar flow rate (mol min^{-1})
k	Thermal conductivity (J m^{-1} s^{-1} K^{-1})
r_{Ai}	Reaction rate of in reaction A (mol m^{-3} sec^{-1})
k	Constant in Debye- Scherrer equation
k_{AB}	Rate constant (varies)
k_{obs}	Observed sintering rate constant
k_B	Boltzmanns constant (J K^{-1})
K_b	Total number of bulk species
K_c	Equilibrium constant in concentration units for reaction i (varies)
K_g	Total number of gas-phase species
K_p	Equilibrium constant in pressure units for reaction i
K_s	Total number of surface species
k_f	Forward rate constant (varies)
k_r	Reverse rate constant (varies)
K	Equilibrium constant
G	Gibbs free energy (J mol^{-1})
G^0	Standard Gibbs free energy (J mol^{-1})
ΔG	Free energy change (J mol^{-1})

H	Enthalpy (J mol^{-1})
ΔH	Enthalpy change (J mol^{-1})
m	Sintering constant
$\dot{m}$	Mass flow rate (kg s^{-1})
N	Total number of species
N_T	Total number of active sites
n	Sintering order
n_{CH_4}	Moles of CH_4
n_{N_2}	Moles of N_2
p	Pressure (Pa)
p^0	Standard state pressure (Pa)
p_{H_2}	Partial pressure of H_2 (Pa)
p_{H_2S}	Partial pressure of H_2S (Pa)
Q	Chemisorption energy (kJ mol^{-1})
r	Interbody distance (m)
R	Gas constant (J mol^{-1} K^{-1})
$\dot{s}_k$	Molar production rate of species k due to surface reaction (mol m^{-2} s^{-1})
S_0	Sticking coefficient
S^0	Standard state of entropy (J K^{-1})
ΔS	Entropy change (J K^{-1})
t	Time (s)
T	Temperature (K)
T^0	Reference temperature (K)
T_m	Melting point of the metal (K)
S	Surface area of the catalytic bed (m^2)
SF_{cal}	Calculated stoichiometric factor
V_s	Volume of sample adsorbed (m^3)
x	Co-ordinate direction
W	Molecular weight
X_{CH_4}	Conversion of CH_4
X_K	Mole fraction of species k
$[X]$	Concentration (mol m^{-3}) for gaseous species, (mol m^{-2}) for surface species
Y_{CH_4}	Mole fraction of CH_4
Y_{N_2}	Mole fraction of N_2
z	Axial length (m)
Y_k	Mass fraction of species k
Z	Rate of collision (mol m^{-2} s^{-1})

Greek Letters

α_{CH_4}	Response factor of CH_4
α_{CO}	Response factor of CO
α_{CO_2}	Response factor of CO_2
α_{H_2}	Response factor of H_2
β	Temperature exponent in Arrhenius expression

ϵ	Porosity
φ	Deactivation function
ν'	Stoichiometric coefficient of reactants
ν''	Stoichiometric coefficient of products
ρ	Density (kg m^{-3})
η	Effectiveness factor
τ	Tortuosity
θ	Angle of incedence (degrees)
θ_k	Fractional coverage of adsorbed species k
θ_s	Fractional sulfur coverage
ϕ	Total surface coverage
λ	X-Ray wave length (A^0)

Subscripts

g	Gas-phase species
i	Reaction index
k	Species index
s	Surface species

Superscripts

0	Standard conditions
d	Diffusive
e	Effective

Abbreviations

AES	:	Auger electron spectroscopy
ATR	:	Autothermal reforming
CD	:	Condenser
CVD	:	Chemical vapor deposition
CPOX	:	Catalytic partial oxidation
DFT	:	Density functional theory
FTIR	:	Fourier transform infrared
GLS	:	Gas liquid seperator
HREELS	:	High resolution electron energy loss spectroscopy
HTS	:	High temperature shift
ID	:	Inner diameter
LEED	:	Low energy electron diffraction
LHHW	:	Langmuir-Hinshelwood-Hougen-Watson
LTS	:	Low temperature shift
MARI	:	Most abundant reactive intermediate
MCFC	:	Molten carbonate fuel cell
OD	:	Outer diameter
PAFC	:	Phosporic acid fuel cell
PEMF	:	Proton exchange membrane fuel cell
QSS	:	Quasi steady state
RDS	:	Rate determining step
SC	:	Sensitivity coefficient
SOFC	:	Solid oxide fuel cell
SR	:	Steam reforming
TC	:	Thermocouple
TPD	:	Temperature programmed desorption
TPR	:	Temperature programmed reduction
TST	:	Transitional state theory
UBI-QEP	:	Unit Bond Index-Quadratic Exponential Potential
UHV	:	Ultra high vacuum
WGS	:	Water gas shift reaction
XPS	:	X-ray photoelectron spectroscopy
XRD	:	X-Ray diffraction

Abstract

Biogas is an important source of renewable energy produced by the anaerobic digestion of biomass. The composition of biogas depends on the biomass source and duration of the digestion process. Biogas is an ideal fuel for distributed power generation using Solid-Oxide Fuel Cells (SOFCs), especially in areas that are not grid connected. Biogas may be combusted to produce electricity or can be converted to synthesis gas by reforming over Rh or Ni catalyst. However, the presence of H_2S or other sulfur containing compounds is a major problem for reforming of biogas because sulfur poisons most transition metals.

The goal of this research is two fold; i) experimental investigation of catalyst deactivation and regeneration, and ii) development of a comprehensive predictive microkinetic model for biogas steam reforming on Ni based catalysts. The kinetic model is developed based on experimental data and further validated by simulating the experiments reported in the literature. The kinetic model is able to capture the performance of a fixed bed reactor used to reform model biogas with and without H_2S in the feed gas.

The objective of the experimental study is the deactivation and regeneration of Ni catalysts supported on γ-Al_2O_3 during steam reforming of biogas containing ppm levels of H_2S. In order to ensure that the catalyst does not lose activity over time in a non-poisoning atmosphere (without H_2S), reforming experiments are performed at 700 and 800 °C for 22 hrs and no loss in activity of the catalyst is observed during this period. Catalyst deactivation experiments are then performed for two different temperatures (700 and 800 °C) and three different H_2S concentrations (20, 50, and 100 ppm). A low S/C ratio is employed to ensure the participation of CO_2 in reforming reactions. Low temperature operation (700 °C) lead to full deactivation of the catalyst where as at higher temperature (800 °C) the catalyst maintained some residual activity. In certain cases, catalyst regeneration is also performed by removing H_2S from the feed gas and by increasing the reforming temperature. The fully poisoned catalysts are then regenerated by steam treatment followed by reduction in H_2. The regenerated catalyst is tested for its activity by performing steam reforming reaction without H_2S in the feed stream. The regenerated catalyst showed stable operation for more than 13 hrs.

The fresh and spent catalysts are characterized by various techniques. XRD studies confirms the absence of coke formation during the reforming reactions with and without H_2S in the feed stream. This also asserts that the catalyst deactivation by introducing H_2S to the feed gas is purely due to sulfur poisoning. The N_2 adsorption/desorption isotherms are of type IV, which is typical for mesoporous materials. TPR results indicate a strong interaction of NiO with the support. The pulse chemisorption result shows that the Ni is well dispersed on the support, and the particle size of Ni crystal is very close to the value calculated using Scherrer equation.

The experimental data are then utilized to develop a detailed elementary kinetic mechanism for biogas reforming with and without H_2S in the feed gas. A comprehensive mechanism of the plausible elementary reaction steps of sulfur are added to an existing methane steam reforming mechanism on Ni. Using established theories, the kinetics of each of the elementary reaction steps on Ni metal catalysts are calculated. The Unity Bond Index-Quadratic Exponential Potential Method (UBI-QEP) is used to calculate the activation energies for both the forward and reverse direction of each step based solely on heats of chemisorption and bond dissociation energies of the species involved. Transition state theory (TST) is used to predict the pre-exponential factors for each reaction step. However, pre-exponential factors are further adjusted to make

the entire surface reaction mechanism thermodynamically consistent. A one dimensional fixed bed reactor model is used to simulate the experiments. Sensitivity analysis is carried out to understand the influence of pre-exponential factors on surface coverage of sulfur. The mechanism is then validated using experimental data in the temperature range of 600-950 °C for biogas free from H_2S and 700-900 °C for biogas containing 20-108 ppm H_2S. The model is capable of predicting deactivation of the catalyst in presence of H_2S in the feed mixture. Moreover, it qualitatively predicts the recovery of the catalyst activity on the removal of H_2S as well as temperature enhancement. The model also predicts saturation coverages of adsorbed sulfur that are comparable to experimental observations.

Contents

Chapter 1

Introduction

1.1 Background

The global energy demand is growing rapidly, and majority of the present demand is met by fossil based fuels such as coal, oil, and natural gas. Since the industrial revolution, our increased dependence on fossil based fuels has resulted in various airborne emissions leading to serious climatic, environmental, and health effects. These emissions are at alarming levels and require immediate actions to counter severe future problems. Moreover, the world's oil and gas reserves are concentrated in a small number of geographic regions, dominated by the Middle East. Any geopolitical uncertainities in these regions can lead to price fluctuations and scarcity in oil supply. The above few factors have led to an increased attention on renewable energy sources.

Renewable energy production is a key objective across the world. According to US Energy information and administration (EIA), the energy demand will increase during this century by a factor of two or three [1]. The European Commission has set legally binding targets for Europe to increase energy production from renewable sources from the current level of 7% to 20% by 2020 [2].

In the recent past, biogas systems have received considerable attention as an attractive source of renewable fuel that is clean, environment friendly, and cheap. Biogas is produced by anaerobic digestion of a variety of organic wastes. This technology offers a very attractive route for decentralized applications in rural areas for meeting the energy needs. Biogas energy is typically used for small to medium scale combined heat and power production, and also receives increasing attention as a renewable feed stock for chemical industry. An increased usage of biogas as a fuel reduces the dependence on fossil based fuels, and has important advantages for both environment and long term energy security. The production of biogas is considered to be a carbon neutral process [3]. Plants produce oxygen and carbohydrates from carbon dioxide by photosynthesis. So even if the organic matter produces carbon dioxide in the course of biogas formation, there is a good balance between the exhaustion of carbon dioxide into the atmosphere and absorption of carbon dioxide from the atmosphere.

Germany is the biggest biogas producer in Europe and has 5,905 plants in operation with an installed power generation capacity of 2,291 MW. The resultant electricity supply is approximately 12.8 TWh, which

is 12.6% of the total generated electricity from renewable sources [4]. The UK is another country which uses biogas widely for power generation and set the targets to deliver 29 GW from its present biogas plants and is targeting a total production of 32- 50 TWh by 2020 from biomass sources [2].

The Ministry of New and Renewable Energy, Government of India, has initiated a scheme on biogas based Distributed/ Grid Power Generation Programmes in 2006. The main objectives of these programmes are proper utilization of animal wastes and wastes from forestry, rural based industries (agro/ food processing), kitchen wastes, etc. India has a total of 348 biogas plants that produce a total capacity of 6,617 KW from 65,287 m^3 of biogas . Biomass energy and co-generation programmes are also promoted for optimum usage of India's biomass resources. These programmes have the potential to deliver 19,500 MW. At present a total of 437 MW of renewable electrical energy is produced from these biomass sources [5].

1.2 Feedstocks for biogas

A wide variety of biomass can be used as substrates for biogas production as long as they contain carbohydrates, proteins, fats, cellulose, and hemicelluloses as main components. Other technologies that produce fuel from biomass sources require very specific feed stocks. For example, ethanol technology requires high fermentable carbohydrate levels in corn and sugarcane, while biodiesel production requires feed stocks with high oil content, waste vegetable oils or virgin vegetable oil from oil seed crops [6]. In contrast, biogas can be made from most biomass and organic wastes regardless of the composition and over a large range of moisture contents, with limited feedstock preparation. In fact, biogas can even be made from the left over organic matter from both ethanol and biodiesel production.

The facility required for the production of biogas is called an anaerobic digester. A great variety of organic materials such as biological wastes of cattle dung, vegetable wastes, animal manure, municipal solid waste, industrial waste water, landfill, etc. can be used in anaerobic digesters depending on the design. A basic biogas digester consists of a tank in which the organic material is digested, combined with a system to collect and store the biogas produced. The digester can be quite simple, and the details vary depending on available materials and the needs of the community. For household purposes a floating dome design enjoys wide acceptance. Anaerobic digestion comprises mainly of four steps. The first step is the decomposition (hydrolysis) of plant or animal matter to break down complex organic materials into simple organic substances such as sugars and amino acids. A number of intermediate products are formed in the second and third steps that include alcohols, fatty acids and hydrogen. In the fourth step a unique group of microorganisms collectively referred to as methanogens convert matter into methane and organic acids [6].

The process temperature plays a key role in biogas digesters that affects the rate of digestion. These digesters are operated at three conventional temperature levels depending on the species of methanogens in the digesters; psychrophilic (below 25 °C), mesophilic (30−40 °C with an optimum of 35 °C) and thermophilic range (55−65 °C). Apart from temperature, the rate of biogas production also depends on factors such as the carbon to nitrogen ratio, solid concentration, pH, hydraulic retention time and nature of the feed stocks [7].

The composition of biogas depends heavily on the nature of the feedstock and process conditions, but the

main components are methane and carbon dioxide, with smaller amounts of hydrogen sulfide and ammonia. Trace amounts of organic sulfur compounds, halogenated hydrocarbons, hydrogen, nitrogen, carbon monoxide, and oxygen are also occasionally present. The gas mixture is saturated with water vapor and may contain dust particles. Table 1.1 shows the biogas composition from different feedstocks [8, 9].

Table 1.1: Biogas composition from different feedstocks.

Components (Volume %)	Municipal waste	Waste water	Agricultural /animal waste	Waste from agro food industry	Landfill
CH_4	50-60	61-65	55-58	68	47- 57
CO_2	34-38	36-38	37-38	26	37-41
N_2	0-5	2	1	3-5	-
O_2	0-1	1	1	1	-
H_2	-	-	-	0-5	-
CO	-	-	-	0-3	-
H_2S (ppm)	60- 750	700-2800	2100-7000	280	36- 115

1.3 Applications

Biogas can be used for all applications designed for natural gas with sufficient purification. The main difference between natural gas and biogas is the carbon dioxide content. Natural gas contains very low levels of CO_2 whereas biogas may contain up to 40% CO_2. Moreover, natural gas also contains small fractions of heavier hydrocarbons. These two differences result in a lower energy content of biogas compared to natural gas. The percentage of methane in the gas determines its calorific value as the other constituents do not contribute to the energy content. The methane content of biogas is appreciably high ($\sim$ 60%). This provides a high calorific value sufficient to find its use in many energy applications, including power generation. Table 1.2 shows the calorific values for different fuels [10].

Table 1.2: Approximate Calorific values of different fuels.

Fuel	Calorific Value (kcal/m^3)
Natural gas	8600
LPG	10,800
Kerosene	10,300
Diesel	10,700
Biogas	5000

1.3.1 Electricity generation

Raw biogas can not be used directly in engines or heaters because of H_2S content and other trace amounts of acidic compounds. The following upgrading techniques are widely used to get atleast 95% methane for certain applications [11].

- Physical absorption (scrubbing with liquid)
- Chemical absorption (chemical reaction with a liquid)

- Pressure swing adsorption (adsorption on material like activated carbon)
- Membrane separation
- Cryogenic separation (cooling at low temperature)
- In-situ enrichment (sludge treatment)

The biogas plants usually provide gas for cooking and lighting through specially designed mantles. In principle, the chemical energy of the combustible gases is converted to mechanical energy in a controlled combustion system using heat engine. This mechanical energy then activates a generator to produce electrical power. The most common heat engines used for biogas energy conversion are gas turbines and combustion engines. Combustion engines can be either internal combustion engine (e.g. reciprocating engine) or external combustion engine (e.g. Stirling engine) [12, 13].

1.3.2 Fuel for vehicles and fuels cells

There is a growing interest in the transport sector for replacing natural gas with upgraded biogas. Like natural gas, biogas can also be compressed and used in motor vehicles [14]. Upgraded biogas with >95% methane is required in order to be used in normal vehicles. Biogas can be used in both light and heavy duty vehicles. Light duty vehicles can normally run both on natural gas and biogas, whereas heavy duty vehicles require minor modifications. Sweden is the first country that used biogas as a transportation fuel and currently 11,500 vehicles are running with natural gas and biogas [15]. Biogas as vehicle fuel is also used in Switzerland, and other countries including Germany, Austria, France, Spain, India, China and USA are following the trend [16, 9, 5].

Low temperature fuel cells such as Polymer Electrolyte Membrane Fuel Cell (PEMFC) and Phosporic Acid Fuel Cell (PAFC) operate on pure hydrogen. Today 90% of hydrogen is produced by the catalytic reforming of light hydrocarbons and naphtha [17]. A viable alternative, for near and short term, is generating hydrogen from biogas. Biogas reforming can be used for on-demand production of hydrogen for automotive and distributed power generation applications. Catalytic reforming for biogas either by a dry reforming or by combination of dry and steam reforming using appropriate catalysts such as Ni, Rh or bimetallic catalysts produce synthesis gas. The synthesis gas can be used directly in various applications such as a fuel for Solid-Oxide Fuel Cell (SOFC), Molten Carbonate Fuel Cell (MCFC) or Fisher-Tropsch synthesis to produce synthetic liquid fuel. Fisher-Tropsch process uses a H_2/CO ratio 2:1 depending on the desired product [18]. These ratios can be tuned by adjusting steam to carbon ratio in biogas steam reforming. Fuel cells operating with biogas offer higher electrical conversion efficiency (> 50%) compared to internal combustion engines or gas turbines that operate on biogas, and produce less pollutants and greenhouse gases. Fuel cells are very sensitive to trace amounts of H_2S so necessary precautions should be taken if biogas is used as a fuel. Table 1.3 shows the tolerance levels for H_2S and CO for various fuel cell types [19].

Table 1.3: Tolerance levels of H_2S and CO in ppmv levels.

Fuel Cell	H_2S	CO
PEMFC	<1	<10
PAFC	<20	<10
MCFC	<10	Fuel
SOFC	<1	Fuel

1.4 Catalyst deactivation

Catalyst deactivation is a major problem for heterogeneous catalytic reactions. It is defined as loss of catalytic activity with time on stream. The deactivation process is inevitable in most processes but it may be slowed down or even be reversed with certain techniques [20, 21]. Interruption of the process for either replacement or regeneration results in loss of production and revenue.

The deactivation process may be physical and/or chemical in nature and occurs simultaneously with the main reaction. Generally the causes of deactivation are poisoning, fouling, phase transformation, and thermal degradation or sintering [20]. The deactivation time varies from seconds to years depending on the process. For example, entrained flow reactor with continuous regeneration deactivates within seconds (catalytic cracking and polymerization reactions), whereas the iron based catalysts in ammonia synthesis reactors deactivates over timespan 0f 5-10 years [20, 21].

Deactivation by poisoning occurs due to the strong adsorption of the poisoning species on active sites and thus blocks the adsorption or alters the adsorption energy of other species [22]. The poisoned catalysts may be regenerated and its activity can be partially restored by certain techniques [23, 24]. The best way to reduce catalyst poisoning is to decrease the amount of poisons in the fuel to more acceptable levels. Fuel/gas mixtures that contain sulfur compounds in ppm levels (>4) are considered to be poisonous to most catalytic reactors, and leads to the formation of inactive compounds on the surface and also to the morphological changes in the catalyst. Nickel catalyst reactor systems are more susceptible to sulfur compounds due to the strong chemisorption of sulfur species on Nickel active sites. The process of chemisorption is almost irreversible at lower temperatures and reversible at higher temperatures. Other compounds such as lead, phosphorous, zinc, calcium and magnesium are also considered to be catalyst poisons [20].

Fouling is another catalyst deactivation process in which carbonaceous materials form on the surface thus physically covering the active sites. Generally this is more severe in the dry reforming of hydrocarbons. Coke deposits may amount to 15% or even 20% (w/w) of the catalyst, and they may lead to deactivation of the catalyst either by covering active sites, and/or by pore blocking [20].

Catalyst sintering is another mechanism that refers to the loss of active surface area via structural modification of the catalyst. Generally sintering happens at higher operating temperature and leads to agglomeration and coalescence of small metal crystallites into larger ones with lower surface-to-volume ratio [20]. Solid-state transformation is another process and can be viewed as an extreme form of sintering at high temperatures and leads to the transformation of one crystalline phase into another one. For example active Nickel on alumina support forms an inactive Nickel Aluminate ($NiAl_2O_4$) at above 800 °C [20, 25].

1.5 Desulfurisation techniques

Most of the applications of biogas are discussed above are successful only in the absence of or at low H_2S concentration in the feed gas mixture. Hydrogen sulfide is typically the most problematic contaminant because of its toxicity and high corrosiveness. Additionally, combustion of H_2S leads to sulfur dioxide emissions, that are harmful to the environment and society. Hence it is necessary to remove hydrogen sulfide before the gas is taken into any process equipment. Biogas normally contains 100-10,000 ppmv H_2S depending on the feedstock. Hydrogen sulfide is formed when the reduction of sulfur-containing proteins under anaerobic conditions by sulfate reduction microorganisms. Inorganic sulfur, particularly sulfates, can also be biochemically converted to H_2S [26]. Table 1.4 shows the H_2S tolerance for various applications if biogas is used as fuel [11, 27].

Table 1.4: Tolerance levels of H_2S in different types of equipments.

Technology	H_2S tolerance (ppm)
Engines	
Heating boiler and Stirling engines	< 1000
Kitchen Stoves	<10
Internal combustion engines	< 500
Turbines	< 10,000
Micro turbines	< 70,000

A variety of technologies are available to remove H_2S from fuel streams. These methods are used depending on the final use, the volume of the gas to be treated, the concentration of H_2S present, and the absolute quantity of H_2S to be removed. Additionally, to achieve higher H_2S removal two or three process are combined. The H_2S removal methods are classified into physical- chemical, and *in-situ* biotechnological methods. Generally biotechnological methods are cheap and give higher efficiency and do not require any secondary treatments compared to the physical- chemical methods.

1.5.1 In-situ methods

In in-situ methods, iron chlorides, phosphates or oxides are directly added into the digester slurry. The addition of $FeCl_2$ is commonly practiced and iron hydroxide ($Fe(OH)_2$) in solid form is also used. They react with H_2S and form insoluble iron sulfide salts. These salts are precipitated and thus stripping of H_2S into the biogas is prevented. These methods generally achieve 100-200 ppm H_2S in the final stream.

$$Fe^{+2} + S^{-2} \rightarrow FeS \tag{1.1}$$

Another simple in-situ method is the addition of 2-6% oxygen or air directly to biogas digester or storage tank. In this process H_2S is converted to elemental sulfur or sulfates by biological aerobic oxidation in the presence of thiobacillus bacteria [28]. The removal of H_2S depends on the process temperature, hydraulic retention time and amount of air introduced, and H_2S may be reduced to 20- 100 ppm in biogas stream [29]. The disadvantages in this method is that the supply of oxygen may effect the anaerobic fermentation process and yellow clusters of sulfur are deposited on surfaces, which may lead to corrosion. Biogas is also explosive

in the presence of air depending on the methane content. Another disadvantage is accumulation of O_2 and N_2 in the biogas, which are very difficult to remove in the biogas up-gradation process [30].

1.5.2 Adsorption techniques

Physical and chemical adsorption techniques are widely used to remove H_2S from the biogas streams. The adsorption process is carried out at different temperatures with high surface area adsorbing materials such as activated carbon, copper, iron, aluminium, zinc, titanium or mixtures of these are used to achieve ultra low level H_2S concentrations. The main disadvantages of this process are high energy consumption due to the higher temperature operation, growing environmental concern over appropriate waste disposal methods, and expensive regeneration techniques [31].

Adsorption on activated carbon

The adsorption on activated carbon is widely used among the processes to achieve very low concentrations of H_2S. In addition to physical adsorption, activated carbon provides a catalytic surface for oxidation to elemental sulfur and sulfate. The sulfur is trapped on the internal surface of the activated carbon, which significantly enhances the removal capacity of H_2S. In presence of oxygen the following reaction takes place

$$H_2S + O_2 \rightarrow 2S + 2H_2O \tag{1.2}$$

Generally the activated carbon adsorption technique is carried out at $50-70\,^{\circ}C$ and at a pressure of $7-8$ bar. The removal capacity of activated carbon process can be significantly improved by impregnation with alkaline or oxide coatings on the activated carbon. Most commonly used coatings are potassium iodide, sodium hydroxide, sodium carbonate, potassium hydroxide, or metal oxides. The removal capacity is enhanced from normal 10-20 kg H_2S/m^3carbon to 120 -140 kg H_2S/m^3 carbon by impregnation. The major drawback in activated carbon process is the spent carbon disposal. The spent carbon must either landfilled or regenerated [29].

Adsorption on iron oxides

Adsorption on iron oxides is one of the oldest method, generally impregnated on wood chips (iron sponge) and pellets. In this method, H_2S is reduced to insoluble iron sulfides, which is converted into elemental sulfur by air in regeneration techniques. The following reactions take place during the adsorption and regeneration process.

Adsorption:

$$FeO + H_2S \rightarrow FeS + H_2O \tag{1.3}$$

$$Fe_2O_3 + 3H_2S \rightarrow Fe_2S_3 + 3H_2O \tag{1.4}$$

Regeneration:

$$FeS + \frac{1}{2}O_2 \rightarrow FeO + S \tag{1.5}$$

$$Fe_2S_3 + \frac{3}{2}O_2 \rightarrow Fe_2O_3 + 3S \tag{1.6}$$

The optimum operating temperature is 20 -50 $^{\circ}C$ and removal capacity of H_2S from 1000 ppm to 1 ppm is achieved in this process. The general drawbacks of the process are that it is chemical intensive, the operating

costs are high and a continuous stream of spent waste material is accumulated [30].

Using iron oxide impregnated on wood chips (iron sponge) is a mature technology. Generally this is carried out at 18- 46 °C, and 140 kPa. The time should be greater than 60 seconds for optimum removal of H_2S from the streams [29]. Iron oxide pellets are also made from redmud, which is a waste product from aluminium industry that has a higher surface to volume ratio than iron sponge. These pellets are impregnated with iron oxide or hydroxides and can remove 50 gm of H_2S per 100 gm of pellets. However, the pellets are more expensive than iron sponge. The major drawback on usage of iron oxide is safe disposal of spent iron oxide, which is considered as hazardous waste and requires special disposal procedures. Furthermore, the regeneration process is highly exothermic and requires accurate control of air flow and temperature, and if not controlled properly the wood chips may self-ignite [29].

ZnO supported on silica is gaining interest in the removal of H_2S at low temperatures. These systems have, however, low capacity and require large volumes of adsorbed bed. Recently modified mesoporous silica has received attention and is used as support materials for metal oxides and metals, due to a combination of good accessibility, uniform pore size, and high surface area. For example, MCM-41 (Mobil Composition of Matter No. 41), KIT-6 silica (ACS meterial mesoporous silica molecular sieve) and SBA 15 (Santa Barbara Amorphous) structures received considerable attention of many researchers for H_2S removal applications [26].

Adsorption on molecular sieves

Molecular sieves (zeolites) are used to seperate different compounds in the gas streams. The adsorption selectivity of different compounds depends on the mesh size and gas pressures. Generally polar compounds such as water, H_2S, SO_2, NH_3, carbonyl sulfide, and mercaptans are strongly adsorbed and can be removed from methane gas. Zeolites are thermally and chemically inactive, however, the main drawbacks are high investment cost and limited capacity.

1.5.3 Absorption techniques

In absorption techniques, solvents are used to remove the H_2S, which alters the solubility of H_2S by making water alkaline or by its oxidation to make it more water soluble. The solvents like methanol, polyethylene glycol ethers, and amine solutions are used for this purpose. Generally absorption column and stripper column (for regeneration) are operated simultaneously to achieve higher removal efficiency (> 99%). This process can handle wide range of pollutants, but the major drawbacks are high initial investment cost and large volumes of water and/or chemicals that are required for processing [29].

Caustic scrubbing

The absorption of H_2S on sodium hydroxide is the oldest method. In this method NaOH reacts with H_2S to form salts of sodium sulfide or sodium hydrogen sulfide. The formed salts are insoluble, that may precipitate in the scrubber. To avoid the formation of salts on the scrubber, spent caustic must be removed on regular basis. The major drawbacks are high investment cost and handling of caustic soda. Caustic soda is considered as poisonous material, and causes severe skin burns and eye damage [29].

Catalytic oxidation with chelated-iron salt solutions

In this method, the oxidation of H_2S into elemental sulfur is formed by the reduction of a soluble Fe^{+3} into a Fe^{+2}. The chelated agents helps in preventing the precipitation of iron sulfide or iron hydroxide, and ferrous ions can be re-oxidized to ferric ions in the presence of air. The chelated ferric iron (Fe^{+3}) is acting as a catalyst which improves the rate of chemical oxidation process. The following reactions take place during the absorption and regeneration [29].

Absorption:

$$H_2S + 2[Fe^{+3}] \rightarrow S + 2[Fe^{+2}] + 2H^{+} \tag{1.7}$$

Regeneration:

$$2[Fe^{+2}] + 0.5O_2 + 2H^{+} \rightarrow 2[F^{+3}] + H_2O \tag{1.8}$$

Sulfur removal efficiencies of 99.99% or higher can be achieved with this technology. There are many commercially available chelated ferrous iron catalysts in the market for this process namely LO-CAT®, MINI-CAT® redox chemistry technology (Gas Technology ProductsMerichem), SulFerox® (shell) and Sulfothane® (Biothane Corporation).

Biofilters and Biotrickling filters

In these systems the biogas is forced through a moist, packed bed that contains microorganisms. Microbes grow on the surface and crevices of the support, forming a biofilm. The H_2S in the biogas is transferred into the biofilm, where it is used as energy source by the microorganisms producing mainly sulfur if the oxidation is partial or sulfate if it is total. The H_2S removal efficiency depends on the medium, temperature, pH, nutrient and oxygen levels. The difference between biofilters and biotrickling filters is the nature of the carrier material: organic carriers in biofilters and inorganic carriers in biotrickling filters. The nutrients are not available in the inorganic carrier material, which are supplied by recirculating the liquid phase through the reactor. This liquid phase provides the moisture and in turn controls the pH or other operating parameters. The major problem found in biofilters is the acidification of the media due to sulfuric acid formation by the degradation of H_2S. This problem is avoided in biotrickling filters due to the fact that the acid reaction products are washed out continuously from the media [29].

Several commercial biofilters and biotrickling filters are available to remove H_2S with efficiency up to >99% such as Biopuric process (Biothane Corporation, Germany), BioSulfurex® (DMT Environmental technology), Biodox® (Closen B V, Dutch company), QSR® (Quick Sludge Removal), BiogasCleaner®.

Bioscrubber

Bioscrubbers are used for treating hydrogen sulfide containing gases from a wide variety of sources such as biogas, off-gases from wastewater treatment plants, livestock farms, etc. The biofilter medium is inexpensive and may contain sufficient micronutrients for the microbial growth. This process is operated simultaneously in two reactors. The first column is an absorption column in which the pollutants are absorbed in a liquid phase and liquid phase goes into a second unit, which acts as a activated sludge unit. In the sludge unit, microorganisms grow in suspended flocks of water degrading pollutants. The effluent is recirculated to the

first unit to increase the inoculation of microorganisms. This process usually removes 99.9% H_2S from the gas streams [32].

1.6 Objective and scope of thesis

Syngas gas production from various sources have been studied extensively by several research groups [33, 34, 35, 36, 37, 38]. The severe operating conditions during the reforming such as high pressure and high temperature, leads to several challenges concerning to the loss of catalytic activity. Catalyst deactivation is a complex phenomenon and it is affected by several known and even unknown factors [20, 39, 40, 41, 42].

The main objective of this thesis is to develop elementary steps of the surface reactions for biogas steam reforming in the presence of H_2S, and to determine kinetic parameters for them. The developed detailed kinetic model can be further used in reactor simulations under various conditions to understand the poisoning and regeneration of the catalyst at different operating temperatures. The work can be divided in two parts:

- Experimental study of catalyst deactivation and regeneration during biogas steam reforming on Ni catalyst.
- Development of a detailed kinetic model by means of Unity Bond Index-Quadratic Exponential Potential (UBI-QEP) calcuations and reactor simulations.

The experimental study deals with the catalyst preparation, its characterization and quantification of poisoning. Various techniques such as XRD, BET, TPR, and pulse chemisorption are used for characterization of catalyst samples. The modeling study deals with the development of a detailed kinetic scheme for biogas reforming and its validation with the experimental data. The UBI-QEP method is used in this thesis to calculate the reaction energetics and a one dimensional fixedbed reactor model is used to simulate the experiments.

This thesis is organized as follows: a review on biogas and its applications related to the electricity generation and fuel cell is given in Chapter 1. An extensive literature survey on biogas reforming technologies and catalyst regeneration methods are also reviewed in Chapter 1. The fundamentals of catalyst deactivation mechanisms are presented in Chapter 2. In particular, the deactivation mechanisms and modeling studies that are relevant to this thesis are examined. Chapter 3 describes the reactor and mainly focuses on the preparation and characterization of catalysts by various techniques. In Chapter 4, a review of micro-kinetics, transport and thermodynamics related to this research is presented. In Chapter 5, the UBI-QEP method, which is used to determine the activation energies and reaction enthalpies of the elementary reaction is described. In addition, thermodynamic consistency of elementary surface reaction mechanism is addressed in Chapter 5. Chapter 6 deals with numerical simulations of the fixed bed reactor using a one dimensional model by applying the kinetic model developed in this work. Finally, in Chapter 7, overall conclusions are drawn and suggestions are made for possible future extensions of the current research.

1.7 Biogas reforming- earlier studies

Effendi et al (2003)., reported biogas steam reforming reactions on Ni/ Al_2O_3 in fluidized bed and fixed bed reactors [43]. They have shown that higher conversions of CH_4 and CO_2 can be achieved in fluidized bed

reactors with slow deactivation compared to the fixed bed reactors. Fixed bed reactors with lower steam to carbon ratio resulted in massive carbon formation causing reactor blockage. In general, reducing the steam in the feed increases the selectivity towards CO production and enhanced CO_2 conversion in both types of reactors. The H_2/CO ratios depend strongly on steam concentration and increases with increasing steam to carbon ratio. In addition, the carbon deposition was dramatically reduced with ratios greater than 0.75 at 750 °C. For ratios less than 0.75, the reaction indicated critical conditions for carbon formation. Furthermore, it was observed that the catalyst fluidization was very poor owing to the massive carbon deposition. Increase in temperature resulted in higher conversions of CH_4 and CO_2. Moreover, enhanced selectivity towards H_2 and CO were observed with increasing temperature suggesting that water gas shift reaction is not favorable thermodynamically at higher temperatures.

In another study Effendi et al., [44] incorporated two CO shift reactors (fixed bed) to maximize hydrogen yield from fluidized bed biogas steam reforming. CO acts as a poison to low temperature PEM fuel cells even in the 10 ppm range and results in carbon formation through the disproportionation reaction. An increase in steam to biogas ratio resulted in slight increase in CH_4 conversion and steep decrease in CO_2 conversion at 850 °C. The increased CH_4 conversion leads to a selectively lower CO concentration and higher selectivity towards H_2 in the product stream. The H_2 in product stream remained constant for S/G (G-biogas) ratios above 0.8 and reached a maximum of 60% corresponding to an almost complete conversion of CH_4 at 850 °C. CH_4 conversion, H_2 and CO concentrations in the product stream very closely followed thermodynamic predictions. The CO_2 conversion, however, does not appear to follow the thermodynamic prediction at high S/G ratios. In the series of experiments at 850 °C, carbon deposition was identified at steam to biogas ratios less than 0.3. A limited amount of carbon (less than 0.1wt%) was identified during the biogas reforming with S/G ratios above 0.67.

Kolbitsch et al., reported biogas steam reforming on commercial nickel catalyst on CaO/ Al_2O_3 support in a fixed bed reactor [45]. They reported increasing CH_4 and CO_2 conversions with temperature and maximum H_2 production between 700- 800 °C. Above 800 °C the H_2 yield decreased due to the reverse water gas shift reaction, which was favorable at higher temperatures. CH_4 conversion and H_2 yield increased with increasing S/C but the CO_2 conversion was zero at S/C ratio of 2.9, above this value CO_2 was produced and below this value CO_2 was consumed.

Araki et al., studied the biogas autothermal reforming on Ni catalyst supported on a cordierite monolith with fluctuating CH_4 concentration in biogas [46]. They found CH_4 conversion to be about 70% in the absence of steam with an oxygen to methane ratio of 0.5. About 95% of CH_4 conversion was achieved at S/C = 2 and O_2/C = 0.5. They observed that S/C ratios above 3 adversely effects the methane conversion, and continuously decreased over time, due to the formation of NiO and Ni_2O_3 in the presence of steam. They extended their studies on startup procedures for catalytic partial oxidation and autothermal reforming of biogas [47], and found that the carbon free operation can be obtained by supplying oxygen below 427 °C for partial oxidation of biogas. Auto thermal reforming was possible only when steam was supplied at temperatures higher than 450 °C, below which the catalytic activity decreased due to the formation of NiO. They reported that the formation of NiO can be prevented by supplying steam at temperature higher than that is required for catalytic partial oxidation. The Ni metal may be oxided to NiO during steam reforming, dry reforming, catalytic partial oxidation, and auto thermal reforming. However, NiO is reduced to nickel by

CH_4 or H_2 which is produced during the above reactions.

Xu et al., developed catalysts for carbon free operation for biogas dry reforming at 800 °C [48, 49]. They have used CH_4/CO_2 ratio of 1.0 on Ni-Co bimetallic catalyst supported on γ- Al_2O_3 modified with La_2O_3 in a fixed bed reactor. It is a known fact that addition of promoters inhibits carbon formation. Lanthanum oxide is an excellent promoter which can strengthen CO_2 adsorption. The addition of cobalt also improves the anti coking and catalytic activity. The excellent performance of Ni-Co bimetallic catalyst is due to the high metal dispersion, strong metal support interaction, and formation of stable strong solution. The conversions of CH_4 and CO_2 on Ni/La_2O_3-Al_2O_3 are improved by addition of cobalt.

Sun et al., reported the tri-reforming of biogas on nickel based SBA-15 (mesoporous silica supported) in fixed bed micro reactor [37]. They observed improved conversions of CH_4 with the addition of oxygen but no significant effect on CO_2 conversion for O_2/CO_2 ratio less than 0.6. However, CO_2 conversions decreased with O_2/CO_2 ratio greater than 0.6, which may be due to the added oxygen that promotes CH_4 conversion.

Reforming of a model biogas on nickel and rhodium-nickel catalysts with addition of lanthanum was reported by Lucredio et al., in a fixed bed reactor [50]. Higher CH_4 conversion was achieved in Rh-Ni and Rh-NiLa than Ni and Ni-lanthanum catalysts. They found that Ni and Ni-lanthanum catalysts converts more CO_2 than CH_4. This may be due to the reverse water gas shift reaction which occurs simultaneously with dry reforming reaction. They concluded that formation of carbon was suppressed by addition of lanthanum oxide to nickel catalysts and addition of synthetic air to the biogas.

Bereketitodou et al., reported [38] that the addition of CeO_2 improves the nickel dispersion on the support resulting in improved catalytic activity and resistance towards the carbon deposition. The conversions are increased by the addition CeO_2 to the Ni/Al_2O_3 catalysts at temperature above 800 °C. However, the conversions of CH_4 and CO_2 were less in the temperature range 700- 800 °C on Ni/CeO_2-Al_2O_3. They concluded that ceria based catalysts enhances the water gas shift reaction because of their strong interactions with the metal due to the transition between Ce^{+3} and Ce^{+4}. Moreover, CeO_2 has a high oxygen storage capacity, which helps in water gas shift activity.

Izquierdo et al., reported tri-reforming of biogas on Ni and Rh-Ni catalysts supported on magnesia or alumina modified with CeO_2 and ZrO_2 [51]. They found higher hydrogen yields on Rh-Ni/Ce-Al_2O_3 than Ni/ MgO catalysts in dry reforming. The low hydrogen yield on Ni/MgO catalyst may be due to the reverse water gas shift reaction. Interestingly on Rh-Ni/Ce-Al_2O_3 catalysts increasing S/C ratio, resulted in low CO_2 conversions and H_2 yield. This could be related to the water gas shift reaction which is favourable at higher S/C ratios. They have concluded that for biogas tri reforming reactions the highest CO_2 conversion and hydrogen yields were achieved at O_2/CH_4 =0.25 and S/C=1.0. The same trend was observed in Ni/Ce-Zr-Al_2O_3 micro reactors.

Much of the work has been done on steam reforming and/or dry reforming of biogas in the absence of hydrogen sulphide. The presence of H_2S in the biogas adversely affects the activity of the nickel based catalysts. Although desulphurization technologies can decrease the amount of hydrogen sulphide present in the biogas, the remaining minor concentrations of sulfur cannot be tolerated by nickel-based catalyst even the if

fuel processor is operated at higher temperatures (>700 °C) [23].

Asharfi et al., [23] reported the biogas steam reforming in the presence of H_2S on commercial nickel based catalyst. They have tested biogas steam reforming with different concentrations of H_2S in the feed at different operating temperatures and concluded that the H_2S poisoning proceeds quickly depending on the H_2S concentration in the feed gas and operating temperature. It is important to note that the poisoned Ni catalyst keeps an appreciable residual activity at 900 °C, but at 700 °C the catalytic activity decreases rapidly even for low concentration of H_2S. They have also found that H_2S poisoned catalysts can effectively be recovered by temperature enhancement. Furthermore, extent of catalyst regeneration by H_2S removal increases with increasing temperature.

1.8 Regeneration of poisoned catalysts

The chemisorption of hydrogen sulphide on a supported nickel catalyst is reversible [52], but the driving force is extremely small. The sulfur deactivated catalyst can be regenerated in a reducing environment at higher temperatures. However, temperature increase may be difficult in some cases because of the temperature limitations of the reactor system or due to sintering of the catalyst.

Wang et al., [53] carried out DFT studies on the regeneration of sulfur poisoned catalysts. They claimed that O_2 is more effective than H_2O in removing the adsorbed sulfur atoms from nickel surface. However, exposure to the large amounts of O_2 or H_2O can lead to excessive oxidation of the nickel metal, resulting in adsorption of oxygen atoms (O(s)) and formation of NiO. While O(s) species can be readily removed by H_2 or other fuels, the formation of bulk NiO will significantly deactivate the Ni catalyst, mostly due to the volume change associated with the redox reaction of Ni. They finally concluded that H_2O is a better candidate for removing surface sulfur without over-oxidizing the Ni surface because of its broader pressure range.

Shawal Nasri et al., reported poisoning and regeneration of precious matels catalysts during CH_4 decomposition in the presence of H_2S [54]. FTIR spectroscopic investigations indicated that the nature of the metal species on the catalysts is different for the freshly reduced and regenerated catalysts. The catalytic activity for fresh catalysts followed the order of Pd > Rh > Pt. Regenerated Pd catalytic showed less activity than the fresh catalyst, but regenerated Rh and Pt showed higher activity than fresh catalyst. They claimed that the differences in catalytic activity is due to the changes in metallic structure caused by H_2S exposure. In the case of Rh/Al_2O_3, the regenerated catalyst shows an increased Rh^+/Rh^0 ratio compared to the fresh catalyst. They observed that the catalytic activity for regenerated catalysts is reduced in the order of Rh > Pt > Pd.

Conventionally sulfur-poisoned steam reforming catalysts are regenerated by sequential treatment with stream, steam-air mixture, and steam-hydrogen mixture (H_2O/H_2 molar ratio of 100) [55]. Steam has been shown to have no influence on the chemisorption equilibrium but, according to the results by Rostrup [52], steaming of sulfur poisoned catalysts results in complete oxidation of the metallic nickel to nickel oxide. Sulfur can be removed easily at temperatures above $600 - 650$ °C if the catalyst is unpromoted. However, If the catalyst is promoted with magnesium or calcium, temperatures above 700 °C are required. The sulfur on the catalytic surface is removed in the form of SO_2 and H_2S. The following reactions take place during the

regeneration process

$$Ni - S + H_2O \rightleftharpoons NiO + H_2S, \tag{1.9}$$

$$H_2S + 2H_2O \rightleftharpoons SO_2 + 3H_2, \tag{1.10}$$

$$Ni + H_2O \rightleftharpoons NiO + H_2. \tag{1.11}$$

If the catalyst is promoted with potassium or sodium, treatment with steam and steam- air mixture may result in a nearly complete conversion of chemisorbed sulfur to alkali sulphate. Owing to the high stability of alkali sulphates ($NiSO_4$), regeneration of alkali promoted catalysts becomes difficult. $NiSO_4$ may be decomposed into H_2S according to the following reaction.

$$NiSO_4 + 4H_2 \rightleftharpoons NiO + H_2S + 3H_2O \tag{1.12}$$

The major disadvantages of conventional regeneration process are slow sulfur removal rate, which declines exponentially with time. These process also requires large volume of sulfur-free reducing gas. Recently Li et al. [24], developed faster regeneration methods to remove adsorbed sulfur on Ni based steam reforming catalysts. The regeneration method proposed by Li et al., has the following steps. Initially the adsorbed sulfur is oxidized in the presence of low flow 1% O_2 into SO_2 and $NiSO_4$ at 750 °C, $NiSO_4$ is decomposed into O_2, SO_2, and NiO in the inert argon atmosphere at 900 °C, the nickel oxide is reduced into metallic nickel with 2% H_2 at 900 °C, and finally the trace amounts of sulfur is removed at 900 °C with steam reforming. They claimed that after regeneration by this method, the reforming performance of the the deactivated catalyst is fully regained to its initial activity.

Chapter 2

Catalyst Deactivation

Catalytic deactivation inherently occurs during the fuel processing of hydrocarbons, which is due to the process conditions and impurities present in the feed. It may be physical and/or chemical in nature, and occurs simultaneously with the main reaction. The deactivation process depends on nature of the process and varies on time scales from few seconds to years. For example, catalytic cracking reactions may take few seconds for deactivation, while ammonia synthesis process takes 5-10 years for iron catalyst deactivation. It costs to the industry billions of dollars per day for catalyst replacement and process shutdown. The deactivation process is inevitable but can be slowed down or may be compensated with certain techniques [23, 24].

Catalyst deactivation can generally be classified in to physical and chemical. Physical deactivation is caused by the blocking of pores by entrained solids, loss of active sites due to agglomeration (site sintering), closure of pores by internal collapse (support sintering), and the reversible loss of active sites by physical adsorption of impurities. Chemical deactivation includes the irreversible loss of active sites through chemisorption of impurities, loss of sites due to coking, and pore blockage due to coking. The deactivation mechanisms can be classified as, coking or fouling, poisoning, phase transformation, and thermal degradation or sintering [20]. Other deactivation mechanisms include masking and loss of active elements via volatilization, erosion and attrition [21].

2.1 Deactivation by Coking

Catalyst deactivation due to the coking or fouling is caused by the formation of carbonaceous material on surface of the catalyst, thereby blocking the pores of the catalyst. This phenomena is generally observed in hydrocarbon catalytic reactions with steam and dry reforming reactions. The deactivation process by coking is more severe for dry reforming reactions of alkanes. Several authors have investigated the coke formation on Ni supported catalysts [56, 57, 21, 58, 59, 60] and concluded that the different routes to carbon formation affect the morphology of the carbon and the way it is gasified. Three types of carbon are observed during the steam reforming reactions such as, whisker like, encapsulating, and pyrolytic carbon. Whisker like carbon is formed at temperatures greater than 450, encapsulating carbon films are formed by slow polymerization of C_nH_m radicals on Ni surface at temperatures below 500 °C, and pyrolytic carbon is formed during thermal cracking of hydrocarbons [33, 60]. The following main reactions are responsible for the coke

formations [59, 61].

$$CH_4 \rightleftharpoons C + 2H_2 \quad \Delta H^0 = 75 \text{ kJ/mol} \tag{2.1}$$

$$2CO \rightleftharpoons C + CO_2 \quad \Delta H^0 = -172 \text{ kJ/mol} \tag{2.2}$$

$$CO + H_2 \rightleftharpoons C + H_2O \quad \Delta H^0 = -131 \text{ kJ/mol} \tag{2.3}$$

$$C_nH_m \rightleftharpoons nC + \frac{m}{2}H_2 \tag{2.4}$$

$$C_nH_m(\text{higher hydrocarbons}) \rightleftharpoons \text{Olefins} \rightleftharpoons \text{coke} \tag{2.5}$$

$$C_nH_m(\text{higher hydrocarbons}) \rightleftharpoons (CH_2)_n \rightleftharpoons \text{gum} \tag{2.6}$$

The above equations are reversible, and the basis to removal of carbon by gasification [60, 62]. The formation of coke via exothermic reactions 2.2 and 2.3 become less favorable as the temperature increases, and coke formation via endothermic reaction 2.1 becomes important at higher temperatures, which can rapidly deactivate the catalyst. Moreover, the decomposition of CO also forms carbon films on the surface. Depending on their reactivity and temperature of formation, carbon films can be classified into five types; adsorbed atomic carbon(C_α), amorphous carbon (C_β), vermicular carbon (C_ν), bulk nickel carbide (C_γ), and graphitic carbon(C_c) [21]. Table 2.1 shows the different forms of carbon during CO disproportionation reaction.

Table 2.1: Forms of carbon from disproportionation of CO.

Structural type	Temperature(°C)	name
Adsorbed, atomic (surface carbide)	200 – 400	C_α
Polymeric, amorphous films	250 – 500	C_β
Vermicular filaments, fibers	300 – 1000	C_ν
Nickel carbide (bulk)	150 – 200	C_γ
Graphitic (crystalline) platelets	500 – 550	C_c

Coking is one of the major factors to be controlled for industrial steam reforming applications. The operating conditions are chosen to increase H_2O/C or CO_2/C ratio to favor the reverse of reactions 2.2 and 2.3 for carbon free operation [60]. Although, high temperature steam is expensive, any measures to reduce coke formation have significant economic advantage for the process [63]. Table 2.2 shows the critical parameters for the coke formation reactions.

In extreme cases, strong carbon filaments may build-up in pores to the extent that they stress and fracture the support material, ultimately causing disintegration of catalyst pellets and plugging of reactor voids. Some forms of carbon result in loss of catalytic activity and some do not. For example, at low temperature (< 300-375 °C) condensed polymer films and at high temperatures (> 650 °C) graphitic carbon films encapsulate the metal surfaces of methanation and steam reforming catalysts. In the intermediate temperature range of 375 - 650 °C, carbon filaments are formed by precipitation of dissolved carbon at the rear side of metal crystallites causing metal particles to grow away from the support. Filament growth ceases when sufficient carbon accumulates on the free surface to cause encapsulation by a carbon layer. However, encapsulation of the metal particles does not occur if H_2/CO or steam/carbon ratios are sufficiently high. Thus, carbon filaments from CO hydrogenation and steam reforming may not necessarily cause intrinsic loss of catalytic activity unless

Table 2.2: Type of carbon formation.

carbon type	reaction	phenomena	critical parameters
Whisker carbon	2.1 – 2.4	Catalyst pellet breakup	Low H_2O/C ratio, high temperature, Presence of olefins, and aromatics
Pyrolytic	2.5	Encapsulation on catalyst surface	High temperature, high residence time, presence of olefins
Gum	2.6	Blocking of Ni surface	Low H_2O/C ratio, absence of H_2, lower temperature

they form in sufficient quantity to cause plugging of pores [58, 64].

The chemical nature of the carbonaceous material depends on the temperature, pressure, the age of the catalyst, nature of the feed, and products formed. An important principle is that the rate of deactivation greatly depends on the difference in rates of formation and gasification of carbon or coke precursors. In steam reforming reactions, carbon formation rate is a function of hydrocarbon structure. For example, carbon formation decreases in the order of acetylenes, olefins and paraffins. Hydrogen acceptors presence in acetylenes and olefins accelerate the carbon formation [65]. Moreover, the carbon formation rate greatly depends on the catalyst structure, metal crystallite size, promoter and catalyst support. For example, Ashcroft et al., reported methane partial oxidation using CO_2 on Ni, Pd, Rh, Ru and Ir catalysts with γ-Al_2O_3 support. They found carbon formation on Ni and Pd, but not on Rh, Ru and Ir catalysts at temperature of 1050 K. They have also observed that Ni is more susceptible to carbon formation than Pd [66]. In another significant work Rostrup- Nielsen and Bak Hansen on methane dry reforming with Ni, Ru, Rh, Pd Ir and Pt as catalysts, demonstrated large differences. Ni alone showed carbon formation at a temperature of 775 K, whereas at 925 K, the carbon formation rates were increased enormously for some of the noble metals. The formation of carbon increases in the order of Ru < Pt < Ir < Rh < Pd < Ni, and Ru is the best suitable catalyst for dry reforming of methane [61].

The addition of noble metal to the base metal can also significantly reduce formation of carbon. For example, bimetallic catalyst Ni- Pt reduces the carbon formation in methanation, and Cu-Ni and Co-Ni bimetallic catalysts substantially reduce the carbon in steam reforming as well as dry reforming reactions [65]. In addition to this, promoters and inhibitors also enhance the gasification rate of adsorbed carbon or coke precursors, and suppress the carbon formation reactions on the catalytic surface. Moreover, the coke formation rate is proportional to the acid strength of the support. For example, potassium is used in Ni based steam reforming reaction, that neutralizes the acid sites, and enhances the gasification of adsorbed carbon [67]. Different types of coke are formed based on bi functional metal or acidic oxide support. In case of Pt catalyst soft coke is formed and bimetallic Pt- Re catalyst results in hard coke formation on γ- Al_2O_3 support in the catalytic reforming [68].

Rostrup-Nielsen et al., reviewed the deactivation process due to the coking from hydrocarbon reforming. They postulated that the coke is formed from different sources. However, irrespective of the sources, the initial mechanistic step involves the dehydrogenation and formation of unsaturated species, that may migrate

to gaseous phase or adsorbed phase. One of the source for coke formation is high temperature gas phase reactions, in which intermediate carbonaceous material may form from the free radicals, and condenses on the catalyst surface. A highly accepted mechanism for the formation of carbon in reforming reactions is the dissociation of hydrocarbon on nickel catalyst to produce highly reactive carbon, in which most of the carbon is gasified and the remaining is less reactive due to the polymerization and rearrangement [69]. The less reactive carbon may encapsulate the Ni surface, and may dissolve in the Ni crystallite. The dissolved carbon may diffuse through nickel and precipitate at the rear side of the crystallite. This process leads to the formation of whisker like carbon. This is the one of the few cases where carbon formation does not lead to deactivation, but it results in pressure build up in industrial applications. Rostrup- Nielsen reported that unsaturated olefins and aromatics are highly susceptible to the coke formation. In general formation of coke increases with unsaturation, molecular weight, and aromaticity.

2.1.1 Modeling of deactivation due to coking

Froment developed catalyst deactivation models for different levels such as, catalyst active site, the particle site, and reactor level. These models are developed based on mechanistic approach of coke formation [70]. The deactivation models at active site and particles site level are used to develop the deactivation model at the reactor level.

Deactivation at active site level

The deactivation by coking at active site level model is developed based on Hougen- Watson approach for a reaction $A \rightleftharpoons B$. The model is based on the assumption of single site adsorption, no diffusional resistance, and surface reaction as the rate determining step [70]. The deactivation functions for the main reaction and coke formation are given by

$$\frac{r_{Ai}}{r_{Ai}^{0}} = \varphi_{Ai}, \tag{2.7}$$

where r_{Ai} is rate of reaction i for reactant A, r_{Ai}^{0} is initial rate, i.e, in the absence of coke, and φ_{Ai} is the deactivation function of reactant A in i'th reaction. For the coke formation

$$\frac{r_{C}}{r_{C}^{0}} = \varphi_{C}, \tag{2.8}$$

where φ_C is the sum of the coking rates. The above rate equations are intrinsic, i.e, free of diffusional limitations. Coke formation is not a simple one step transformation of chemical species. It proceeds through a sequence of steps gradually leading to a carbonaceous residue. The deactivation function has to be expressed in terms of the deactivating agent: for coking obviously the coke precursor, for poisoning the true poison. This means that the local amount of coke (or poison) on the catalyst site has to be known and this requires a rate equation for the formation of the coke precursor.The reaction rate (surface reaction controlled) r_{AB} is given by

$$r_{AB} = \left(\frac{c_t - c_{C1}}{c_t}\right) \frac{k_{AB} K_A c_t \left(c_A - (c_B/K)\right)}{1 + K_A c_A + K_B c_B}, \tag{2.9}$$

where c_t is the total active sites concentration, c_{C1} is coke concentration at active site, K is the reaction equilibrium constant, k_{AB} is rate coefficient, c_A and c_B are the concentrations of reactants and products respectively, K_A and K_B are adsorption equilibrium constants. The fraction $(c_t - c_{C1})/c_t$ gives the free active

sites (φ_A) after coking.

The reduction of active sites information and coke formation rates are required for the actual rate of reaction r_{AB}. The coke may be formed from the reactants (parallel coking) or from the products (consecutive coking); for parallel coking

$$r_C = \frac{\varphi_C k^0_{C,A} c_t K_A c_A}{1 + K_A c_A + K_B c_B} = r^0_C \varphi_C, \tag{2.10}$$

and for consecutive coking

$$r_C = \frac{\varphi_C k^0_{C,B} c_t K_B c_B}{1 + K_A c_A + K_B c_B} = r^0_C \varphi_C, \tag{2.11}$$

where $k^0_{C,A}$ and $k^0_{C,B}$ are the rate coefficient for coke from A and B components respectively, φ_C equals φ_A only at coking at the same site and equal number sites. The above equations are valid only for single site coking. When n_A sites are involved in the rate determining step of the main reaction and n_C sites in the coking, then

$$\varphi_A = \left(\frac{c_t - c_{C1}}{c_t}\right)^{n_A}; \quad \text{and} \quad \varphi_C = \left(\frac{c_t - c_{C1}}{c_t}\right)^{n_C}. \tag{2.12}$$

Deactivation at the particle level

The active sites are distributed through out the pores of the catalyst particle. Initially coke is formed on the active sites by formation of coke precursors and coke molecules grow up and lead to the pore blockage. In this model rate determining step is single site surface reaction $A \leftrightarrow B$. The model is developed based on three steps: the formation of coke precursors from the adsorbed species, precursors of coke grows on the active sites, and termination of the growing coke [70]. The reaction rate for the main reaction r_{AB} is

$$r_{AB} = \frac{k_{AB} K_A c_t c_A (1 + K_A c_A K_B c_B)}{\phi}, \tag{2.13}$$

where ϕ is the accessible fraction of active sites for the reaction, and is given by $1 - (c_{t,acc}/c_t)$. The total coke formation during the deactivation at the particle level is given by

$$c_{C,global} = \frac{3}{R^3} \int_0^R r^2 c_C(r) dr. \tag{2.14}$$

Deactivation at the reactor level

A plug flow reactor model is used to develop the deactivation model with the assumption of no interfacial diffusion limitations. The continuity equation for A component for pseudo steady state is given by [70]

$$-\frac{dF_A}{dz} = N_A \frac{S}{V}, \tag{2.15}$$

where

$$N_A = | - D_{\text{A,eff}} \left(\frac{\partial c_A}{\partial r}\right)|_{r=R}, \tag{2.16}$$

where D_{eff} is the effective diffusivity, which is a combination of molecular and Knudson diffusivities in the straight pore, and S/V is the ratio of external surface area to volume of the bed. This model is used for the simulation of isothermal plug reactor by Beyne and Froment [71] and concluded that in the case of parallel coking, the coke formation is higher at the reactor inlet as time proceeds, and large fraction of reactant is converted as the reactor length increases. In consecutive coking, the formation of coke increases with the

reactor length as a result the fraction of reactant conversion decreases.

2.2 Thermal degradation and Sintering

Catalyst sintering is another mechanism that refers to the loss of active surface area via structural modification of the catalyst. Generally sintering happens at higher operating temperature and leads to the formation of agglomeration and coalescence of small metal crystallites into larger ones with lower surface-to-volume ratio [20].

Two different sintering mechanisms have been proposed by Gruber et al., i) atom migration, and ii) particle migration and coalescence [72]. Atom migration refers to the process where metal atoms are emitted from one metal particle and captured by another metal particle. In particle migration process, the particles themselves move over the support and collide and coalesce to form larger particles. The driving force for both processes is the difference in surface energy, which varies inversely with the particle size.

Sintering process is accelerated by high temperature and presence of water vapor. Sintering in steam reforming reactions is mainly caused by the atomic migration of nickel particles at above 600 °C. [20, 21]. There are many parameters that can also affect the sintering, which include atmosphere, metal type, metal dispersion, promoters/impurities, support surface area, texture, and porosity. Sintering rate increases exponentially with temperature and in the presence of O_2, and relatively low in H_2 atmosphere [21].

Sintering temperature generally depends on the melting temperature of metals. The ideal operating temperature for dry reforming reaction is $0.5T_m$, and $(1/3)T_m$ for steam reforming reactions, where T_m is the melting temperature of the metal. The limit for the steam reforming is lower due to the presence of steam, as it facilitates reorganization of many metals, alumina and silica. Table 2.3 shows the sintering temperatures for the different metals in steam reforming reactions [73].

Table 2.3: Sintering temperatures for different metals in steam reforming.

Metal	Sintering temperature (°C)
Cu	360
Fe	500
Ni	500
Pt	570
Pd	500

Sintering can be prevented by adding stabilizers like chromium, alumina, or magnesia to the catalysts that may have a high melting point, and prevent agglomeration of small crystals. There is evidence that adding trace amounts of chlorinated compounds to the gas phase prevents the platinum catalyst sintering [73]. Metal crystallite stability generally decreases with decreasing metal melting temperature in reducing atmosphere in the order Ru > Ir > Rh > Pt > Pd > Ni > Cu > Ag, but this order may be affected by the strong metal support interactions [20]. For example, platinum stability decreases in the order Pt/ Al_2O_3 > Pt/ SiO_2 > Pt/C. In oxidizing atmosphere, metal crystallite stability depends on the volatility of metal oxides and strength of

metal support interactions. For example, crystallite stability decreases in the order Rh > Pt > Ir > Ru [21].

Baker and Trimm et al., [74] reported on sintering of catalyst support materials. Single phase oxide carriers may sinter by one or more combinations of surface diffusion, solid state diffusion, evaporation/ condensation of volatile atoms or molecules, and grain boundary diffusion. They claimed that γ-Al_2O_3 and silica supports in oxidizing atmosphere, and carbon carriers in reducing atmosphere are the most thermally stable carriers. Doping of additives and impurities can also improve the thermal stability of the supports, which occupy the defective sites or form new phases. For example, by adding calcium, barium, nickel or lanthanum oxides to alumina supports may form thermally stable spinel phases [73]. In steam reforming reactions water vapor accelerates the support sintering by forming mobile surface hydroxyl groups which are volatile at higher temperatures.

2.2.1 Modeling of sintering

The kinetics of sintering is a function of temperature, time, pressure and concentrations. The sintering kinetics are developed from active metal surface area versus time measurements at constant temperature [20]. A simple sintering kinetics can be fitted with simple power law expression

$$-\frac{d(\frac{D}{D_0})}{dt} = k_s \left(\frac{D}{D_0}\right)^n, \tag{2.17}$$

where k_s is the sintering rate constant, D_0 is the initial dispersion, and n is the sintering order

$$k_s = k_{s0} \exp\left(\frac{-E_a}{RT}\right), \tag{2.18}$$

where k_{s0} is the initial rate constant, E_a is the activation energy, R is the gas constant, and T is temperature. The sintering order varies from 3 to 15, lower n values indicates atomic migration, and larger values of $n > 4$ indicates particle migration. This equation is not valid for sintering processes because it assumes that surface area or dispersion ultimately reaches zero given sufficient time, when in fact, for a given temperature and atmosphere, a non-zero or limiting dispersion is observed after long sintering times. Moreover, the use of this equation is further questionable because variations in sintering order are observed as a function of time and temperature for a given catalyst in a fixed atmosphere.

Bartholomew and co-workers [20] have proposed an expression for the sintering rates that considers the effects of temperature, atmosphere, metal, promoter, and support. This is developed by fitting sintering data to general power law expressions

$$-\frac{d(\frac{D}{D_0})}{dt} = k_s \left(\frac{D}{D_0} - \frac{D_{eq}}{D_0}\right)^m \tag{2.19}$$

the additional term D_{eq}/D_0 accounts for the asymptotic nature of dispersion versus time curve to a limiting D_{eq} at infinite time, m is the order of the sintering which is either 1 or 2.

2.3 Catalyst poisoning

The presence of impurities in the feed have a tremendous effect on the performance of the catalyst. The most important poison for catalytic steam reforming is sulfur. Sulfur compounds in the feed are converted into H_2S under reforming conditions, and leads to the total deactivation of the catalyst. Catalyst poisoning occurs due to the strong adsorption of sulfur or other poisons on active site, and consequently blocks or alters the adsorptivity of the other species by electronic effect [75]. Moreover, poisons may modify the chemical nature of the active site due to the strong adsorption or reconstruction of the catalytic surface [33].

Catalytic poisons are classified based on the chemical structure, selectivity, and nature of reactions poisoned. Table 2.4 shows the catalyst poisons classification based on chemical structure [20].

Table 2.4: Poisons classification based on chemical structure.

Chemical	Examples	Type of interaction
V A and VI A group	N, P As, Sb, O, S, Se, Te	Shielded structures with s and p orbitals
VII A	F, Cl, Br, I	Formation of volatile with s and p orbitals
Toxic metals and ions	As, Pb, Hg, Bi Sn, Zn, Cd, Cu, Fe	May form alloys with d orbitals
Molecules with multiple adsorption bonds	CO, NO, HCN, C_6H_6, C_2H_2, unsaturated HCs	Chemisorption through multiple bonds and back bonding

Poisons can be classified as selective, anti-selective, and non-selective. The difference between these three are related to the nature of the surface, and the degree of interaction of the poison with the surface. The strongest active sites are poisoned first in selective poisoning, lesser active sites are blocked initially in anti-selective poisoning. In the both cases the catalyst activity depends on the amount of poison chemisorbed. In non-selective poisoning, the less active sites are poisoned in a uniform manner and net loss of catalytic activity is a linear function of chemisorbed poison [21, 20]. An example for selective poisoning is deactivation of platinum by CO for the para-H_2 conversion, Pb poisoning on platinum for CO oxidation is anti-selective, and arsenic poisoning of cyclopropane hydrogenation on Pt is non-selective.

Selective poisoning is preferred for certain reforming reactions and hydrocracking reactions to adjust the selectivity. Sulfur compounds are strongly chemisorbed on the active sites and thus reduces the number of active sites for the reaction. For example, the sulfur passivated nickel catalysts are used for carbon free methane dry reforming [76] and Pt-Re/ Al_2O_3 is pretreated with low concentrations sulfur to limit the hydrocracking activity [77].

Poisoning of catalytic reactions may be reversible or irreversible. In reversible poisoning, the poisons are weakly adsorbed on the surface, and the catalyst activity is regained by simply removing the poisons from the feed. For example, H_2O and CO are considered as poisons for iron based catalyst in ammonia synthesis,

these compounds affect the adsorption capacity of N_2 on the catalyst. Whereas in irreversible poisoning, the poisons are strongly chemisorbed on the surface, and the catalyst activity is not regained by removing the poisons from the feed, but it may be regained with some other techniques. For example, Ashrafi et al., regained the initial catalyst activity of poisoned catalyst by temperature enhancement [23]. Table 2.5 shows the list of industrial catalytic reactions that are susceptible to poisonous compounds.

Table 2.5: Examples of poisonous industrial catalysts.

Process	Catalyst	Poison
Ammonia synthesis	Fe	CO, CO_2, H_2O, C_2H_2, S, Bi, Se, Te, P
Steam reforming	Ni/ Al_2O_3	H_2S, As, HCl
Methanol synthesis	Cu	H_2S, AsH_3, PH_3, HCl
Catalytic cracking	SiO_2- Al_2O_3, zeolites	Organic bases, NH_3, Na, heavy metals
CO hydrogenation	Ni, CO, Fe	H_2S, COS, AS, HCl
Oxidation	V_2O_5	As
Automotive catalytic converters (oxidation of CO and HC, NO reduction)	Pt, Pd	Pb, P, Zn
methanol oxidation to HCHO	Ag	Fe, Ni, carbonyls
Ethylene to Ethylene oxide	Ag	C_2H_2
many	transition metals	Pb, Hg, As, Zn

A number of researchers focused on poisoning of nickel metal catalysts by H_2S [76, 78, 79, 80, 52, 81, 82]. The studies on methane reforming on nickel catalysts by Rostrup-Nielsen suggests improvements against catalyst deactivation. A process named SPARG (Sulfur Passivated Reforming) has been commercialized by Haldor Topsoe A/S to protect catalyst from deactivation by coke deposition in natural gas steam reforming. In SPARG process, the formation of carbon is reduced by ensemble control, i.e., sites for carbon formation are blocked by sulfur species, while sufficient sites for steam reforming reactions are maintained. It has also been suggested that sulfur in liquid feed allows competition for metal sites between adsorbing sulfur atoms and coke precursors [83]. Studies on sulfur passivated catalysts of Pt, Pt-Ir, and Pt-Re on Al_2O_3 support indicates that the catalyst life can be improved by lowering the coke deactivation rate. Sulphur is adsorbed on the hydrogenolysis sites of platinum surface, later these sites are occupied by coke precursors. They have also concluded that the addition of small amounts of Ir or Re to Pt improves the sulfur tolerance [77].

2.3.1 Modeling of catalyst poisoning

In general the catalytic activity is proportional to the number of active sites [84]

$$k_{\text{obs}} = N_T k_{\text{intr}} \eta, \tag{2.20}$$

where k_{obs} ans k_{intr} are the observed and intrinsic rate constants for the reaction, N_T is the total number of active sites, and η is the effectiveness factor. Catalyst deactivation is caused by the decrease in number of active sites (N_T), a decrease in quality of active sites (k_{intr}), and a degradation in accessibility of the pore space. During the catalyst poisoning the the number of active sites are reduced by the strong adsorption of impurities on the active sites, which is given by

$$N_T = N_T \left(1 - \theta\right), \tag{2.21}$$

where θ is the fraction of sites occupied by the poisons. The intrinsic rate constant is affected by the presence of poisons in the feed. For example, the interaction of H_2S with transition metals leading to the formation of surface sulphides with a different activity than the fresh catalyst. The effectiveness factor is also influenced by poisoning.

2.4 Deactivation by solid phase transformations

Deactivation by phase transformations occurs at very high temperature and this can be viewed as extreme form of sintering. In this process phase crystallite is transformed into another. This phenomena can be observed in metal supported catalysts as well as metal oxide supports. In the first case, active metal on the support is transformed into inactive. For example, Nickel on Al_2O_3 is transformed into inactive nickel aluminate phase ($NiAl_2O_4$) at above 800 °C, and reaction of Rh_2O_3 with Al_2O_3 forms inactive $Rh_2Al_2O_4$. In the second case, the conversion of γ-Al_2O_3 with surface area 100- 200 m^2/gm is transformed into α-Al_2O_3 with low surface area 5 m^2/g. Table 2.6 shows the transformations of boehmite (Alumina oxide) to α- Al_2O_3 with respect to the temperature, α- Al_2O_3 is the non porous, which is the most stable phase of alumina with less surface area 5m^2/gm.

The solid phase transformations are also limited by rate of nucleation and occurs due to the presence of some

Table 2.6: Alumina oxide support transformations.

Form	Temperature(°C)	Surface area (m^2/g)
Boehmite	200 - 400	200 - 350
γ- Al_2O_3	600 - 800	100 - 200
δ- Al_2O_3	800 - 1000	-
θ- Al_2O_3	1000 - 1100	-
α- Al_2O_3	1100 - 1200	5

foreign compounds in the lattice or even on the surface. For example, V_2O_5 support accelerates the sintering process of titanium catalysts. TiO_2 on V_2O_5 support transforms the anatase phase into inactive rutile phase of TiO_2, but the addition of WO_3 support effectively increases the surface area for TiO_2 catalysts [21].

2.5 Other forms of deactivation

Other forms of catalyst deactivation include masking or pore blockage caused by the presence of poisonous substances in the feed. The deactivation occurs due to the physical deposition of substances on the external surface of the catalyst. This is observed in nickel and vanadium catalytic reactions, and deposition of phosphorus and silica on automotive exhaust converters.

Active metal loss through the formation of volatile compounds is another deactivation mechanism. Volatile compounds like metal carbonyls, oxides, sulfides and halides are formed in the presence of gas phase environment. This process is significant over a wide range of conditions. For example, loss of nickel in the presence of CO form nickel carbonyls at relatively low temperature, and at high pressures of CO(> 20kPa), ruthenium oxide is formed in the presence of oxygen environment, and volatile $CuCl_2$ is formed with copper catalyst in

the presence of chlorides. Bartholomew has proposed the following mechanism for the formation of volatile compound from the metal surface.

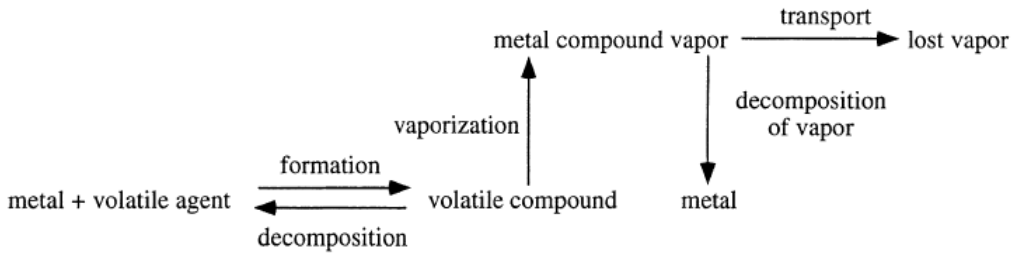

Finally, the loss of catalytic material is observed in different forms such as crushing of catalysts due to the load, produce fines due to the attrition in moving or fluidized beds, erosion of catalyst particles or monolith coatings occur at higher gas velocities, and sudden changes in temperature. The changes in temperature also leads to differences in thermal expansion between the washcoat and monoliths, which results in washcoat peel off from the surface.

2.6 Hydrogen sulfide chemisorption studies

The chemisorption of H_2S on Ni surface is extensively studied by variety of techniques such as LEED, Auger experiments, TPD/ TPR, HREELS, XPS, and AES [85, 79, 86, 80, 87]. Most of these methods deal with structural, electronic and vibrational properties of chemisorbed sulfur on different metals.

Zhou et al., reported the chemisorption of H_2S on clean and pre-adsorbed sulfur on Ni(100) by AES and TPD. They have found that the desorption of hydrogen from the surface is a strong function of H_2S exposure. At low H_2S exposure, H_2S is totally dissociated and H_2 is desorbed from the surface. But in the case of pre-adsorbed sulfur, the dissociation of H_2S is inhibited and also shifts the H_2 desorption to lower temperature [88]. The study by Hedge et al [89], on chemisorption of H_2S on clean and sulfur covered Rh(100) also led to the same conclusions as Zhou et al., and claimed that the initial sticking coefficient of sulfur on rhodium(100) surface is greater than 0.5 and constant up to 0.6 langmuir exposure. Langmuir (L) is unit of exposure or dosage to a surface. The high sticking coefficient indicates the involvement of a kinetically important weakly held molecular precursor state in adsorption process.

Alfonso et al., studied [90] H_2S adsorption and dissociation on different metal surfaces using DFT calculations. They found that H_2S molecule is weakly adsorbed on the on-top sites and dissociates into S, SH, and H species on the surface. In contrast to the H_2S, species H, SH, and S strongly interact with the surfaces. SH is preferentially adsorbed on bridge site, where as S and H are adsorbed on hollow sites. The dissociation of H_2S on all the metals is exothermic and energy barrier for dissociation is higher for Ag(111) and Au(111), intermediate for Cu(111) and lower for Ir(111), Ni(111), Pd(111), Pt(111).

Oliphant et al., reported on chemisorption of H_2S on different metals and concluded that supported Ni catalysts have strong affinity for H_2S chemisorption than unsupported Ni, Ru, Ni-Co, and Ni-Pt bimetallic

catalysts. H_2S chemisorption is strong and dissociative at lower coverages and non dissociative at higher sulfur coverages. If the surface is saturated with sulfur it may form nickel sulfide or bulk sulfide [79]. Maraecot et al., observed two types of sulphides on Ni catalyst surface at 323 K. They found that after the formation of superficial metallic sulphides, sulfur quickly forms polysulphides on the surface or slowly attacks deeper layers and forms bulk sulphides. Furthermore, the relative amounts of these two sulfur species strongly depends on the ability of the nickel catalyst to dissociate the poison molecule and to form superficial polysulfides or bulk sulfides.

The earlier studies by Besten et al., [91], suggested that H_2S forms four chemisorption bonds with the nickel at lower coverages, and two nickel atoms are required at higher coverages. They found that hydrogen desorption from the catalytic surface depends on the sulfur coverages. If the coverage is low, the dissociated hydrogen is quickly adsorbed on bare sites, but at high coverage the dissociated hydrogen is forced out to the gas phase as the sulfur atoms are adsorbed. If the Ni surface is completely saturated with sulfur, it is found that about two-thirds of the total hydrogen may be removed, even at 400 °C. These results are confirmed with deuterium exchange experiments and suggested that two differents types of chemisorption bonds are formed with Ni surface depending on the sulfur coverage. At higher coverages, it appears that the hydrogen cannot be removed below the sulphide layer, as it acts as a barrier and prevents diffusion of hydrogen to, and from the surface.

at lower coverages

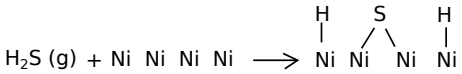

at higher coverages

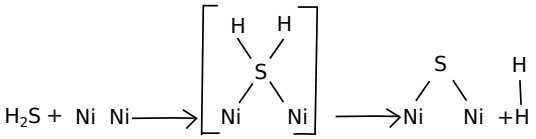

Most of the previous chemisorption studies discussed above are carried out at low temperatures and they concluded that H_2S requires two or four nickel atoms for chemisorption. Rostrup-Nielsen et al., [80] reported the chemisorption studies of H_2S on nickel catalyst at higher temperatures (550- 645 °C). They found that sulfur uptake depends on p_{H_2S} and p_{H_2} as well as on the p_{H_2S}/p_{H_2} ratio. A saturation layer is obtained at p_{H_2S}/p_{H_2} ratios above 5×10^{-6}, which is independent of the amount of sulfur added. Furthermore, it is indicated that an abrupt increase in the sulfur uptake occurs when the H_2S/H_2 ratio exceeds the value for the formation of bulk sulphide (Ni_2S_3), which is predicted from thermodynamics ($p_{H_2S}/p_{H_2}=10^{-3}$), and also identified by X-ray analysis. The following chemisorption mechanism involving of one nickel site is proposed by Rostrup-Nielsen for temperatures above 400 °C.

$$H_2S(g) + Ni \leftrightarrow Ni - S + H_2(g) \tag{2.22}$$

The saturation sulfur coverage and equilibrium coverages are dependent on the $H_2S/\ H_2$ ratio and temperature [80]. In another study by Alstrup et al. [81], sulfur chemisorption isobars were measured in the temperature range of 773 - 1023 K with H_2S/H_2 ratio 7-50 ppm. They have indicated that for up to 90% of saturation,

the H_2S/H_2 ratio can be calculated using simple expression relating entropy, coverage, and enthalpy (or heat of adsorption)

$$\frac{p_{H_2S}}{p_{H_2}} = \exp\left[\Delta H_0^0 (1 - \alpha\theta) RT - \frac{\Delta S^0}{R}\right], \tag{2.23}$$

with ΔH_0^0 = -289 kJ/ mol, ΔS^0= -19 kJ/ mol and α = 0.69, $\theta = s/s_0$ where s and s_0 are actual and saturation amounts of sulfur respectively. The high temperature data of the published sulfur chemisorption measurements are well described by Eq. 2.23. It is suggested that the absence of coverage dependence in the entropy term is due to the subsurface chemisorption. Constant entropy resembles gas/solid solution equilibrium or bulk-like behavior of the chemisorbed layer. Eq. 2.23 can be rearranged to give the surface coverage of sulfur as

$$\theta_s = 1.45 - 9.53 \times 10^5 T + 4.17 \times 10^5 T \ln\left(\frac{p_{H_2S}}{p_{H_2}}\right) \tag{2.24}$$

This expression is not valid for θ_s close to zero and one. Changes in the saturation level are very small at the higher temperatures but become significant at the lower temperatures. So, as the poisoning process is represented by a simple exothermic adsorption process, the sensitivity of the reforming catalyst to poisoning increases at lower operating temperatures. For example, while poisoning of the (nickel) catalyst occurs with about 5 ppm of sulfur in the feed gas at a temperature of 800 °C, concentrations of the order of 0.01 ppm poisons the catalyst at 500 °C [92, 21].

Chapter 3

Biogas steam reforming: Experimental investigation

The objective of this chapter is to examine experimentally the biogas steam reforming in the presence of hydrogen sulphide. Model biogas with different levels of H_2S is subjected to reforming reaction over supported Ni catalyst in fixed bed reactor at 700 and 800 °C. In order to understand the poisoning effects of H_2S the reactions are initially carried out without H_2S in the feed stream. Three different H_2S concentrations (20, 50, and 100 ppms) are considered in the study. The H_2O to CH_4 ratio is maintained in such a way that CO_2 also participates in the reforming reaction. After performing the poisoning studies, regeneration of the catalyst is attempted by three different techniques.

3.1 Basic reactions

The major reactions that occur during biogas reforming are i)steam reforming

$$CH_4 + H_2O \rightleftharpoons CO + 3H_2 \quad \Delta H^0_{298} = +206 \text{ kJ/mol} \tag{3.1}$$

$$CH_4 + 2H_2O \rightleftharpoons CO_2 + 4H_2 \quad \Delta H^0_{298} = +165 \text{ kJ/mol}, \tag{3.2}$$

ii) water gas shift reaction

$$CO + H_2O \rightleftharpoons CO_2 + H_2 \quad \Delta H^0_{298} = -41 \text{kJ/mol}, \tag{3.3}$$

and iii) dry reforming reaction with CO_2

$$CH_4 + CO_2 \rightleftharpoons 2CO + 2H_2 \quad \Delta H^0_{298} = +247 \text{kJ/mol}, \tag{3.4}$$

which plays a minor role when enough H_2O is available. Even though the dry reforming reaction tends form coke, it can be suppressed by adding small amounts of H_2O. The syngas composition that results from reforming of biogas at a fixed temperature depends on S/CH_4 ratio as well as CO_2/CH_4 ratio.

3.2 Catalyst preparation

Initially the γ-Al_2O_3 (Alfa Aesar) supports are calcined in air at 800 °C and held for 4 h to remove any volatile components present in the supports. The physical properties of γ-Al_2O_3 as received are shown in table 3.1. The nickel metal catalysts supported on γ-Al_2O_3 are prepared by wet impregnation method using nickel

Table 3.1: Physical properties of γ-Al_2O_3 supports.

Surface area	253 m^2/g
Packing density	0.402 g/cm^3
Total pore volume (Hg)	1.14 cm^3/g
Median pore diameter	118 A^0
Length (average)	5.1 mm
Diameter (average)	3.3 mm

(II) nitrate hexahydrate ($Ni(NO_3)_2$ $6H_2O$, Merck, 98.9% purity) as nickel precursor. Measured quantities of metal precursor equivalent to the desired metal loading (15 wt%) is first dissolved in distilled water of volume equal to or slightly excess of the total pore volume of the support. The precursor solution is slowly added to the γ-Al_2O_3 supports and stirred continuously for two hours to ensure uniform mixing. The wet material is subsequently dried overnight at 100 °C for 12 hours in a hot air oven, and followed by calcination at 800 °C in presence of air for about 6 hours. Enough catalyst is prepared in one batch and used throughout the experiments to ensure consistency in the results. The 15% nickel loading is calculated according to the following equation.

$$\text{Amount precursor required} = \frac{0.15}{1-0.15} \times \frac{W_{Ni(NO_3)_2 6H_2O}}{W_{Ni}} \times \text{weight of support.} \tag{3.5}$$

where $W_{Ni(NO_3)_2 6H_2O}$ and W_{Ni} are the molecular of weights of nickel nitrate hexahydrate and nickel respectively. The amount of distilled water to be added to the precursor salt is calculated according to

$$\text{Amount of water required} = \text{pore volume} \times \text{weight of support} \tag{3.6}$$

3.3 Catalyst characterization

The fresh and spent catalysts are characterized by various techniques, including surface area and porosity analyer, temperature programmed reduction (TPR), pulse chemisorption, and powder X-Ray diffraction (XRD).

3.3.1 X-ray powder diffraction (XRD)

X-ray powder diffraction (XRD) is a rapid analytical technique primarily used for phase identification of a crystalline material and can provide information on unit cell dimensions. It is also possible to roughly estimate the average crystallite size. XRD analysis of catalyts are performed on the Philips Xpert Pro instrument (X-Pert PRO PANalytical) between 10−90 degrees using CuK_α radiation (λ =0.15418 nm) at 40 kV and 30 mA, with a scanning rate of $2\theta = 0.067°$. The crystallographic phases are identified by using the software PDFWIN. This software is based on diffraction data from International Centre for Diffraction Data (ICDD).

The crystal size of the catalysts is calculated using the Debye− Scherrer equation and the XRD spectra. The mean size (D) of the crystallite in the catalyst is determined using the following equation

$$D = \frac{k\lambda}{\mathrm{B}_{1/2}\mathrm{Cos}(\theta)} \tag{3.7}$$

where k is a constant ranging between 0.9 to 1.0, λ is the wave length of X-Ray (A^o), θ is the angle of incidence in radians, $B_{1/2}$ is measured angle from the diffraction pattern figure obtained at the different 2θ angles (degrees), as it can be approximated as line broadening at half of the maximum intensity. In general, a broader peak means that the corresponding crystallite present is of relatively small particles and a sharp peak usually is attributed to crystallites of relatively large size.

3.3.2 Surface area and porosity measurement

Micrometrics ASAP 2020 analyzer is used to measure the BET surface area, average porosity, and pore size distribution of fresh catalyst sample and spent catalysts. This analysis is essentially an adsorption-desorption phenomena.

Before the analysis, the sample needs to be degassed to remove impurities, such as air and other gases. The sample is degassed under high vacuum at 250 °C and for 1 hour. After degassing the amount of the catalyst in the cell is weighed and loaded to the analysis port of the equipment. Dewar flask is filled with liquid nitrogen and kept under analysis port to maintain the cell temperature at −196 °C. The amount of nitrogen gas adsorbed at various relative pressures is measured. From the obtained data a plot of p/p_0 vs $1/[w((p_0/p) - 1)]$ is drawn and surface area is calculated using BET equation. The linear relationship of this equation is maintained only in the range of $0.05 < p/p_0 > 0.35$, where p and p_0 are the equilibrium and the saturation pressure of adsorbates at the adsorption temperature, and w is the quantity of volume adsorbed.

Similarly, a sample of porous material is characterized by its distribution of pore sizes. Each pore size contributes to the total adsorption isotherm in proportion to the fraction of the total area of the sample. Isotherms of mesoporous materials are measured over a pressure range of 1 torr to approximately 760 torr. Once details of the isotherm curve are accurately expressed as a series of pressure vs. quantity adsorbed data pairs, a number of different methods (theories or models) can be applied to determine the pore size distribution. Barrett, Joyner and Halenda method (BJH), and T-Plot analysis is used to calculate the pore size.

3.3.3 Temperature programmed reduction

Temperature programmed reduction (TPR) is employed mainly to study the reduction behavior of metals present on the support. The data obtained from TPR is useful to estimate reduction temperatures, degree of reduction, metal-support interactions and any important findings related to the interaction of metal with other metals and support. The reduction temperature depends on the degree of interaction between the active metal and the support. Stronger interactions lead to higher reduction temperatures. TPR studies are carried out in a AutoChem II 2920 (Micrometrics, USA). A measured amount of fresh catalysts is loaded in a quartz tube supported on the quartz wool. Sample preparation includes heating the catalyst to 200 °C with a ramp rate of

10 °C/min, and holding it at that temperature for 1 h in argon stream with a flow rate of 30 ml/min to remove any absorbed moisture, after which the catalyst is cooled to 50 °C. After sample preparation, the catalyst is heated to 900 °C at a ramp rate of 10 °C/min in 10% H_2 in argon mixture. The consumption of hydrogen is monitored with a thermal conductivity detector (TCD).

3.3.4 Pulse chemisorption

Pulse chemisorption measures the metal dispersion in the catalyst support. Dispersion is the fraction of active metal atoms exposed or is accessible to the reacting species. It is a critical parameter for catalyst activity since only atoms which are exposed can take part in the surface catalyzed reactions. Due to the high temperatures encountered in different steps (calcination, reduction, reaction) during the catalyst preparation, some of the metal particles may become inaccessible to the reactants due to migration into the support bulk, formation of a new product, sintering, etc. 10% H_2 in argon mixture is used to carry out the experiment and the amount of H_2 chemisorbed is used to determine the exposed metal atoms in the catalyst. A measured amount of fresh catalysts is loaded in a quartz tube supported on the quartz wool. The catalyyst is reduced with 10 vol% H_2 in argon with a flowrate of 30 ml/ min. After completion of reduction, the sample is cooled down to ambient temperature with argon carrier gas and the flow is continued for another 30 min to remove any traces of hydrogen. Pulses of the 10% H_2 in argon mixture are dosed repeatedly until the catalyst surface is saturated (Fig. 3.1).

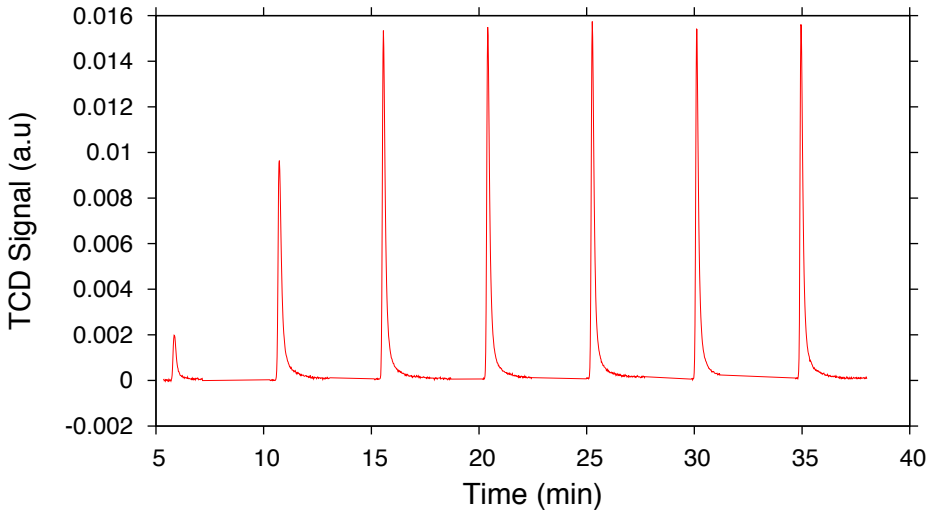

Figure 3.1: Pulse chemisorption trend for 15% Ni reduced catalyst.

The total amount of H_2 chemisorbed is measured using a thermal conductivity detector (TCD) and the metal dispersion can be calculated as [93],

$$\text{Percent metal dispersion} = \frac{M(V_s\, SF_{\text{cal}})}{S_w V_{\text{ideal}}} \times 100, \tag{3.8}$$

where M is the molecular weight of Ni, V_s is the volume adsorbed in cm^3 at STP, SF_{cal} is the calculated stoichiometry factor, S_w is the sample weight, and V_{ideal} is the the molar volume of an ideal gas (22414 cm^3)

at STP.

3.4 Experimental rig

A schematic representation of the experimental rig used for biogas steam reforming is shown in Fig. 3.2. The following sections briefly explain the system configurations.

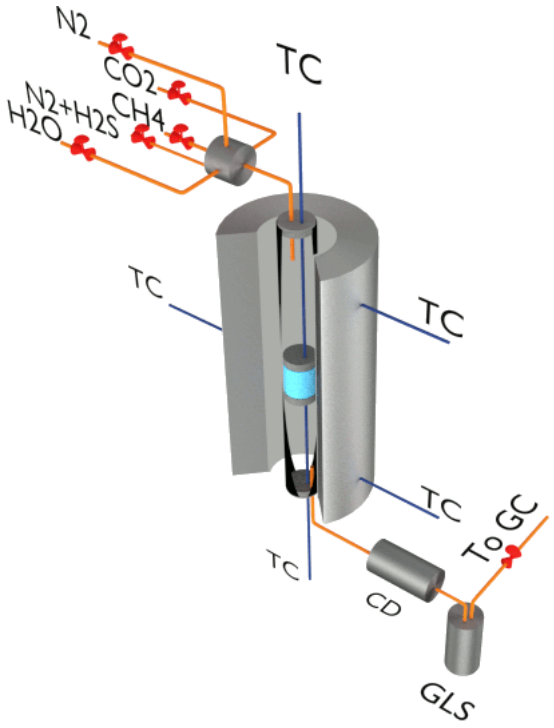

Figure 3.2: A schematic representation of reactor used for experiments. The abbreviations used are as follows: Thermocouple (TC), Gas-Liquid separator (GLS), Condenser (CD), Gaschromato- graph (GC).

3.4.1 Reactor

The reactor section consists of a high temperature tubular reactor inside a furnace and a temperature controller to control the temperature of the catalyst bed. A 40 cm long quartz tube having 18 mm ID and 22 mm OD forms the reactor. The two ends of the quartz reactor are fitted with stainless steel clamps with the help of graphite gaskets. Two Ni-Cr thermocouples are inserted in to the catalyst bed at the top and bottom through 0.32 cm bored-through fittings. The furnace used in the reactor set-up has three split zones (Series 3220, Applied Test Systems, USA). The first zone serves as a preheating section, second zone maintains the isothermal conditions for the catalyst bed, and third zone maintains the reactor temperature to avoid condensation within the reactor. The three zones of the furnace heater are controlled using digital controllers, and the temperatures of the three zones are adjusted based on the bed temperature at the top and the bottom. By maintaining these temperatures the entire quartz reactor is maintained at a desired reaction temperature.

Initially the reactor is heated to the desired reaction temperture with a ramp rate of 10 °C per minute under inert N_2 flow (99.999% pure, Prax air). Prior to the reactions the nickel catalysts are reduced in pure H_2 flow

20 ml/min at a temperature of 800 °C for about 5 hours. Before starting the reaction, water is fed using a calibrated HPLC pump through a preheating zone heater for 5 min to fill the liquid line. Pure gases of CH_4 (99.999%) and CO_2 (99.995%) are fed to the reactor using calibrated mass flow controllers with N_2 dilution. The gas mixture is heated to 250 °C in a preheating zone before entering the reactor hot zone.

3.4.2 Catalyst loading

Maintaining the location of the catalyst bed within the reactor is critical for reproducible data. For obtaining consistent reading the length of the bed is kept constant and so is the distance of the bed from one of the ends of the reactor. In this work, the reactor is loaded with 1.5 g of catalyst pellets diluted with quartz beads (3 mm to 5 mm diameter) and total length of the bed is maintained at ~6 cm and it is placed exactly at middle zone of the furnace. The catalyst bed is placed such that the temperature measurements are possible at the top and bottom of the bed. Care must be taken to obtain an ideal fixed bed reactor system. The ideal fixed bed configuration requires the catalyst bed to be placed on top of a flat surface and also to have a flat top. For this reason, the catalyst bed is placed in between the fine quartz wool.

3.4.3 Flow controllers

An HPLC pump (Series I, Lab alliance, USA), and calibrated mass flow controllers (Bronkhorst High Tech, The Netherlands and Alborg, USA) respectively controls the flow of liquid water and gases into the reactor. The HPLC pump for liquid water has a flow range of 0 to 5 ml/min with an accuracy of 0.01ml/min. The water flowrate is maintained at 0.036 ml/min throughout the experiments. The outlet of the HPLC pump is connected to microbore tubing in order to create sufficient pressure drop so that selected amount of liquid flow can be injected. The gases and water enter the reactor through different lines. 1/4 inch lines are used for gases and 1/8 inch line for liquid. Each line is fitted with a non-return valves to avoid any back flow due to pressure build up in the system. Pressure gauges are installed on each line to monitor the pressure. The inert gas feed lines have 7 µm size filters installed between the gas cylinder and the mass flow controller. Initially the mass flow controllers are calibrated with actual gas reactants. The range of mass flow controllers for CH_4, N_2, H_2 and CO_2 is 0- 200 ml/ min with minimum accuracy of 1%, while H_2S/N_2 mixture mass flow controller range is 0- 20 ml/min with an accuracy of 1%. The inert gas N_2 served both as the internal standard for the gas chromatograph and as a carrier gas through the reactor system.

MFC calibrations

The mass flow controllers are calibrated in the range of flow necessary for the desired feed conditions. Actual flow rates are measured at the out let of the MFC with the help of manual soap bubble meter as well as digital soap bubble meter (Smarttech instruments, India). The following Table 3.2 gives actual flowrate equation constants from respective mass flow controller in the form of $F_{act} = aF + b$, where F_{act} is actual flow from MFC in ml/min, F is the set point of MFC, and a and b are the constants for the respective controller.

3.4.4 Steam generation and gas preheating

Vaporization of water is accomplished using heating tape wrapped around the feed lines. Sufficient length of the water line wrapped with heating tapes ensure the complete vaporization of water before entering into the

Table 3.2: MFC actual flow equation constants in the form of $F_{act} = a\ F + b$.

Species	a	b
CH_4	0.8373	2.0242
CO_2	1.1181	-1.8987
N_2	1.0611	6.9020
H_2S	1.0860	-0.3759

preheating zone of furnace heater. The temperature of all the feeding lines are maintained at 250 °C, which is controlled by a K-type thermocouple and a controller. The vaporized water and preheated gases are mixed together in a cross connection near the reactor inlet.

3.4.5 Condenser and gas liquid separator

A condenser is required to condense any unreacted water that comes out of the reactor. The condenser is made of stainless steel with inside spiral coil of surface area 160 cm^2. The shell side of the condenser is maintained at O °C using a chiller (Zulabo, Germany) and the effluent coming out from the bottom of the reactor is passed through a coiled section of the condenser using 1/4 inch OD SS 316 line. The gases and condensed water are separated in one side torispherical head closed gas liquid seperator. The left over uncondensed water vapor from the condenser is condensed in the gas liquid seperator, which also has a provision to maintain shell side temperature at O °C by using a chiller. The effluent gases leaving this section are passed throgh a moisture trap to remove trace amounts of water vapor. The dry gases are then directed to online GC for analysis.

3.4.6 Gas analysis

The gases leaving the reactor system mainly contains H_2, CO, CH_4, CO_2 and N_2. These gases are directed to the online GC 2014 (Shimadzu Corporation) equipped with a themal conductivity detector (TCD) for analysis. The sampling is done with gas sampling valve (MGS-5, Shimadzu). The gas sampler is used to introduce gas samples through manual operation, under ambient temperature conditions. The sample volume is selectable in 1, 2, or 5 milliliters by valve operation. In our experiments 1 ml loop is operated throughout the experiments. Carboxane packed column of inner diameter 3.17 mm and length 4.5 m is used for gas seperation. The injector port temperature, column temperature, and TCD temperature are maintained at 150 °C with TCD current of 60 mA. Argon is used as a carrier gas for GC for detecting all the components. The product gas sample is injected for every 15- 30 mins untill steady state is reached. i.e., constant chromatogram areas for all the components.

3.4.7 Process automation

SCADA software is used for online control of system for gas flow, liquid flow, reactor furnace temperature, reactor upstream and down stream pressures, pressure control system, and catalyst bed temperature.

3.5 Catalyst testing

This section briefly explains the different sets of experiments carried out just for the sake of explaining the results of catalyst characterization. Three sets experiments are carried out for biogas steam reforming.

(i) Catalyst stability test at 700 °C and 800 °C in the absence of H_2S in the feed gas

(ii) Catalyst poisoning with 20, 50, 100 ppm of H_2S in the feed stream.

(iii) Catalyst regeneration by different techniques.

Table 3.3 shows the actual flow rates of reactants which are maintained throughout the experimental studies.

Table 3.3: Reactant flow rates in ml/min at NTP.

Species	Flow rate (ml/min)
CH_4	23.794
CO_2	15.99
N_2	102.4
H_2O	0.036 (liquid)

The above flow rates gives CH_4/CO_2 ratio is 1.487. This composition corresponds approximately to mean values of the biogas (CH_4/CO_2 ratio is ~1.5).

S/C ratio

Steam to carbon (S/C) ratio in the reformer is defined as

$$\text{S/C} = \frac{\dot{n}_{H_2O}}{\dot{n}_{CH_4}} \left[\frac{\text{mole}}{\text{mole}}\right] \tag{3.9}$$

where $\dot{n}_{H_2O}$ and $\dot{n}_{CH_4}$ are the molar flow rates of steam and CH_4 respectively. Biogas mainly contains CH_4 and CO_2, while calculating S/C only organic carbon is considered. A low S/C = 2.02 is employed throughout the experimental studies to ensure the participation of CO_2 in reforming reactions.

Catalyst stability tests are caried out at temperature of 700 °C and 800 °C. The main purpose of the stability test is to evalute the catalyst performane during reforming of H_2S free biogas. The reaction is carried out for ~ 12 h at 700 °C and for ~22 h at 800 °C. In second set of experiments, the biogas steam reforming reaction is performed with out H_2S until steady state and once the steady state is reached H_2S is introduced into the reactor from a cylinder containing 1052 ppm H_2S diluted with N_2. All the experiments with H_2S are repeated to ensure reproducibility of the results. The reforming reactions are continued in the presence of H_2S and sampling is done for every 15-30 min until a new steady state is reached. In regeneration experiments, the totally poisoned catalyst is regenerated by.

- removing of H_2S from feed stream
- temperature enhancement
- steam treatment followed by reduction in H_2

3.6 Calculations

The gas chromatograph calibrations are performed using a constant flow rate of ~100 sccm of different concentrations of individual gases diluted in nitrogen. Response factors of each species are generated from the GC chromatographs. For example CH_4 response factor is calculated based on the following.

Chromatographs of different compositions of CH_4 balanced with N_2 are generated and corresponding areas are measured. Once the areas are known at different compositions the response factor for individual composition is calculates as

$$\frac{Y_{CH_4}}{Y_{N_2}} = \alpha_{CH_4} \times \frac{A_{CH_4}}{A_{N_2}} \tag{3.10}$$

where Y_{CH_4} and Y_{N_2} represnts the mole fractions of CH_4 and N_2 respectively, α_{CH_4} is the response factor CH_4, and A_{CH_4} and A_{N_2} are the chromatogram area of CH_4 and N_2 respectively. The above equation can be written as

$$\alpha_{CH_4} = \left(\frac{n_{CH_4}}{n_{N_2}}\right) / \left(\frac{A_{CH_4}}{A_{N_2}}\right) \tag{3.11}$$

where n_{CH_4} and n_{N_2} represents the moles of methane and nitrogen. The above procedure is repeated for all the compositions and average response factor of CH_4 is calculated. The similar procedure is adopted for all other reactant and product gases. The response factor of each component is listed in Table 3.4.

Table 3.4: GC response factors (α) of individual components.

Species	α
CH_4	0.382137
H_2	0.085576
CO	0.833152
CO_2	1.324115

N_2 component calibration is done by injecting different volumes of N_2 into the GC and measuring corresponding chromatogram areas. The generalized equation is developed for unknown moles of N_2 in the gas mixture given by

$$n_{N_2} = 7 \times 10^{-11} \times A_{N_2} \tag{3.12}$$

The unknown moles of CH_4 in the gas mixture is then calculated according to

$$n_{CH_4} = \alpha_{CH_4} \times \left(\frac{A_{CH_4}}{A_{N_2}}\right) \times n_{N_2} \tag{3.13}$$

The conversion of methane is calculated as

$$X_{CH_4} = 1 - \frac{n_{CH_4}}{n_{CH_{4,0}}} \tag{3.14}$$

where $n_{CH_4,0}$ is the initial moles of methane in the reaction mixture and n_{CH_4} is the moles of methane in the product stream.

3.7 Mass balance

Here, it is assumed that the reaction of inlet gases produces a mixture of CO, CO_2, H_2, CH_4, H_2O and solid C. The calculations of all outlet flow rates are based on the assumption that carbon, oxygen and hydrogen mass balance equations are given by equations that are presented in the following.

Carbon balance

$$[CH_4]_{in} + [CO_2]_{in} = [CO]_{out} + [CO_2]_{out} + [Carbon]_{out} \tag{3.15}$$

Oxygen mass balance

$$[H_2O]_{in} + 2[CO_2]_{in} = [CO]_{out} + 2[CO_2]_{out} + [H_2O]_{out} \tag{3.16}$$

Hydrogen balance

$$2[CH_4]_{in} + [H_2O]_{in} = 2[CH_4]_{out} + [H_2O]_{out} + [H_2]_{out}. \tag{3.17}$$

Where $[\ ]_{out}$ and $[\ ]_{in}$ are outlet flow rates [mol/h] and inlet flow rates [mol/h], respectively.

The outlet gas from the reactor passes through the condenser and gas liquid seperator to remove unreacted H_2O. Thus, the gas passing the gas analyser contains only H_2, CO, CO_2, and unreacted CH_4. These components are related by the following equation:

$$[H_2]^{mf}_{out} + [CH_4]^{mf}_{out} + [CO]^{mf}_{out} + [CO_2]^{mf}_{out} = 1. \tag{3.18}$$

Where $[\ ]^{mf}_{out}$ are water free mol fractions (dry mole fractions) of the outlet stream and are given through gas analyser results.

Carbon deposition is one of the main factors of catalyst deactivation. The deposited carbon amount can be calculated using the mass balance equations above. Since no carbon deposition and catalyst deactivation was observed during the stability at 700 °C and 800 °C, $carbon_{out}$. Formation of carbon is assumed to be zero throughout the calculations.

3.8 Results and discussion

3.8.1 XRD- phase identification

The γ- Al_2O_3, the catalyst calcined at 800 °C, and fresh reduced catalyst with hydrogen are characterized to get an insight into the phases present. XRD is also useful in estimating the crystallite sizes of the different phases using the Scherrer equation. The XRD patterns of these catalysts are shown in Fig. 3.3. The calcined catalyst shows NiO peaks at 37.26 and 66.12 degrees, and $NiAl_2O_4$ is observed at 45.62 degrees. The formation of nickel aluminate is attributed to the close interaction between NiO and Al_2O_3 support at a high temperatures (>800 °C) according to

$$NiO + Al_2O_3 \rightleftharpoons NiAl_2O_4 \tag{3.19}$$

The presence of $NiAl_2O_4$ in Fig 3.3 indicates strong metal support interaction. However, a careful examination of the γ- Al_2O_3 and calcined samples reveals that there is an intensity increase at the 2θ values slightly

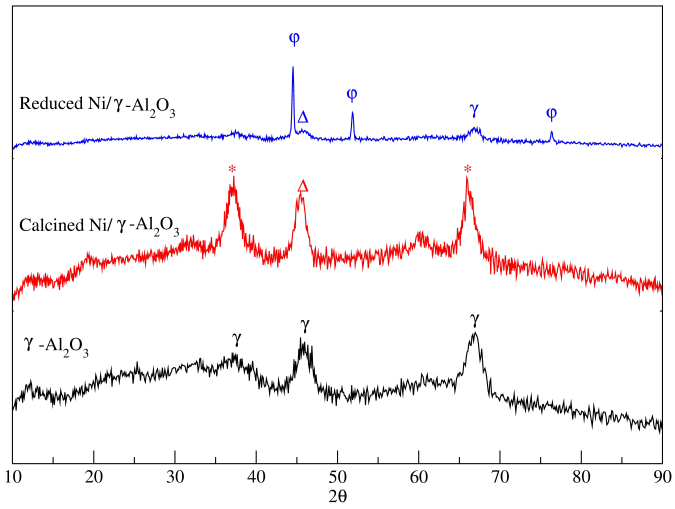

Figure 3.3: XRD patterns of γ-Al_2O_3, calcined Ni/Al_2O_3, and reduced Ni/Al_2O_3. Symbols represents the crystalline phases γ -Al_2O_3, $\star$- NiO, φ- Ni, and Δ- $NiAl_2O_4$.

lower than the 2θ of the γ-Al_2O_3 peak. It has been reported that γ-Al_2O_3 has a pseudospinel structure and its lattice parameters are very close to that of $NiAl_2O_4$, with 2θ shifted slightly to higher values [94]. After reduction of the Ni/γ-Al_2O_3 at 800 °C for 5 hr, nickel shows (1 1 1), (2 0 0) and (2 2 0) faces and are clearly visible respectively at 2θ of 44.6, 51.90 and 76.42 degrees. The peak intensity of $NiAl_2O_4$ is reduced compared to the calcined catalyst. Alumina crystallite phase is also observed at 2θ of 67.24 degrees. The absence of NiO indicates that NiO is completely reduced to metallic nickel during reduction with H_2.

Spent catalysts are characterized using XRD analysis and the results are shown in Fig. 3.4 The figure shows the XRD patterns of catalyst after stability at 800 °C without H_2S, reforming in the presence of H_2S with temperature enhancement (catalyst regeneration), and complete catalyst poisoningat 700 °C with H_2S.

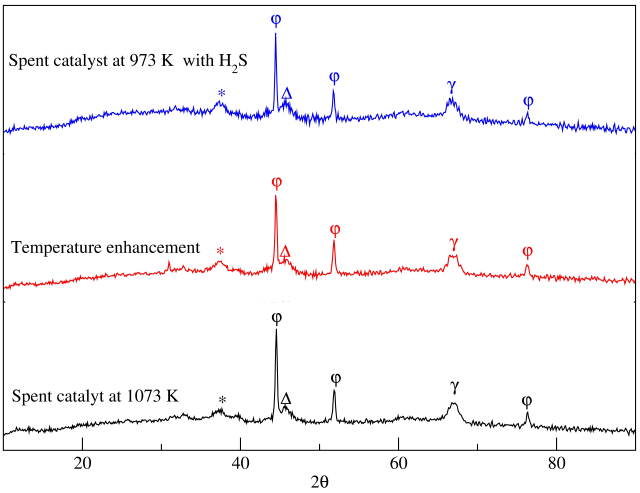

Figure 3.4: Spent catalyst XRD patterns of stability at 1073 K, temperature enhancement and poisoned catalyst at 973 K. Symbols represents the crystalline phases γ- γ-Al_2O_3, $\star$- NiO, φ- Ni, and Δ- $NiAl_2O_4$.

A nearly identical set of XRD patterns are observed for the fresh and spent catalysts. It is observed that support alumina unchanged position at 2 θ value for different spent catalysts as well as in fresh catalysts. It also shows that these peaks remain intact even after reaction, indicating the stability of the support during reactions at high temperatures. The peak at 37.26 degrees corresponds to NiO, observed for all Ni-containing catalysts, which indicates that metallic Ni is oxidized into NiO in the the presence of steam that is not observed in XRD pattern of fresh reduced catalyst. The diffraction patterns for NiS and Ni_2S_2 are not observed for the spent catalyst at 700 °C with 100 ppm H_2S exposure even though the catalyst is almost fully poisoned. A similar XRD pattern is also observed by Kuhn et al., for Ni-YSZ sample exposed to 100 ppm H_2S [95]. The absence of stable compounds of NiS or Ni_3S_2 in the XRD pattern is not surprising as these are expected to form only at high concentrations of H_2S in the feed. The diffraction peak for graphite carbon at 26.50 degrees is not observed for spent catalyst at 700 °C and 800 °C, which confirms the absence of coke formation during the reforming reactions.

3.8.2 BET area and pores size distribution

Figure 3.5 shows the N_2 adsorption/desorption isotherms of the fresh and spent catalyst at 1073 K, The N_2 adsorption/desorption isotherms are of type IV; they are presented as a hysteresis loop H_2 type, which is typical for mesoporous material. Figure 3.6 shows the the pore size distribution of the fresh and spent catalysts; both follows a normal distribution and that the mean pore size is less than 20 nm. The maximum value on the pore size distribution of the spent catalyst shifts from 15 nm to 18.3 nm and is about 3.3 nm larger than the fresh catalyst. The distribution of pores larger than 20 nm is similar for both the fresh and the spent catalysts.

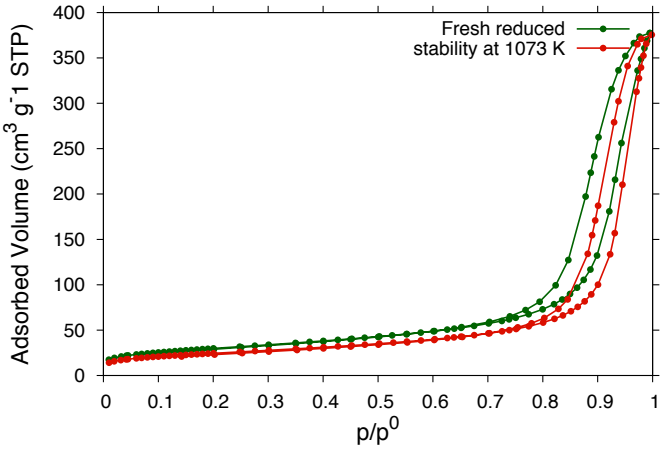

Figure 3.5: N2 adsorption-desorption isotherms of reduced catalyst and spent catalysts.

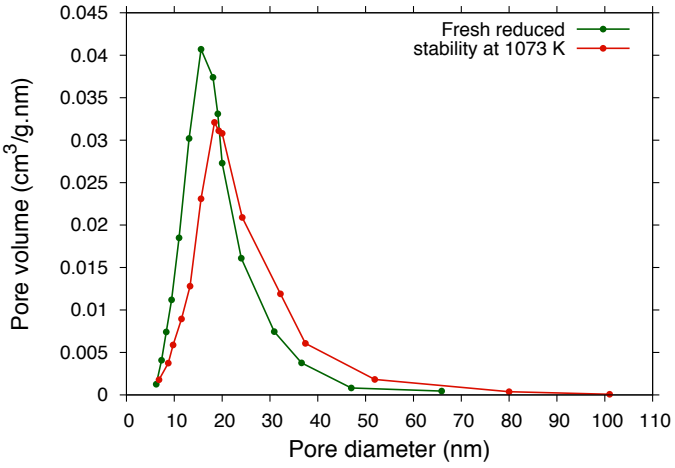

Figure 3.6: Pore diameter distribution of fresh and spent catalysts.

The BET surface area of calcined γ-Al_2O_3, reduced catalyst, and spent catalysts are shown in Table 3.5. The calcined and reduced catalysts show lower surface area compared to γ-Al_2O_3. The reduction in surface area is probably due to pore blockage. Moreover, the fresh reduced catalyst shows lower surface area than the calcined catalyst. This may be due to sintering of nickel metal particle during reduction at 800 °C for 5 h. It is also observed that spent catalysts shows less surface area than the fresh reduced catalyst. The pore volume is lower in the case of calcined and reduced catalysts compared to the γ- Al_2O_3 support. This may be due to the the blockage of pores with metallic nickel particle.

Table 3.5: BET Analysis of catalyst samples before and after experiments.

Sample	BET surface area (m^2g^{-1})	Pore volume (cm^3g^{-1})	Average pore Size (nm)
Calcined γ-Al_2O_3 at 800 °C	206	0.793	11.34
Calcined Ni/γ-Al_2O_3	151	0.626	12.09
Reduced Ni/γ-Al_2O_3	106	0.585	17.30
Spent catalyst after stability test at 800 °C	86	0.581	21.11
Spent catalyst at temperature enhancement	93	0.573	9.54
Spent catalyst at 700 °C	76	0.433	17.66

3.8.3 TPR studies

Fig 3.7 shows the TPR profile for 15% Ni loaded catalyst. The peak temperature is observed in the range of 780-800 °C. The higher reduction temperature indicates strong interaction NiO with γ-Al_2O_3 support. This is also normally attributed to the reduction of Ni aluminate ($NiAl_2O_4$), a surface spinel species formed by the diffusion of NiO into the support alumina. Similar type of TPR behavior is observed by Chen et al., [96]. Formation of $NiAl_2O_4$ occurs at calcination temperatures higher than 700 °C with NiO diffusing into the surface of support. There are no low temperature peaks found around 400−450 °C, which indicates that the sample is deprived of any free NiO dispersed on the support.

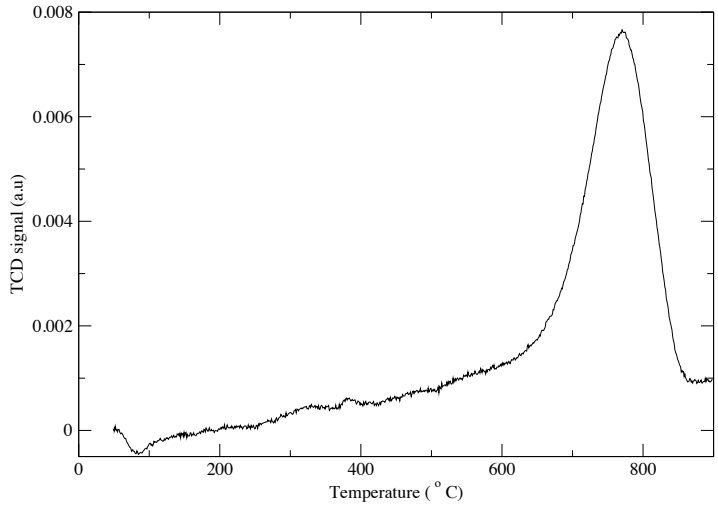

Figure 3.7: TPR profile for 15% Ni/γ-Al_2O_3 calcined at 800 °C.

3.8.4 Pulse chemisorption

Nickel metal dispersion and metallic surface area are determined by assuming an adsorption stoichiometry Ni/H ratio of 1 [97]. The mean size of the nickel particles is calculated from hydrogen adsorption [98]. H_2 pulse chemisorption results for Ni/Al_2O_3 reduced at temperature of 800 °C for 15 wt% Ni loading gave 3% metal dispersion, metallic surface area of 19.9 m^2/g.metal and cubic crystallite size of 28.1 nm.

3.9 Activity tests

3.9.1 Stability tests

In order to ensure that the catalyst does not lose activity over time in non poisoning atmosphere (without H_2S) reforming experiments are performed for 22 h at 800 °C. Fig. 3.8 shows the conversion of CH_4 and CO_2 on dry basis during the catalyst stability test at 800 °C. All data reported in this thesis is on dry basis and the lines are just drawn to guide the eye. The reactor exit compositions for the stability test are shown in Fig. 3.9. The constant conversion and product composition implies that the catalyst is stable and the activity remains constant under non-poisoning gas atmosphere. The H_2 to CO ratio in the product gas for the given inlet composition is ~3.

The stability test is also carried out at 700 °C and the conversions of CH_4 and CO_2 are shown in Fig. 3.10. The exit product mole fractions are shown in Fig. 3.11. The H_2 to CO ratio at 700 °C is ~ 2.72 and CO_2 conversion is lower compared to 800 °C, which can be attributed to the shifting of the thermodynamic equilibrium of the reactions involved.

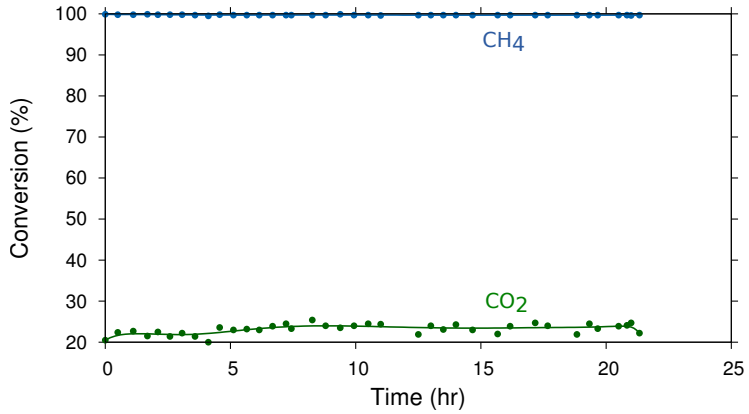

Figure 3.8: Time on stream conversion of CH_4 and CO_2 during catalyst stability test at 800 °C.

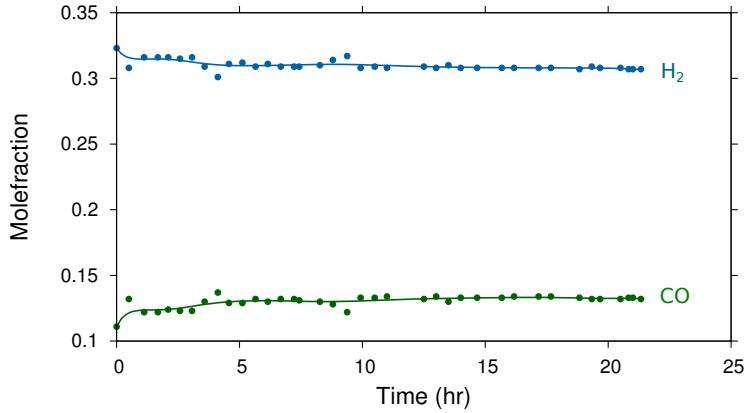

Figure 3.9: Time on stream mole fraction of H_2 and CO during catalyst stability test at 800 °C.

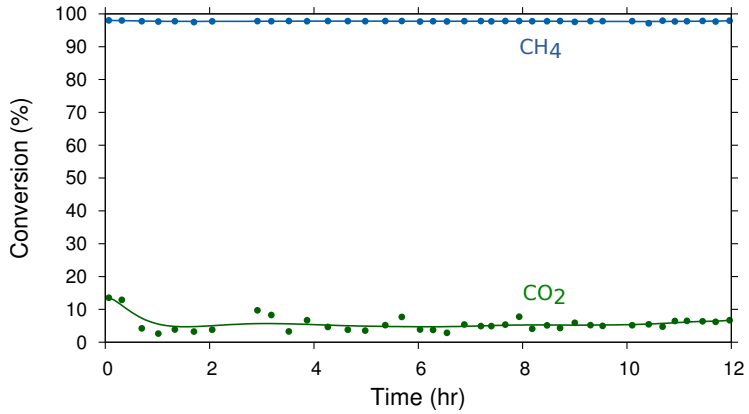

Figure 3.10: Time on stream conversion of CH_4 and CO_2 during catalyst stability test at 700 °C.

H

Table 3.6: Comparison between equilibrium prediction and experiments

Reactants/Products	Equilibrium		Experiments	
	800 °C	700 °C	800 °C	700 °C
CH_4 Conversion (%)	99.86	98.08	99.7	97.75
CO_2 Conversion (%)	22.85	7.03	23.2	5.6
H_2 dry moles fraction (%)	32.23	32.6	31.0	31.0
CO dry moles fraction (%)	13.06	11.5	13.0	11.3

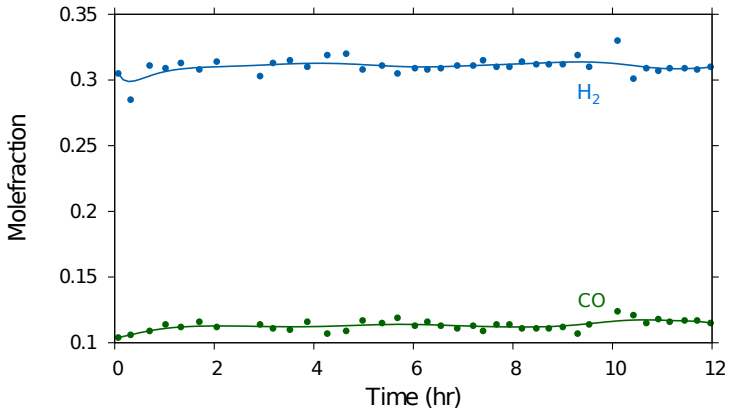

Figure 3.11: Time on stream mole fraction of H_2 and CO during catalyst stability test at 700 °C.

Equilibrium calculations are performed with DETCHEM^{EQUIL} [99] and Table 3.6 shows a comparison between equilibrium predictions and the experimental data. It can be seen that the conversions and product mole fractions agree well with the equilibrium calculations. The increase in CO_2 conversion with temperature shows that the methane dry reforming reaction takes place. At higher temperatures (800 °C), this endothermic reaction is favored and therefore CO_2 is consumed. Since all the catalysts used in the experiments are prepared in the same batch and since they are stable under non-poisoning gas atmosphere, we can assert that the catalyst deactivation by introducing H_2S to the feed gas is purely due to sulfur poisoning, at least for the time on stream considered in this study.

Mass balances of carbon and hydrogen are carried out for stability test at 800 °C based on equations of Eqs. 3.15 and 3.16.

Table 3.7: Carbon moles balance.

Species	In (mol/hr)	Out (mol/hr)
CH_4	0.05938	172.2 x 10^6
CO_2	0.03991	0.03066
CO	0.0	0.0663931
Total	0.09930	0.09723

3.9.2 Deactivation studies

Catalyst deactivation experiments are performed for two different temperatures and three different H_2S concentrations. Fig. 3.12 shows the deactivation of the catalyst for 20, 50, and 100 ppm H_2S with respect to

Table 3.8: Hydrogen moles balance.

Species	In (mol/hr)	Out (mol/hr)
2 x CH_4	0.11877	0.00034
H_2O	0.11978	0.07252
H_2	0.0	0.15859
Total	0.23855	0.23646

CH_4 +CO_2 concentration at 700 °C. All H_2S concentrations led to almost complete deactivation (98%) of the catalyst, however, the rate at which deactivation occur varies. Higher H_2S concentrations lead to faster deactivation.

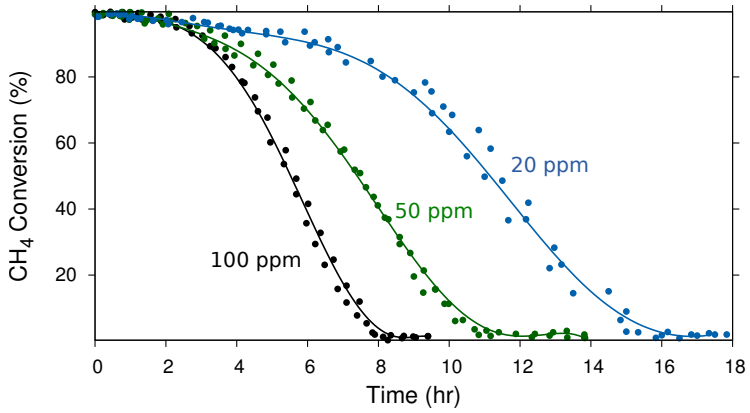

Figure 3.12: CH_4 conversion at 700 °C as a function of time for three different H_2S concentrations.

Figure 3.13 shows drop in CH_4 conversion as a result of deactivation at 800 °C for different H_2S concentrations. In all cases the catalyst activity dropped, however, did not deactivate fully. The residual activity retained by the catalyst depends on the concentration of H_2S in the feed gas. 100 ppm H_2S concentration in the feed gas led to a final steady state of 34% CH_4 conversion, 50 ppm to 43%, and 20 ppm to 48%.

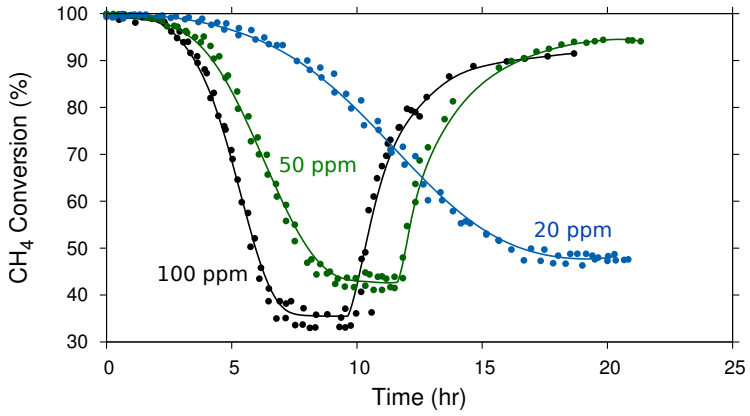

Figure 3.13: CH_4 conversion at 800 °C as a function of time for three different H_2S concentrations.

Deactivation versus time on stream for 20, 50, and 100 ppm for the two temperatures studied are shown

respectively in Fig. 3.14, 3.15, 3.16. It is interesting to notice that for both the temperatures the rate of activity loss (the slope of the curve) before reaching steady state is same for 50 and 100 ppm whereas for 20 ppm the rate of deactivation is much slower at 800 °C compared to 700 °C. For both the temperatures CH_4 conversion is ~98-99% in the absence of H_2S in the feed gas. Therefore, the catalyst deactivation is purely due to sulfur poisoning.

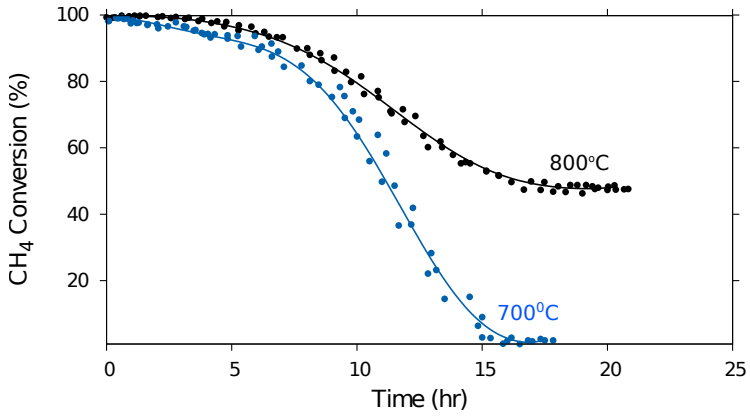

Figure 3.14: Comparison between CH_4 conversions achieved at 700 and 800 °C for 20 ppm H_2S in the feed gas.

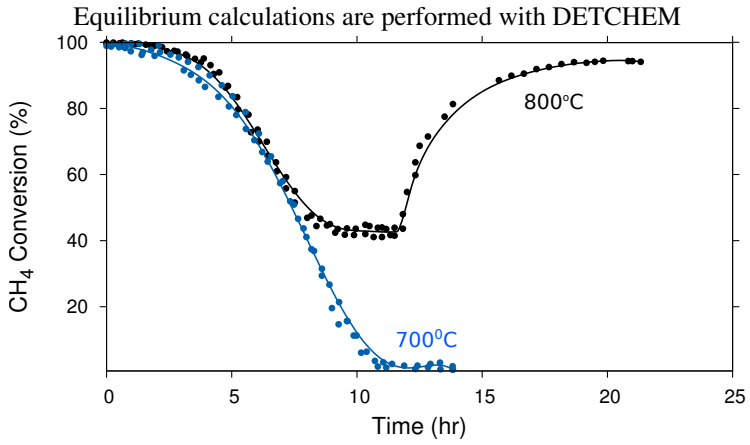

Figure 3.15: Comparison between CH_4 conversions achieved at 700 and 800 °C for 50 ppm H_2 S in the feed gas.

The H_2 and CO mole fractions from the reactor exit at 700 °C during deactivation for different H_2S concentrations are shown in Figures 3.17, 3.18. Examining Figure 3.12 and Fig. 3.17, 3.18 leads us to the conclusion that the final activity of the catalyst is independent of the H_2S concentration. In all cases the catalyst retained ~2% of its activity. However, the same is not true for high temperature operation.

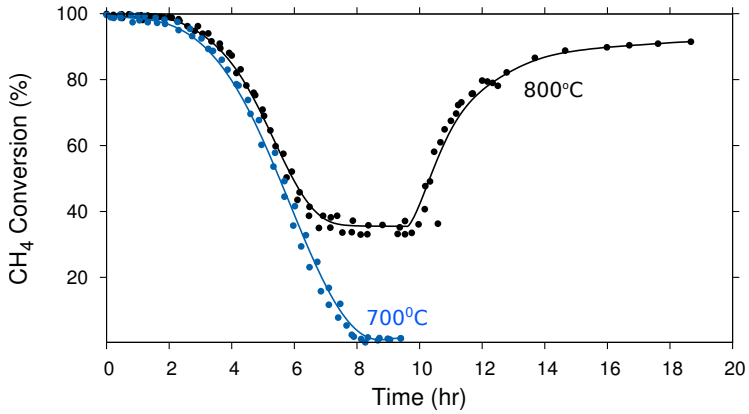

Figure 3.16: Comparison between CH_4 conversions achieved at 700 and 800 °C for 100 ppm H_2S in the feed gas.

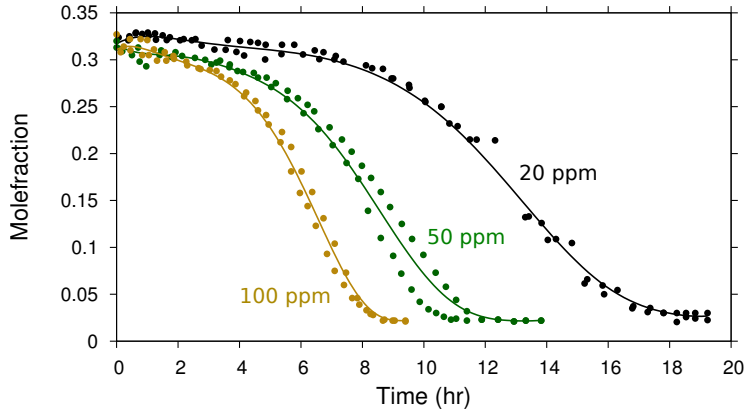

Figure 3.17: H_2 mole fraction from the reactor exit at 700 °C.

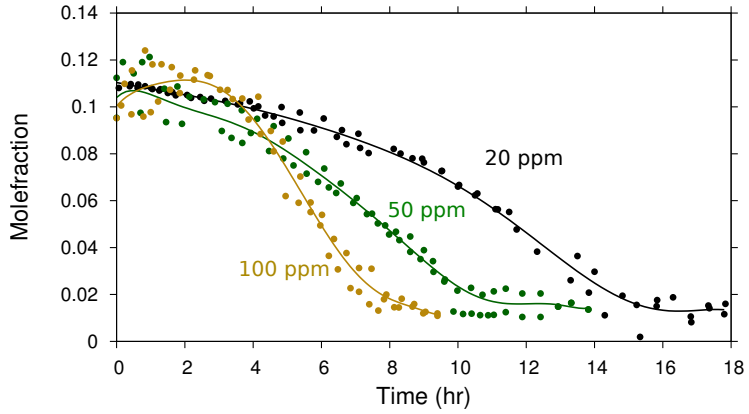

Figure 3.18: CO mole fraction from the reactor exit at 700 °C.

Figures 3.19 and Fig. 3.20 shows the exit mole fractions of H_2 and CO at 800 °C. Higher ppm level of H_2S results in low CH_4 conversion and hence low H_2 mole fraction in the product stream. That is at low operating temperatures, the saturation coverage of sulfur on Ni is independent of H_2S concentration. All the H_2S concentrations considered in this study lead to saturation coverages at 700 °C whereas at high temperature,

the mechanistics of H_2S adsorption and recombination reaction involving sulfur leads to different saturation coverages of sulfur for different H_2S concentrations.

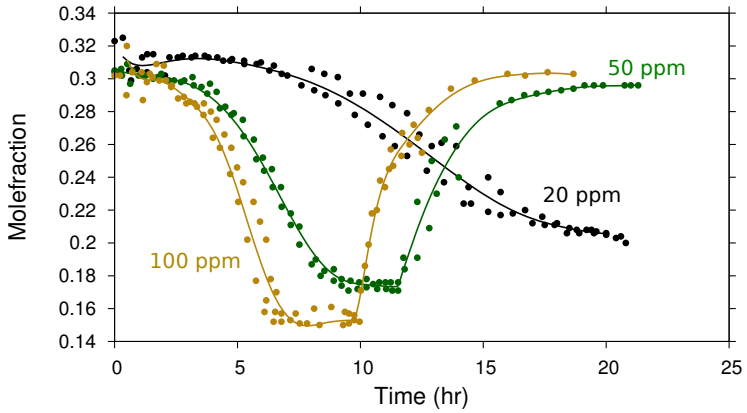

Figure 3.19: H_2 mole fraction from the reactor exit at 800 °C.

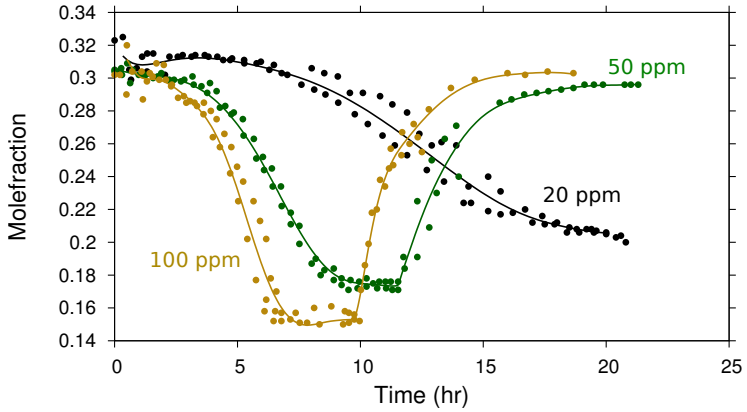

Figure 3.20: CO mole fraction from the reactor exit at 800 °C.

3.9.3 Regeneration by H_2S removal

Since chemisorption is a reversible process, surface adsorbed sulfur can be removed by decreasing the sulfur content in the feed stream [100]. For 100 and 50 ppm we have performed the regeneration experiments by removing H_2S from the feed gas after reaching their steady state residual activity. For both 100 and 50 ppm the catalyst activity again reached another steady state after H_2S removal (Fig. 3.12). However, full regeneration could not be achieved. In the case of 50 ppm 95% activity could be recovered, whereas for 100 ppm recovery is only 90%. The time required for regeneration is ~10 h, which is very short compared to the time required for conventional regeneration methods reported by Li et. al [1]. We could not perform regeneration experiments for 20 ppm due to periodic power outages after every 24 h. The rate of regeneration is same as rate of deactivation in all cases. For instance from Fig. 3.13 the deactivation for 100 ppm H_2S takes about 8 h and the regeneration also takes approximately the same duration. These results are consistent with the report of Ashra et al., [23]. The catalyst activity loss is mainly due to dissociative adsorption of H_2S on Ni leading

to the active sites being covered with sulfur. At high temperature each sulfur atom occupies one adsorption site on Ni [80]. To recover the activity the adsorbed sulfur needs to be removed from the active sites of the catalyst. The surface adsorbed sulfur can participate in recombination reactions with a number of other surface adsorbed species such as H, O, and OH. The recombination products can then desorb from the surface, leaving the surface again capable of promoting surface reactions. The partial recovery of activity would then imply that the adsorbed sulfur is not fully removed by the recombination reactions. Some possible reaction mechanisms for recombination reactions are given below.

$$S* + H* \rightleftharpoons SH* + * \tag{3.20}$$

$$SH* + H* \rightleftharpoons H_2S* + * \tag{3.21}$$

$$S* + O* \rightleftharpoons SO* + * \tag{3.22}$$

$$SO* + O* \rightleftharpoons SO_2* + * \tag{3.23}$$

3.9.4 Regeneration by temperature enhancement

At 800 °C the catalyst activity is recovered by removing H_2S from the feed gas. However, at 700 °C the catalyst activity could not be recovered in the same manner. This means that the kinetics of desorption and/or recombination reactions are not favored at low temperatures. This is further confirmed by temperature stepping at 700 °C which lead to recover the activity. Fig. 3.21 shows the gain in catalytic activity when the temperature is increased from 700 to 800 °C. 100 ppm H_2S concentration at 700 °C leads to almost complete deactivation of the catalyst. However, when the temperature is increased to 800 °C, the catalyst started regaining activity and stabilized at 32% CH_4 conversion, very close to the steady state activity at 800 °C for 100 ppm reported in Fig. 3.13. This also reconfirms the reproducibility of our experiments. Since chemisorption is exothermic an improved sulfur removal is naturally expected by increasing the temperature [100]. Higher temperature favors the kinetics for desorption reactions and recombination reactions involving adsorbed sulfur species. After reaching the steady state, H_2S is completely removed from the feed gas and the catalyst is allowed to regain its activity further. 92% of the activity is recovered by this process. This again corresponds very well with the final activity reported in Fig. 3.13 for 100 ppm case.

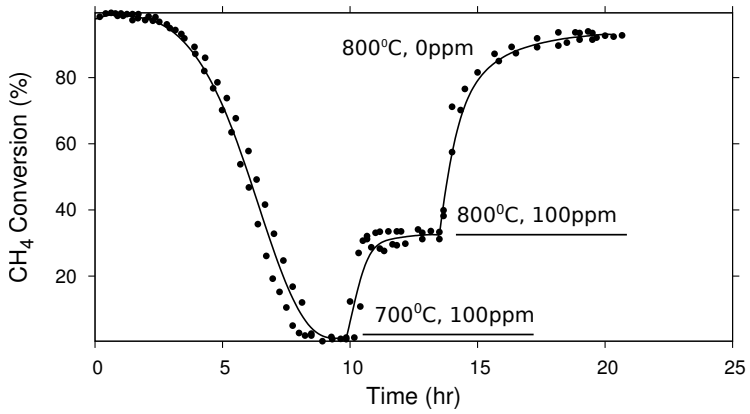

Figure 3.21: Effect of temperature and H_2S concentration on regaining catalyst activity.

The mole fractions of various gases from the reactor exit for the same case are shown in Fig. 3.22. At steady state before introducing H_2S into the reactor, CH_4 is fully converted and the reactor exit contains 33% H_2, 9% CO, 9% CO_2 and remaining N_2 . As soon as H_2S is introduced to the reactor, the reactants mole fraction starts to (CH_4 and CO_2) increases and stabilized respectively at 15% and 10%. These values corresponds very well to dry inlet mole fraction of CH_4 (16.7%) and CO_2 (11.2%). The 3% H_2 and 1.5% CO at the reactor exit is due to the residual activity (2%) of the catalyst.

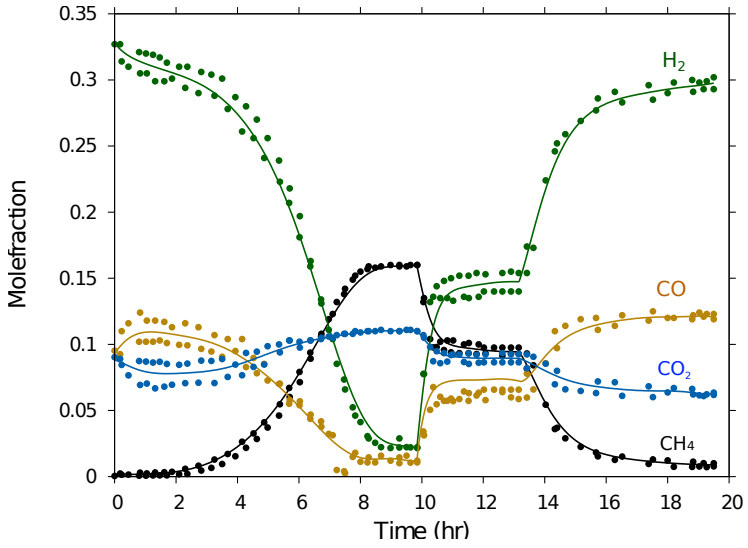

Figure 3.22: Mole fraction of various gases out of the reactor during the activity regeneration by temperature enhancement .

3.9.5 Regeneration by steam treatment

Conventionally, the sulfur poisoned Ni is regenerated by sequential steam, steam air, and steam hydrogen treatment. Since the removal of adsorbed sulfur can be easily achieved by steaming above 650 °C we have attempted the regeneration by treating with H_2O. Once the catalyst is fully deactivated at 700 °C, the feed stream is replaced with H_2O (0.036 ml min^{-1}) diluted in N_2 (102.4 ml min^{-1}) flow for ~5 h. Since steam treatment leads to the formation of NiO the catalyst is further reduced under H_2 flow (20 ml min^{-1}) at 700 °C for 5 h. Total regeneration time is 10 h, which is far shorter than the regeneration time reported by Li et al. and Nielsen [24, 100]. The regenerated catalyst is tested for its activity by performing reforming reaction without H_2S in the feed stream. CH_4 conversion after regeneration is shown in Fig. 3.23. The catalyst showed stable operation for more than 10 h whereas Li et al. observed fall in activity of the catalyst regenerated using conventional sequential technique after 10 h of operation. Its very likely that the steam treatment regenerates the catalyst by forming SO_2 according to reactions 3.22 and 3.23. The oxygen atoms are formed by the dissociative adsorption of H_2O on Ni surface.

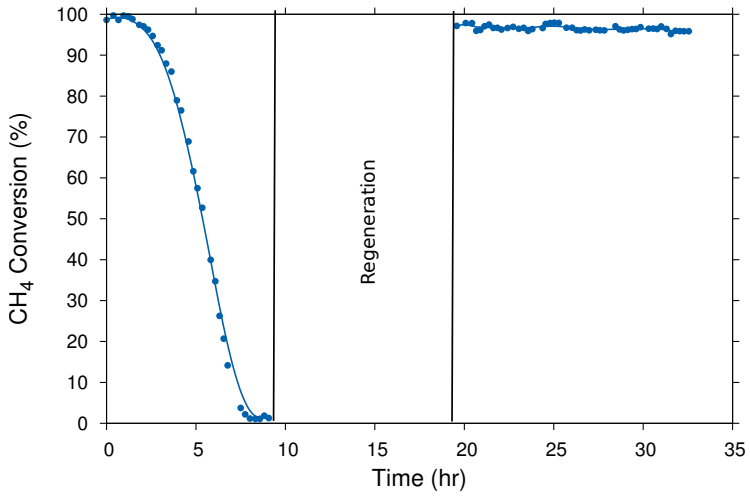

Figure 3.23: Regeneration of poisoned catalyst at 700 °C by steam treatment.

3.10 Conclusions

Ni Catalyst poisoning due to H_2S during the reforming of biogas is studied. The experiments are performed at 700 and 800 °C and for three diferent H_2S concentrations (20, 50, and 100 ppm w.r.t CH_4 +CO_2 concentration). At 700 °C, the saturation sulfur coverage is independent of H_2S concentration in the feed gas. However, at 800 °C, the saturation coverage of sulfur is dependent on the concentration of H_2S. Generally, higher H_2S concentrations lead to faster deactivation of the catalyst. The deactivation and regeneration showed exponential behavior on time on stream. At higher H_2S concentrations (50 and 100 ppm), the rate of deactivation is found to be independent of the temperature. At 800 °C, the activity of the catalyst is partially recovered just by removing H_2S from the feed gas. However, this method did not recover the catalyst activity at 700 °C. Regeneration of the poisoned catalyst at 700 °C required either temperature enhancement or steam treatment. The activity of the catalyst which is almost completely poisoned by exposure to 100 ppm H_2S at 700 °C is regenerated partially by enhancing the temperature to 800 °C and the catalyst is almost completely regenerated by removing H_2S from the feed gas. The same catalyst may also be regenerated by steam treatment. Five hours of steam treatment followed by reduction in H_2 for 5 h led to almost complete recovery of the catalyst activity. This regeneration time is far shorter than the ones reported in previous literature.

Chapter 4

Heterogeneous Catalysis

In heterogeneous catalysis, the reactants and the catalyst are in different phases, usually the catalyst is a solid and the reactants are either gases or liquids. These reactions proceed at the interface between the solid catalyst surface and the adjacent gas phase. The catalyst provides an alternate reaction pathway between reactants and products by lowering the activation energy for the reaction as shown in Fig. 4.1. Heterogeneous catalysis is of paramount importance in many areas of the chemical and energy industries.

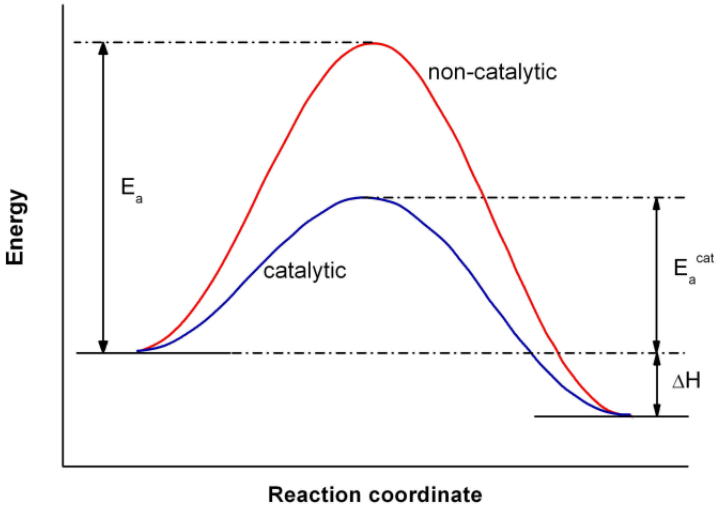

Figure 4.1: Activation energy for catalytic and non-catalytic pathway for a chemical reaction [101].

The reaction conditions for a specific reaction is defined by the thermodynamics of the system. The catalyst facilitates the adsorption of the reactants and their subsequent conversion into products. However, the products of heterogeneous catalyst reaction must be removed rapidly from the catalyst surface to generate free active sites. In general heterogeneous catalysis consists of various physico-chemical processes such as [102]:

- Chemisorption

- Dissociation/activation
- Diffusion
- Recombination
- Desorption

After diffusion from the gas-phase to the catalyst surface, the reactants adsord on the surface, and the adsorbed species further undergoes dissociation, disproportionation, and recombination. The reaction rates of surface reaction and desorption depend on the surface coverage and reaction temperature. Moreover, the catalytic reaction rate is specific to the catalyst formulation, catalyst support, catalyst type, and method of catalyst manufacturing. Therefore, the description of heterogeneous reaction rates is more complex compared to gas-phase kinetics. Due to this complexicity, global rate expressions and reaction rates used to be the model for heterogenerous reactions. The reaction rate has often been based on catalyst mass, catalyst volume, reactor volume, or catalyst external surface area.

Most of the global reaction kinetics are developed based on some assumptions, and the validity of these assumptions cannot be verified a priori by changing the operating conditions. Most frequently Langmuir-Hinshelwood-Hougen-Watson (LHHW) method is used to develop the rate expressions for heterogeneous systems, which is based on Langmuir adsorption. Furthermore, rate expressions are developed by assuming that both reactants and products are equilibrated with surface species and that rate controlling step can be identified. LHHW kinetics cannot account for the complex variety of phenomena mentioned above and that the rate parameters must be evaluated experimentally for each new catalyst and various external conditions. The advantage of micro-kinetic model is that there are no initial assumptions during the mechanism development like rate determining step (RDS), most abundant reaction intermediate (MARI), quasi steady state (QSS) and partial equilibrium. A key advantage of the micro-kinetic analysis is that it captures system features under significantly different conditions.

4.1 Mean-field approximation

Heterogeneous reactions on solid surfaces can be principally treated by drawing analogy with gas phase reactions if mean-field approximation is applied. In mean-field approximation, the surface adsorbed species are assumed to be randomly distributed on surface, which is viewed as being uniform. The state of the surface is described by the temperature T and the fractional coverages of adsorbates θ_{k}. Fractional coverage θ_{k} is the fraction of the surface covered by the surface adsorbed species k. Moreover, it is assumed that the adsorption is limited to a mono atomic layer, and an uncovered surface is treated as the k_s'th surface species. This means, there are only $K_s - 1$ surface adsorbed species. The surface temperature and coverage depend on time and the macroscopic position in the reactor, but are averaged over microscopic local fluctuations. Under these assumptions a chemical reaction can be defined in a way similar to gas-phase reactions [103],

$$\sum_{k=1}^{K_g+K_s+K_b} \nu'_{ki} X_k \Longrightarrow \sum_{k=1}^{K_g+K_s+K_b} \nu''_{ki} X_k \tag{4.1}$$

where X_k is the species involved in the reaction and ν'_{ki} and ν''_{ki} are the stoichiometric coefficients of the k'th species for the i'th reaction.

Steric effects of adsorbed species and various configurations are taken into account in the surface structure. The surface structure is accociated with surface site density Γ in mol/m^2 that describes the maximum number of species that can adsorb on a unit surface area [104]. The number of sites required for the species to adsorb on the surface is given by the coordination number σ_k. In the following analysis it is assumed that the total number of surface sites is conserved for each reaction, i.e,

$$\sum_{i=1}^{K_s} \nu_{ki}\sigma_k = 0 \tag{4.2}$$

The above equation means that if the reactants occupy two surface cites then the products should also occupy two surface sites. Here $\nu_{ki} = \nu''_{ki} - \nu'_{ki}$. However, the scenario could be different in case of Chemical Vapor Deposition processes (CVD), where the surface sites are not conserved.

Under these assumptions a multistep reaction mechanism can be developed. The net molar production rate $\dot{s}_k$ of a gas phase species or a surface adsorbed species due to heterogeneous reactions on the solid surface is given by

$$\dot{s}_k = \sum_{i=1}^{N} \nu_{ki} k_{fi} \prod_{k=1}^{K_g+K_s+K_b} [X_k]^{\nu'_{ki}} \tag{4.3}$$

where N is the number of surface reactions, $[X_k]$ are the species concentrations, which are given in mol/m^2 for the K_s adsorbed species, and mol/m^3 for the K_g and K_b gaseous and bulk species. A modified Arrhenius expression is used for the reaction rate constant based on mean field approximation and is given by

$$k_{f_i} = A_i \left(\frac{T}{T^0}\right)^{\beta_i} \exp\left(-\frac{E_{ai}}{RT}\right) \prod_{k=K_g+1}^{K_g+K_s} \theta_k^{\mu_{ki}} \exp\left(-\frac{\varepsilon_{ki}\theta_k}{RT}\right) \tag{4.4}$$

where, k_{fi} is the forward rate constant for the i'th reaction, μ_{ki} and ε_{ki} are the parameters modeling the surface coverage dependancy of rate constant for i'th reaction and the θ_k is the surface coverage of the k'th chemical species. The rate constant for the reverse reaction can be calculated from the thermodynamic data as

$$K_{c_i} = \frac{k_{f_i}}{k_{r_i}} = K_{p_i} \left(\frac{p^0}{RT}\right)^{\sum_{k=1}^{K_g} \nu_{ki}} \prod_{k=K_g+1}^{K_g+K_s} \frac{\sigma_k^{\nu'_{ki}}}{\sigma_k^{\nu''_{ki}}} \tag{4.5}$$

where p^0 is the standard state pressure and K_{p_i} is the equilibrium constant calculated by

$$K_{p_i} = \exp\left(\frac{\Delta S_i^0}{R} - \frac{\Delta H_i^0}{RT}\right) \tag{4.6}$$

The relationship between surface coverages and the surface concentrations are given by

$$\theta_{\mathrm{k}} = \frac{[X_k]\sigma_k}{\Gamma} \tag{4.7}$$

and the temporal variations of surface coverages are given by

$$\frac{d\theta_{\mathrm{k}}}{dt} = \frac{\dot{s}_k \sigma_k}{\Gamma}, \quad k = K_g + 1, \ldots, K_g + K_s, \tag{4.8}$$

Here Γ is the available site density in mol/m^2 and σ_k is coordination number i.e., the number of sites the species takes to adsorb. At steady state the above equation becomes

$$\dot{s}_k = 0, \quad k = K_g + 1, \ldots, K_g + K_s, \tag{4.9}$$

for surface adsorbed species indicating that the surface composition is invariant in time (although varying spatially). Since the surface coverages are referred to a single mono-layer, the sum of coverages obeys the condition

$$\sum_{k=1}^{K_s} \theta_{\mathrm{k}} = 1. \tag{4.10}$$

Since the reactor temperature and concentrations of the gases vary along the axial position in the reactor, and surface coverages vary with position, the lateral interactions of surface species are neglected in the above model. This assumption is valid due to the fact that the computational cells used in reactor simulations are much larger than the range of lateral interactions of the surface processes. The detailed implementation of kinetics is published elsewhere [105, 106, 107].

The change of entropy ΔS_i^0 and enthalpy ΔH_i^0 for *i*'is given by

$$\frac{\Delta S_i^0}{R} = \sum_{k=1}^{k=K_g+K_s} \nu_{ki} \frac{S_k^0}{R} \tag{4.11}$$

and

$$\frac{\Delta H_i^0}{RT} = \sum_{k=1}^{k=K_g+K_s} \nu_{ki} \frac{H_k^0}{RT} \tag{4.12}$$

4.2 Adsorption and sticking coefficients

Heterogeneous reactions occur by collision of gas phase molecule on a catalytically active solid adsorbent. According to kinetic theory of gases the rate Z at which these collisions occur is given by

$$Z = \sqrt{\frac{k_B T}{2\pi W}} \left(\frac{N}{V}\right), \tag{4.13}$$

where k_B is Boltzmann's constant, T is the absolute temperature, W the molar mass, and N/V is the number density of gas molecules. The kinetic gas theory expression assumes that the gas molecules are in continuous random motion, with a Maxwellian velocity distribution that is determined by the temperature [104]. However, these surface collisions are only one of the several processes that occur during surface reactions. For example the surface adsorbate can be mobile, there can be interactions between the surface adsorbates, dissociative adsorption, and desorption from the surface and so forth. However, for a simple sticking reaction, the reaction rate is just the rate of collision multiplied with the probability that the collision results in the formation of a surface adsorbate. The probability of such a process, or in other words the ratio of the rate of adsorption to the rate at which the adsorptive strikes the total surface can be expressed in terms of sticking coefficient S_i^0. Furthermore, the sticking coefficient in general depends on temperature and the temperature dependency is expressed as [101]

$$S_k^0 = S_i^0 = a_k \left[\frac{T}{T^0}\right]^{b_k} e^{-c_i/RT} \tag{4.14}$$

Since sticking coefficient is a probability factor, its value should lie between 0 and 1. a_k and b_k are dimensionless constants and c_k has units compatible with gas constant R. The expression for reaction rate while using sticking coefficient can be written as

$$\dot{s}_k = S_k^0 \sqrt{\frac{RT}{2\pi W}} [X_k] \theta_{\text{free}}^{\tau} \tag{4.15}$$

Here θ_{free} is the available free surface coverage for collision $\tau = \sum_k^{K_s} \nu'_{ki}$. Equation 4.15 can be written as

$$\dot{s}_k = k_{f_i} [X_k] [X_{\text{free}}]^{\tau} \tag{4.16}$$

where

$$k_{f_i} = \frac{S_i^0}{\Gamma^{\tau}} \sqrt{\frac{RT}{2\pi W}} \tag{4.17}$$

4.3 Development of multistep surface reaction mechanism

Development of heterogeneous reaction mechanisms is a complex process and the inputs come from various sources. A schematic of the same shown in Fig. 4.2. Initialy a tentative mechanism is proposed based on the surface studies, analogy to gas phase kinetics, and organo metallic compounds. This mechanism contains all posiible paths for the formation of chemical species, which are in the form of elementary kinetics [103]. Generally surface science techniques are used to study the surface properties of a single crystal

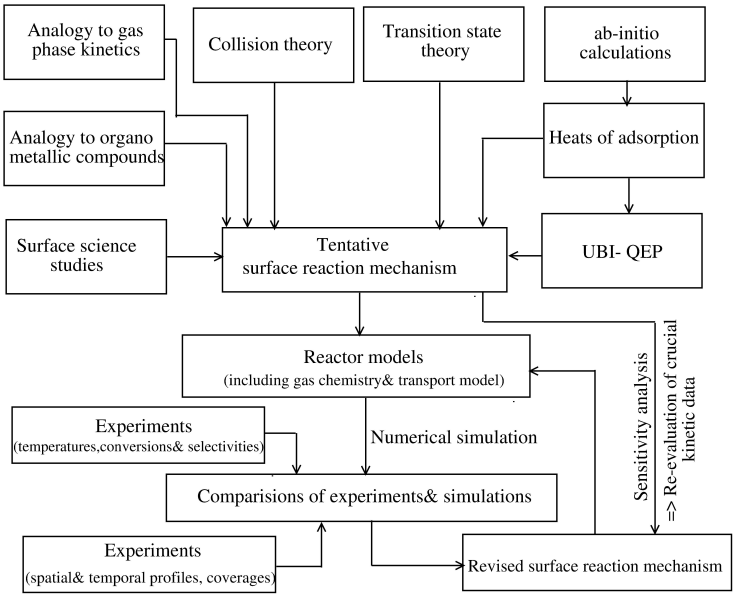

Figure 4.2: Methodology of the development of a surface reaction mechanism [103].

surface. The experimental techniques such as AES, XPS, LEED, and some direct probe methods are used to

get information on elemental, chemical, or structural composition/ properties of the catalytic surface. Temperature programmed desorption/reaction/reduction techniques gives information on surface reaction kinetics and mechanisms. Sophisticated modulated molecular beam-scattering techniques are conducted at very low pressures for surface science studies. Since most of these techniques uses ultra high vacuum, extrapolation of these results to higher pressures may be questionable. For example, CO can dissociate on platinum at high pressure and temperature, while this reaction path way could not be observed in UHV experiments [108]. In-situ measurements are required for surface reaction investigations at technically feasible pressures and temperatures on catalyst surfaces

In mechanism development, rate expressions have to be developed for the proposed mechanism. A range of theoretical techniques such as *ab-initio* electronic structure calculations and semi-empirical approximations, transition state theory, quantum mechanical reactive scattering, and classical trajectory methods are used in the mechanism development. The developed mechanism should be thermodynamically consistent in enthalpy as well as in entropy. The consistency of the surface mechanisms will be discussed in chapter 5.

Kinetic data of common facets such as (111), (110), (100) are used as initial guesses for real catalysts, especially for the estimation of sticking coefficients for the adsorption steps, and desorption energies. Density functional theory (DFT), or experiments (microcalorimetry) has to be used to determine heats of chemisorption for all the species that are presumed to be present on the surface. Using this information as an input, UBI-QEP makes possible the computation of thermodynamically consistent, coverage-dependent activation energies for all the proposed reactions, through analytical equations. The calculations of activation energies for the surface reactions by using UBI-QEP will be discussed more in detail in chapter 5.

Based on the available theories, a tentative reaction mechanism is initially proposed. The tentative reaction mechanism is then coupled with reactor models that may include appropriate gas-phase kinetics and transport phenomena. These models are to be simulated with actual experimental conditions of numerous experiments. The numerical data need to be compared with experimental data such as conversions, selectivities, etc. The deviations between experimentally derived and numerically predicted data can now be used for fine tuning the mechanism, which even can be done using optimization techniques [109]. Sensitivity analysis is a widely used technique to fine tune elementary reaction mechanisms [110, 105]. Sensitivity analysis allows for an identification of the individual reaction steps that are most influential to the system. Several methods can be used in order to calculate the sensitivity of the solution, i.e., the time behavior of the different species profiles with respect to the rate coefficients. Generally sensitivity analysis involves perturbation of pre-expotentials from their nominal, initial value, and estimation of the corresponding change in the model response. Although this technique is very simple, it has the disadvantage of requiring a large amount of computational power if the number of parameters involved are large. Furthermore, appropriate reactor models need to be used and experimental uncertainties have to be taken into consideration.

Chapter 5

Kinetic modeling

5.1 UBI-QEP

The theoretical approaches to surface reactivity are based on the estimation of energitics (enthalpies and activation barriers). Determination of adsorption energies and activation barriers of surface reactions is a complex task. The reaction energetics are determined by using quantum mechanical methods such as *ab-initio* wave function methods and density functional calculations [111]. These methods are useful for structural predictions such as calculations of bond lengths and angles, vibrational frequencies, charge moments, etc. than for thermochemical properties due to their computational demands. As a result accurate calculations of bond energies and activation barriers for surface reactions are still an enormous challenge [112].

The simulation of adsorption and surface reaction on a metal surface is commonly accomplished by modeling the catalyst surface as a finite cluster of limited size. A fundamental dilemma, with both DFT and *ab initio*, is designing or assembling the cluster of a size such that it accurately represents the atoms on the bulk surface. It is a theoretical paradox: the clusters must be large enough to adequately represent a geometric and electronic structure of a surface; yet, the size of the cluster must also be small enough that it may be accurately treated by the available methods [112].

A reasonable agreement between the cluster and slab-type calculations, with experiments are achieved by using *ad hoc* parameters [112]. However, the use of *ad hoc* parameter values blurs the conceptual picture. Because of the challenge with both first-principle and semi-empirical methods, another practical alternative is considered: the phenomenological approach. The phenomenological approach differs from empirical- or heuristic-based approaches because it employs phenomenological quantities, i.e., observable thermodynamic quantities, as input parameters and analytically calculates quantities relevant to phenomenological, observable thermodynamic properties of surface adsorption and reactive systems. The greatest advantage of an analytic phenomenological model is that it provides a direct conceptual understanding through its explicit interrelations among its parameters. Because our interest is with surface energetics, the model should be based on thermodynamics. An informative analytic model should have a rigorous and rigid mathematical formalism which provides well-defined rules [112].

Bond Order Conservation− Morse Potential (BOC− MP) method was developed by Shustorovich. Fur-

ther developments resulted in the renaming of the method, now known as the Unity Bond Index−Quadratic Exponential Potential (UBI−QEP) method. This method is unique due to its success with complex reactions, whose mechanisms may be extensive both in terms of number of intermediates and number of elementary reactions. This method requires only a few basic inputs such as atomic heats of adsorption and gas phase molecular bond energies to calculate heats of chemisorption of diatomic, polyatomic molecules, as well as the reaction activation barriers of dissociation, recombination, and disproportionation reactions. Typically, the accuracy of the calculated values of heats of adsorption and activation barriers is within 1-3 kcal/mol. This method has been successfully applied to several reaction systems including direct conversion of methane to methanol [113], methanol synthesis [114], hydrogen peroxide synthesis [115], ammonia synthesis [116], NO reduction and decomposition [117], and Fischer-Tropsch synthesis [118, 119], sulfur oxide chemistry [120], and many more.

BOC− MP was initially based on three postulates, the modified UBI-QEP method is now based on four main postulates. First, the two body interction energy is spherical and depends only on the interbody distance r. Second, the-two body interaction energy poses a single minimum and approaches zero monotonically as the distance between them increases and is described by Morse potential (MP) as

$$E(x(r)) = a(x^2(r) - 2x(r)). \tag{5.1}$$

Third, as shown above, the two-body interaction is expressed as a polynomial function of an exponential variable called the bond index and can be written as

$$x(r) = \exp\left[\frac{-(r - r_0)}{b}\right], \tag{5.2}$$

where r is the distance of the bond of interest, a is the bond energy, r_0 is the equilibrium distance corresponding to the minimum interaction energy, and b is a distance scaling constant. In a many body system, the total bond order, X, of all interacting two-center bonds is conserved at unity

$$X = \sum_i x_i = 1. \tag{5.3}$$

Fourth, the multi-body, where body is defined as an atom or group of atoms that may be treated as a single entity, potential energy is formed by summing the nearest neighbor pair-wise interactions [111], i.e.,

$$E(X) = \sum_i a_i \left[x_i^2 - 2x_i\right] \tag{5.4}$$

The bond index function should be defined such that: a one-to-one correspondence between $x(r)$ and r exists; $x(r)$ is non-negative and greater than zero; $x(r)$ monotomically decreases to zero as r increases without bound; and, at the equilibrium distances, $x_0 = x(r_0) = 1$.

The unity bond index (UBI) condition at equilibrium requires that, at the equilibrium distance, r_0, any bond index will be unity, regardless of the system. In addition, the total bond index (N) of a multi-body system is conserved, stipulating that $N = \mathrm{x}_0$. Bond indices are the same regardless of changing multiplicities

of states, therefore N may be considered a normalization constant where

$$N = \sum_i x_i(r_i) \tag{5.5}$$

The value of the equilibrium bond index is the value to which the bond index is conserved [111]. As a result, the unity bond index condition may be written as

$$X = \sum_i x_i(r_i) = N = 1. \tag{5.6}$$

$N = 1$ condition has been verified by *ab initio* calculations with exponential bond index functions for linear, three-center bonds. This condition is verified for adsorption and dissociation of diatomic molecules H_2, O_2, and F_2 on closed packed metal (Hg) surface (111).

Therefore, the UBI-QEP principle of chemisorption states "The sum of the two-body bond indices of the active bonds along any minimum energy path of a metal surface reaction is conserved and equal to unity" [111].

The total energy of a many-body system can be expressed as a summation of additive two-body bond energies governed by the UBI condition. For example, UBI constraint for a diatomic AB adsorption is written as

$$x_{\mathrm{AB}} + x_{\mathrm{A}} + x_{\mathrm{B}} = 1. \tag{5.7}$$

For practical reasons, the sum over pairwise interaction energies is limited to nearest neighbors within a metal surface unit mesh or bonding site. Within the UBI-QEP method, the heats of chemisorption (Q) and reaction activation barriers (E_{for} and E_{rev}) are independent of the choice of the bond index; they only contain energy parameters which are thermodynamic observables that are obtained from atomic chemisorption energies (Q_A) and gas-phase molecular bond energies (D_{AB}).

5.1.1 Atomic heats of adsorption

The heats of atomic chemisorption is determined from the energy function E which is the sum of the n pairwise interactions between the adatom, and the n metal atoms of the surface (M), that form the M_n binding site or unit mesh

$$E = Q_0 \sum_i^n \left[x_i^2(r_i) - 2x_i(r_i) \right], \tag{5.8}$$

where Q_0 is the strength of the M-A interaction, independent of the crystal plane. The summation in the above equation is limited to the nearest neighbor metal atoms, or the number of metal atoms defining the binding site. For example n=1 for on-top, n=2 for bridge type, n=3 for fcc (111) hollow, n=4 for fcc (100) hollow, n=5 for bcc(100) hollow.

The atomic binding Eq. 5.8 is optimized under the unity bond index constraint Eq. 5.7, and the resulting

equation represents the binding energy of n M-A interactions

$$Q_{nA} = -E(n) = Q_{0A}\left(2 - \frac{1}{n}\right) \tag{5.9}$$

The value of Q_{0A} in the above equation can be found from the experimental heat of atomic chemisorption Q_A,

$$Q_{0A} = \frac{Q_A(n)}{(2 - 1/n)} \tag{5.10}$$

The heats of chemisorption for diatomic molecules are based on the type of binding. Weakly bound molecules such as closed shell molecules CO, N_2 or molecular radicals with strongly delocalized unpaired electrons such as O_2, NO tend to have heats of chemisorption in the range 10-35 kcal/mol. The heat of chemisorption for mono-coordination of weakly bound diatomics over a n-fold site is given by

$$Q_{\mathrm{AB},n} = \frac{Q_{0A}^2}{Q_{0A}/n + D_{\mathrm{AB}}}. \tag{5.11}$$

where D_{AB} is the gas phase dissociation energy of AB molecule. Eq. 5.11 gives higher values for higher coordination number than for on-top coordination. This may be due to neglecting the repulsive M-B interactions. Another reason for neglecting the M-B repulsive interactions may be because it is particularly inaccurate for mono-coordination of homonuclear diatomics. For mono-coordinated closed shell molecule with on-top binding, the chemisorption energy is given by

$$Q_{\mathrm{AB}} = \frac{Q_{0\mathrm{A}}^2}{(Q_{0\mathrm{A}+D_{\mathrm{AB}}})}. \tag{5.12}$$

The heat of energy for on-top site with di-coordination of diatomic molecule , AB is given by

$$Q_{\mathrm{AB}} = \frac{ab(a+b) + D_{\mathrm{AB}}(a-b)^2}{ab + D_{\mathrm{AB}}(a+b)}, \tag{5.13}$$

where

$$a = \frac{Q_{0\mathrm{A}}^2(Q_{0\mathrm{A}} + 2Q_{0\mathrm{B}})}{(Q_{0\mathrm{A}} + Q_{0\mathrm{B}})^2}, \tag{5.14}$$

and

$$b = \frac{Q_{0\mathrm{B}}^2(Q_{0\mathrm{B}} + 2Q_{0\mathrm{A}})}{(Q_{0\mathrm{A}} + Q_{0\mathrm{B}})^2}. \tag{5.15}$$

Eq. 5.13 for a homonuclear diatomics, A_2 can be written as

$$Q_{\mathrm{A}_2} = \frac{9Q_{0\mathrm{A}}^2}{(6Q_{0\mathrm{A}} + 16D_{\mathrm{A}_2})}. \tag{5.16}$$

The chemisorption for a AB molecule positioned parallel to a surface and across the M-M bridge is given by

$$Q_{\mathrm{AB}} = \frac{2[ab(a+b) + 2D_{AB}(a-b)^2]}{ab + 2D_{AB}(a+b)}, \tag{5.17}$$

where

$$a = 3Q_{0\mathrm{A}}/4, \tag{5.18}$$

and

$$b = 3Q_{0\mathrm{B}}/4. \tag{5.19}$$

For a homonuclear A_2 Eq. 5.17 reduces to

$$Q_{\mathrm{A}_2} = \frac{9Q_{0\mathrm{A}}^2}{(3Q_{0\mathrm{A}} + 16D_{\mathrm{A}_2})}. \tag{5.20}$$

Strong binding typically occurs with radicals that have localized unpaired electrons (i.e. OH, SH and CH). In this case, the heat of chemisorption is given by

$$Q_{\mathrm{AB},n} = \frac{Q_{\mathrm{A}}^2}{Q_{\mathrm{A}} + D_{\mathrm{AB}}}, \tag{5.21}$$

and the chemisorption energies of these molecules are in range of ~ 35-120 kcal/mol. The chemisorption energies of medium binding are in the range of ~ 10-120 kcl/mol and is given by

$$Q_{AB} = 0.5\left[\frac{Q_{0A}^2}{Q_{0A/n} + D_{AB}} + \frac{Q_A^2}{Q_A + D_{AB}}\right]. \tag{5.22}$$

Once the chemisorption energies are determined, the enthalpy change for each reaction, as it occurs on the surface, may be calculated as

$$\Delta H = \sum_r Q_r - \sum_p Q_p + \sum_b D_b - \sum_f D_f \tag{5.23}$$

where Q_r and Q_p are respectively chemisorption energies of reactants and products, D_b and D_f are the binding energies that are broken (b) and formed (f) respectively. The net enthalpy change of a reaction is written as the sum of the enthalpies of the steps of the thermodynamic cycle:

$$\text{adsorbed reactants} \rightarrow \text{gas-phase reactants} \quad \Delta H_1 = \sum_a Q_r$$

$$\text{gas-phase reactants} \rightarrow \text{gas-phase products} \quad \Delta H_2 = \sum_b D_b - \sum_f D_f$$

$$\text{gas-phase products} \rightarrow \text{adsorbed products} \quad \Delta H_3 = -\sum_c Q_p$$

The net entahpy change is $\Delta H_1 + \Delta H_2 + \Delta H_3$.

In the case of the disproportionation reaction, A(s) + BC(s) $\rightleftharpoons$ AB(s) + C(s), the direction of the reaction is defined such that the condition $D_{\mathrm{BC}} > D_{\mathrm{AB}}$ is satisfied. If it is not, the direction of the reaction should be reversed for the analysis [121].

5.1.2 Activation energy barriers

The activation energy (ΔE_{AB}^*) of the reaction in the forward direction (dissociation reaction), corresponding to the appropriate form of the reaction, may be written as

$$\Delta E_{\mathrm{AB}}^* = \frac{1}{2}\left[\Delta H + \frac{Q_{\mathrm{A}}Q_{\mathrm{B}}}{Q_{\mathrm{A}} + Q_{\mathrm{B}}}\right]. \tag{5.24}$$

The recombinations reaction is the reverse of dissociation reaction and therefore the activation barrier for recombination reaction ($\Delta E^*_{\mathrm{AB},rev}$) is written as

$$\Delta E^*_{\mathrm{AB,rev}} = \Delta E^*_{\mathrm{AB}} - \Delta H. \tag{5.25}$$

In the case where the numerical result for either the forward or reversed activation energy is negative, both activation energies are shifted such that the negative activation energy is forced to zero and the enthalpy change for the reaction remains unchanged [121].

The dissociation barrier relative to gas phase reactants is obtained from the difference between activation barrier relative to surface adsorbed reactants and the heat of adsorption of dissociating molecule (Q_{AB}):

$$\Delta E^g_{f,g} = \Delta E^*_{f,s} - Q_{\mathrm{AB}} \tag{5.26}$$

The reverse activation energy for this type of reaction may be determined from the following equations, depending on the sign of the forward activation barrier

$$\Delta E^*_{f,s} = \Delta E_{b,g} = Q_A + Q_B - D_{AB} + \Delta E^*_{f,g}, \qquad if\ \ \Delta E_{f,g} > 0 \tag{5.27}$$

or

$$\Delta E^*_{f,s} = \Delta E^*_{b,s} - \Delta E_{f,g} = Q_A + Q_B - D_{AB}, \qquad if\ \ \Delta E_{f,g} < 0 \tag{5.28}$$

where D_{AB} is defined as the difference between total bond energies of the reactants and products. This definition is valid for both atomic and molecular adsorbates [122]. Table 5.1 shows the heats of chemisorption and gas phase dissociation energies for species involved in biogas steam reforming

Table 5.1: Chemisorption energies (Q) and gas-phase dissociation energies (D) [123, 111, 124, 125, 121, 120].

Species	Q (kcal/mol)	D (kcal/mol)
CH_4	6	398
CH_3	48	293
CH_2	83	183
CH	116	81
C	171	–
CO	27	257
CO_2	6.35	384
HCO	50	274
O	115	–
H	63	–
OH	61	102
H_2O	17	220
H_2S	19	173
SH	65	82
S	112	–
SO	17	125
SO_2	36	132

As an example of the application of the UBI-QEP method, consider one of the reaction H_2S + Ni(s) $\rightleftharpoons$ SH(s) + S(s) on a Ni(111) catalyst. Where "(s)" represents the species on the surface. Using the information provided in Table 5.1, the enthalpy change of the elementary reaction step is calculated using Eq. 5.23

$$\Delta H = \sum_r Q_r - \sum_p Q_p + \sum_b D_b - \sum_f D_f$$

$$= Q_{\mathrm{H_2S(s)}} - (Q_{\mathrm{SH(s)}} + Q_{\mathrm{S(s)}}) + D_{\mathrm{H_2S}} - D_{\mathrm{SH}}$$

$$= (19) - (65 + 63) + (173 - 82)$$

$$= -18 \text{ kcal/mol.}$$

Forward activation energy of the elementary reaction step using Eq. 5.24 can be written as

$$\Delta E^*_{\mathrm{for}} = 1/2\left[\Delta H + \frac{Q_{\mathrm{SH(s)}} Q_{\mathrm{S(s)}}}{Q_{\mathrm{SH(s)}} + Q_{\mathrm{S(s)}}}\right]$$

$$= 0.5\left[-18 + \frac{65 \times 63}{65 + 63}\right]$$

$$= 6.996 \text{ kcal/mol.}$$

Next, the activation energy for reverse reaction can be determined using Eq. 5.25

$$\Delta E^*_{\mathrm{rev}} = \Delta E_{for} - \Delta H$$

$$= 6.996 - (-18)$$

$$= 25 \text{ kcal/mol.}$$

5.1.3 Pre-exponential factors

A variety of methods are available to estimate the pre-exponential factors, but this is a challenging task for surface reactions. Generally transition state theory is used to predict the pre-exponential factors for each elementary surface reactions. The critical assumption of the transition state theory is that quasi equilibrium is established between the reactants and an activated complex. Cortright and Dumesic [126, 127] provides the guidelines from which the pre-exponential factors may be estimated using transition-state theory through an order-of magnitude analysis of partition functions for a variety of surface reactions, including adsorption and desorption reactions.

For a bimolecular reaction $A^* + B^* \rightleftharpoons AB^{\ddagger} \rightarrow C^* + D^*$, the forward rate constant for formation of the activated complex is given by [128]

$$k_{AB} = \frac{k_B.T}{h}.K^{\ddagger} = \frac{k_B T}{h}.\exp\left[\frac{\Delta S^{0\ddagger}}{k_B}\right].\exp\left[\frac{\Delta H^{0\ddagger}}{k_B.T}\right] \tag{5.29}$$

where k_B is the Boltzmann constant, T is the temperatute, h is the Planck constant. $\Delta S^{0\ddagger}$ and $\Delta H^{0\ddagger}$ are the entropy and enthalpy change for formation of activated complex $AB^{\ddagger}$, respectively. The activation energy for the forward reaction E_{AB} can be calculated from $\Delta H^{0\ddagger}$ and Eq. 5.29 can be written as

$$k_{AB} = A_{AB}.\exp\left[\frac{-E_{AB}}{k_B.T}\right], \tag{5.30}$$

where A_{AB} is the pre-exponential factor for the forward reaction, given by

$$A_{AB} = \frac{k_B.T}{h}.\exp\left[\frac{\Delta S^{0\ddagger}}{k_B}\right] \tag{5.31}$$

The standard entropy change for formation of the activated complex $AB^{\ddagger}$ from A and B in Eq. 5.31 is

$$\Delta S^{0\ddagger} = S^0_{AB\ddagger} - \left(S^0_A - S^0_B\right) \tag{5.32}$$

where $S^0_{AB^{\ddagger}}$, S^0_A, and S^0_A are the total standard entropies of the individual species. The total standard entropy (S^0_{tot}) of a gas phase species is a summation of contributions from translational, rotational, and vibrational modes.

Generally, a thumb rule for assigning the pre-exponential factors for mono and bi-molecular surface reactions are respectively in the order of 10^{13} sec^{-1} and 10^{21} $\mathrm{con}^{-1}\mathrm{sec}^{-1}$. Dumesic, et al., [127] provides a more detailed examination of the transition state theory applied to the estimation of the pre-exponential factor for several other types of reactions under various conditions.

5.2 Thermodynamic consistency

Thermodynamic consistency of surface reaction mechanism is a key problem for many of the surface reactions. The main reason for this problem is the lack of thermochemical data for surface species. The rate parameters of forward and backward reactions are chosen in ad hoc fashion without maintaining the thermodynamic constraints. This issue has been addressed in many instances [127, 128, 129, 130, 109].

If the reversible surface reaction mechanism is thermodynamically consistent, then any reversible *i*'th reaction in the complex network must follow the enthalpy as well as entropy (Eq. 5.33)consistency given by

$$\Delta H = E_f - E_r, \text{and } \frac{\Delta S}{R} = \ln\left(\frac{A_f}{A_r}\right), \tag{5.33}$$

where ΔH is enthalpy change of reaction, E_f and E_r are the activation energies of forward and reverse reactions respectively, and ΔS is the entropy change. A_f and A_r are the pre-exponential factors of forward and reverse reactions respectively.

Mechanisms that are not consistent in enthalpy results in incorrect solutions of temperature, and inturn wrong predictions in heat exchange and conversion/ selectivity in nonisothermal simulations. Errors can propagate in isothermal simulations as well. Entropy inconsistency is due to the incorrect pre-exponential of surface reactions. Both inconsistencies distorts the underlying thermodynamic principle, which affects the prediction of equilibrium constants and equilibrium states. A previously published alogorithm [131, 105] address the above issues and makes the complex surface reaction mechanism thermodynamically consistent in enthalpy as well as in entropy.

The equilibrium of a chemical reaction is defined as

$$\sum_k \upsilon_{ki}^{'} \rightleftharpoons \sum_k \upsilon_{ki}^{''} A_k \tag{5.34}$$

for any reaction mixture to exist at equilibrium, the rates of the forward and backward (reverse) reactions must be equal. The equilibrium constant K_{pi} is defined as

$$K_{pi} = \prod_k \left(a_k^{eq}\right)^{\upsilon_{ki}} = \exp\left(-\frac{\Delta_i G^0}{RT}\right) \tag{5.35}$$

a_k^{eq} is the equilibrium activity, R is the gas constant, T is the absolute temperature. The change of free enthalpy ΔG_0 at normal pressure p_0 is given by

$$\Delta_i G^0 = \sum_k \upsilon_{ik} G_k^0(T). \tag{5.36}$$

Once the specific heat is known, the other thermodynamic properties can be evaluated in terms of the specific heat. The standard state enthalpy is given as

$$H_k^0 = \int_{T_0}^{T} C_p^0(T^{'}) dT^{'} \tag{5.37}$$

and the standard state entropy by

$$S_k(T) = \int_{T_0}^{T} \left(\frac{C_p^0(T^{'})}{T^{'}}\right) dT^{'}. \tag{5.38}$$

When heat capacity is expressed as fourth order polynomial is given by

$$C_p^0 = R \sum_{n=1}^{5} a_{ni} T^{n-1} = R(a_{1i} + a_{2i}T + a_{3i}T^2 + a_{4i}T^3 + a_{5i}T^4) \tag{5.39}$$

then the standard free enthalpies ($G = H - TS$) can be expressed in terms of seven coefficients, $a_{0,i}, ..., a_{6i}$ as

$$G_k^0 = a_{0,k} + a_{1,k}T + a_{2,k}T^2 + a_{3,k}T^3 + a_{4,k}T^4 + a_{5,k}T^5 + a_{6,k}T \ln T \tag{5.40}$$

The equilibrium of reversible reaction can be written in terms of forward and reverse reaction rates as

$$\frac{k_{fi}}{k_{ri}} = K_{pi} \prod_k \left(c_k^0\right)^{\upsilon_{ki}}, \tag{5.41}$$

where υ_{ki} is the diffrence of stoichiometric coefficients of reactants and products of i'th reaction, c_k^0 are the reference concentrations at normal pressure. i.e.,
for gas-phase species

$$c_k^0 = \frac{p_k^0}{RT} \tag{5.42}$$

for surface species

$$c_k^0 = \frac{\Gamma \theta_k}{\sigma_k} \tag{5.43}$$

where Γ is the total surface site density and σ_k is the site occupancy number of species k.

One problem in calculating the equilibrium constant by Eq.5.35 is unknown thermo-chemistry data for intermediate species. The forward and reverse reaction rates are then defined seperately with their own rate laws. Nevertheless, these rates cannot be chosen independently.

Assuming an initial guess for the rate parameters of a surface reaction mechanism, the rate coefficients for the forward and reverse reactions may be adjusted seperately to make the entire mechanism thermodynamically consistent.

The free energy change for the i'th reaction is calculated based on the initial guess values of rate constants by using Eqs. 5.33

$$\Delta_i G = -RT \ln K_{pi} \tag{5.44}$$

Eq. 5.44 can also be written by using thermo-chemistry data of participating species in the i'th reaction as

$$\Delta_i G = \sum_{k=1}^{N} \upsilon_{ki} G_k^0(T) \tag{5.45}$$

The above equation includes the free energies of gas phase species and surface species in i'th reaction. Eq. 5.45 can be written as

$$\Delta_i G_0 = \sum_{k=1}^{N_u} \upsilon_{ki} \tilde{G_k^0}(T) + \sum_{k=1+N_u}^{N} \upsilon_{ki} G_k^0(T), \tag{5.46}$$

which is a linear equation system for the known (G_k^0) and unknown free enthalpies ($\tilde{G_k^0}$). In the above equation, thermo-chemical properties of $1, ..., Nu$ out of N species are unknown. For each pair of a reversible reactions we can calculate the equilibrium constant according to Eq. 5.41 and, Eq. 5.44 yields change of free enthalpy. Since most of the surface species are involved in more than one reaction, this system is usually over-determined. Equation 5.40 for several temperatures T_j gives a system of linear equations in the unknown coefficients $\tilde{a_{l,k}}$:

$$\sum_{k=1}^{Nu} \sum_{l=0}^{6} \upsilon_{ki} t_{lj} \tilde{a_{l,j}} = g_{i,j}, \tag{5.47}$$

the unknown free enthalpy can be found from Eq. 5.46

$$g_{i,j} = \Delta_i G^0(T_j) - \sum_{k=N_u+1}^{N} \upsilon_{ki} G_k^0(T_j) \tag{5.48}$$

where

$$t_{lj} = \begin{cases} T_j^l & \text{if } l < 6 \\ T_j \ln T_j & \text{if } l = 6 \end{cases} \tag{5.49}$$

An optimal set of parameters $\tilde{a_{l,k}}$ are determined by a weighted least square approximation for each unknown surface species. These weights can be chosen individually for each pair of reactions according to a sensitivity analysis. This guarantees that the equilibrium of crucial reaction steps will be shifted less than others after the adjustment.

The newly calculated polynomials are used to calculate the free enthalpy change for each pair of reaction,

equilibrium constant, and the rate coefficient for the reverse reaction. In case the reverse reaction shall be expressed in terms of Arrhenius coefficients, another least-square approximation using the rate constants at the discrete temperatures, T_j, is performed.

Since the surface reactions are written as pairs of irreversible reactions, this procedure has to be repeated during the mechanism development after modification of any rate coefficients in the reaction network. Fig. 5.1 shows the schematic representation of the adjustment algorithm to setup thermodynamically consistent surface reaction mechanism. Mahedeshwar et al., [109] proposed a mechanism based on the linear base and linear combinations. The main advantage of previously proposed alogorithm [131, 105] is that it is not required to select linear combinations and all reactions are treated equally by solving the linear problem using a least-squart fit.

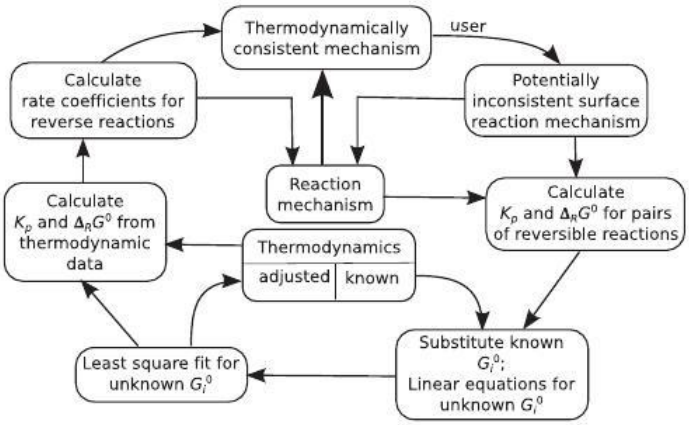

Figure 5.1: Illustration of the adjustment algorithm to set up thermodynamically consistent surface reaction mechanisms.

Chapter 6

Modeling of experiments

This chapter deals with the development and validation of a detailed kinetic model for steam reforming of biogas with and without H_2S. The presence of H_2S in the feed is the root cause for catalyst poisoning during reforming. In order to account for catalyst deactivation, H_2S adsorption, dissociation, disorption, and disproportionation reactions are incorporated into a previously published mechanism of CH_4 steam reforming on Ni. The activation energies for the elementary step reactions are calculated by UBI-QEP method and the entire mechanism is made thermodynamically consistent using algorithm that are discussed in the chapter 5. The developed kinetic model is validated by comparing the model predictions with our experiments and the experiments reported by other research groups. These experiments are performed in isothermal fixed bed reactors. Therefore, a one dimensional fixed bed reactor model is used to simulate the experiments.

6.1 Kinetic model

The main set of the kinetic model is a previously published mechanism for steam reforming of CH_4 on Ni by Janardhanan et al., [132]. Additional reactions are incorporated into this mechanism to account for sulfur adsorption, desorption, disproportionation, and recombination reactions. The UBI-QEP method is adopted to calculate the forward and reversed activation energies of biogas steam reforming reactions. Table 6.1 shows the forward (E_{for}) and reverse (E_{rev}) activation energies for reactions involving sulfur species. The reversible activation energies are forced to zero in Table 6.1 when the activation barrier E_{rev} is negative [121].

6.2 Reactor model

A one-dimensional transient fixed bed reactor model is used for the simulations presented in this thesis. Assuming ideal gas behavior and constant pressure, the partial differential equation that describes the species transport in a fixed bed reactor with constant mass flow rate is:

$$\rho \frac{\partial Y_k}{\partial t} = -\dot{m} \frac{\partial Y_k}{\partial x} + \frac{\partial}{\partial x}\left(\mathcal{D}_{\text{km}} \frac{\partial \rho Y_k}{\partial x}\right) + A_{\text{v}} W_k \dot{s}_k, \quad k = 1, \ldots, N_{\text{g}}. \tag{6.1}$$

Table 6.1: Activation barriers for forward and reversed reactions with sulfur involving reactions.

Reaction	E_{for} (kJ/mol)	E_{rev} (kJ/mol)
H_2S(Ni) +(Ni) $\rightleftharpoons$ SH(Ni) +H(Ni)	29.31	104.67
SH(Ni) +(Ni) $\rightleftharpoons$ S(Ni) +H(Ni)	25.79	143.02
H_2S(Ni) +O(Ni) $\rightleftharpoons$ SH(Ni) +OH(Ni)	27.84	40.40
S(Ni) +O(Ni) $\rightleftharpoons$ SO(Ni) +(Ni)	296.82	0.00
SH(Ni) +O(Ni) $\rightleftharpoons$ SO(Ni) +H(Ni)	206.05	0.00
S(Ni) +OH(Ni) $\rightleftharpoons$ SO(Ni) +H(Ni)	229.02	0.00
SO_2(Ni) +(Ni) $\rightleftharpoons$ SO(Ni) +O(Ni)	106.31	0.00
S(Ni) +H_2O(Ni) $\rightleftharpoons$ SH(Ni) +OH(Ni)	143.37	0.00
SH(Ni) +CO(Ni) $\rightleftharpoons$ S(Ni) +HCO(Ni)	61.82	82.74
SH(Ni) +CO(Ni) $\rightleftharpoons$ SO(Ni) +CH(Ni)	223.41	0.00
S(Ni) +CO(Ni) $\rightleftharpoons$ SO(Ni) +C(Ni)	206.12	0.00

Here, ρ is the density, Y_k is the mass fraction of species k, t is the time, $\dot{m}$ is the mass flux, $\mathcal{D}_{\text{km}}$ is axial dispersion coefficient of species k in the mixture, A_{v} is the active area available for chemical reactions per unit volume, $\dot{s}_k$ is the molar production rate of gasphase species k, W_k is the molecular weight of species k, N_{g} is the number of gasphase species, and x is the axial coordinate. The density ρ is calculated from the ideal gas equation:

$$p\bar{M} = \rho RT, \tag{6.2}$$

where $\bar{M}$ is the average molecular weight, R is the gas constant, and T is the temperature. The axial dispersion coefficient of species k in the mixture $\mathcal{D}_{\text{km}}$ is calculated according to

$$\mathcal{D}_{\text{km}} = \frac{1 - Y_k}{\sum_{j \neq k}^{N_{\text{g}}} X_j / \mathcal{D}_{\text{jk}}}. \tag{6.3}$$

Here X_j is the mole fraction of species j, and the binary diffusion coefficient $\mathcal{D}_{\text{jk}}$ is calculated according to Chapman-Enskog theory [133]. Since the catalyst poisoning is mainly due to loss in active surface area A_{v} is not a constant and changes with sulfur coverage. In the present calculations, we assume a linear dependence of A_{v} on the sulfur coverage [84]. i.e.,

$$A_{\text{v}} = A_{\text{v0}}(1 - \theta_{\text{s}}), \tag{6.4}$$

where, A_{v0} is the active area available before poisoning and θ_{s} is the surface coverage of sulfur. When the surface is fully covered with sulfur, the active area becomes zero. Assuming surface diffusion to be negligible, the fractional surface coverage θ of various species is calculated from [105]

$$\frac{d\theta_k}{dt} = \frac{\sigma_k \dot{s}_k}{\Gamma}, \quad k = N_{\text{g}} + 1, \ldots, N_{\text{g}} + N_{\text{s}}. \tag{6.5}$$

Here σ_k is the number of sites occupied by adsorbed species k, Γ is the total site density, $\dot{s}_k$ is the molar production rate of surface adsorbed species k, and N_{s} is the number of surface species. Calculation of $\dot{s}_k$ from an elementary like reaction mechanism is decribed in Chapter 4. Method of lines is applied to solve equations 6.1 and 6.5 simultaneously by using the ODE solver CVODE [134]. The entire model is implemented in C++.

6.3 Results and discussion

The detailed kinetic model developed for reforming of biogas on Ni is given in Table 6.2. The mechanism contains 68 reactions among 8 gasphase species, 17 surface adsorbed species, and the catalytic surface. While solving 6.5, the catalytic surface is also considered as a surface species. i.e., N_s includes the surface adsorbed species and the free catalytic surface. The adsorption of gas phase species on the catalytic surface is expressed as sticking reactions. It is generally well accepted that, H_2S chemisorbs dissociatively on Ni surface. However, there is no consensus on the number of Ni sites required for dissociative adsorption or the number of active sites that a sulfur atom may occupy. It is likely that at low temperature, the dissociative adsorption involves two Ni sites and at high temperature it involves only one Ni site. Although Rostrup-Nielsen [135] postulates the following scheme

$$H_2S(g) + Ni \rightleftharpoons Ni - S + H_2(g) \tag{6.6}$$

for the adsorption of H_2S on Ni at high temperature, Rostrup does not make a final claim on this. Nevertheless, his data fitting to Langmuir isotherm leads to the conclusion that sulfur occupies only one site at high temperature. Since the mechanism developed here is for use at high temperature, sulfur is assumed to occupy only one site. Formation of bulk sulfide is not considered in this study as they form only at significatly high H_2S partial pressures [135]. For the disproportionation and recombination reactions the activation energies are calculated by applying UBI-QEP method. The pre-exponential factors are adjusted to reproduce the experimental observations and the entire reaction mechanism is made thermodynamically consistent by using the method described in Chapter 5. Sensitivity analysis is performed to elucidate the effect of various reaction parameters on sulfur coverage. In the analysis presented here, the sensitivity coefficients are defined as follows

$$SC = \frac{\phi - \phi_0}{\phi_0}, \tag{6.7}$$

where

$$\phi = \frac{1}{\tau}\int_0^t \theta_s dt, \quad \phi_0 = \frac{1}{\tau}\int_0^t \theta_s^0 dt. \tag{6.8}$$

Here ϕ is the total surface coverage of sulfur for ±5% change in pre-exponential factors and ϕ_0 is the total surface coverage of sulfur for pre-exponential factors as noted in Table 6.2. Figure 6.1 shows the scaled value of the sensitivity coefficient with respect to absolute maximum for major reactions that affect the formation of sulfur on Ni. The most sensitive reactions for the formation of adsorbed sulfur is the H_2S sticking reaction (R7) and H_2S desorption reaction (R45). An increase in sticking coefficient results in higher sulfur coverage, whereas an increase in H_2S desorption pre-exponential factor results in lower sulfur coverage. The sticking coefficient of H_2S is generally found be higher than 0.5 [85]. Therefore, in this mechanism we used a sticking coefficient of 0.6 for H_2S. In addition to these reactions, hydrogen abstraction reaction from H_2S and the reaction between adsorbed H_2S and O atom are also found to be influencing the formation of adsorbed sulfur. A positive change in R52 leads to the formation of SH, which further dissociates to give adsorbed sulfur. Since surface coverage of O facilitates the formation of SH from adsorbed H_2S through R52, a positive change in R16 also results in more adsorbed sulfur. Increasing the pre-exponential factor of R52 and R47 also results in faster deactivation.

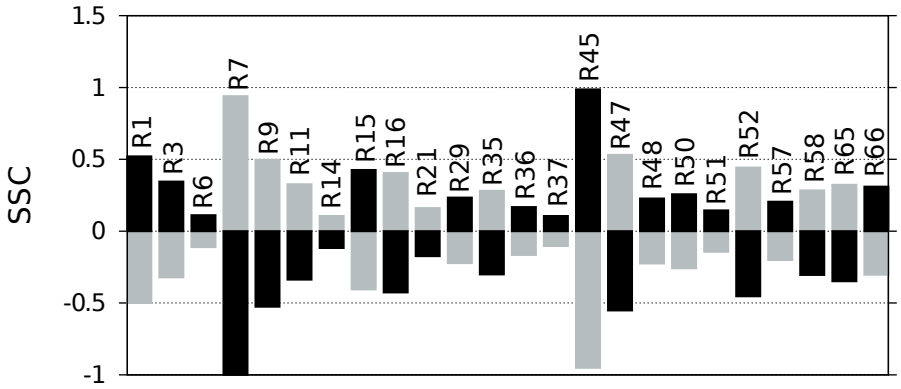

Figure 6.1: Scaled sensitivity of various reactions on sulfur coverage. Gray bars represent a 5% increase in the pre-exponential factors and black bars represent 5% decrease in pre-exponential factors.

The kinetic model presented in 6.2 is developed by fine tuning the pre-exponential factors to reproduce our own experiments. The only adjustable parameter in the modeling results presented below is A_{v0}. To check the predictive capability of the mechanism we have simulated the experiments reported by other research groups [136, 45, 23] in addition to our own experiments. In addition to predicting catalyst deactivation, the mechanism is also capable of predicting the product composition under non poisoning conditions.

6.3.1 Model predictions without sulfur poisoning

Comparison between model predictions and experimental observations made by Ashrafi et al. [136] for CH_4 and CO_2 conversions are shown respectively in Fig. 6.2 and Fig. 6.3. The experiments were performed in a fixed bed reactor with S/C ratio of ~2.7 and CH_4 to CO_2 ratio of 1.5. The reactor model described above is used for the simulations. The steady state model predictions for CH_4 conversions are in good agree-

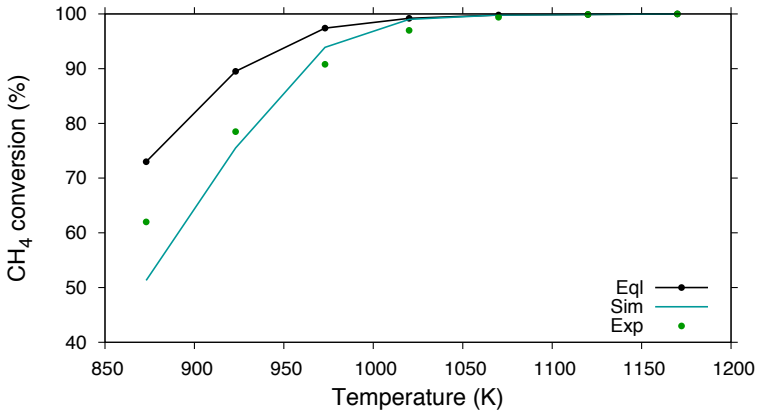

Figure 6.2: Comparison between CH_4 experimental data (Exp), equilibrium predictions (Eql), and model predictions (Sim). The experimental data is from [136]. The S/C ratio employed is ~2.7 and CH_4/CO_2 ratio is 1.5.

ment with the experimental observations and are well within the limits of equilibrium predictions. Deviation from experimental observation is present only at low temperatures (873 K), which are not anyway practically

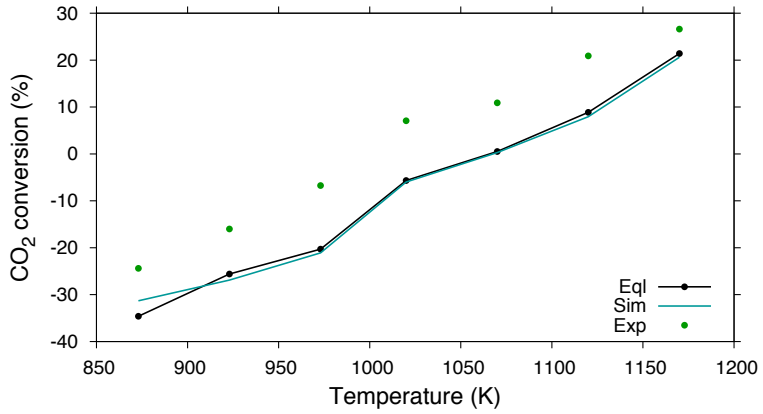

Figure 6.3: Comparison between CO_2 experimental data (Exp), equilibrium predictions (Eql), and model predictions (Sim). The experimental data is from [136]. The S/C ratio employed is ~2.7 and CH_4/CO_2 ratio is 1.5.

useful for biogas reforming. As far as CO_2 conversions are concerned, the experimental observations violate thermodynamic predictions. Thermodynamics predicts the maximum possible conversion or production. Although the experimentally observed CO_2 production (negative conversion in Fig. 6.3) is within the thermodynamic limits, the observed conversions are above that predicted by thermodynamics. The increase of CO_2 conversion in Fig. 6.3 with temperature shows that the methane dry reforming reaction takes place. At higher temperatures, this endothermic reaction is favored and therefore CO_2 is consumed. At temperature below 700 °C, CO_2 is negative due to the due to the water gas shift reaction. The Nevertheless, the model predictions are well within the thermodynamic limit. The comparison between model predictions and experimental observation for CO selectivity and H_2 yield are shown respectively in Fig. 6.5 and Fig. 6.4.

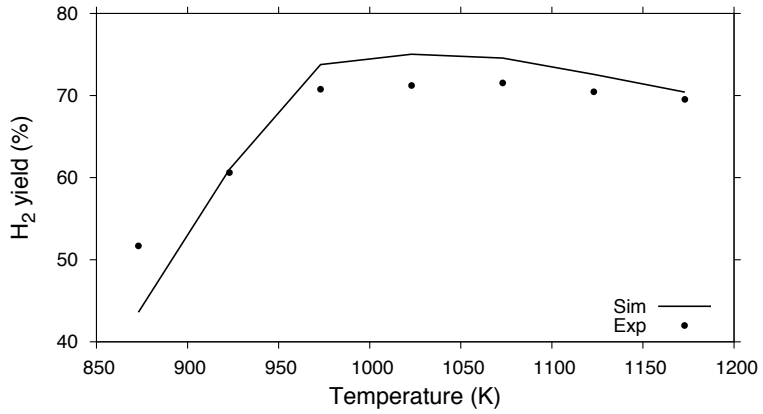

Figure 6.4: Comparison between H_2 experimental data (Exp) and model predictions (Sim). The experimental data is from[136]. The S/C ratio employed is~2.7 and CH_4/CO_2 ratio is 1.5.

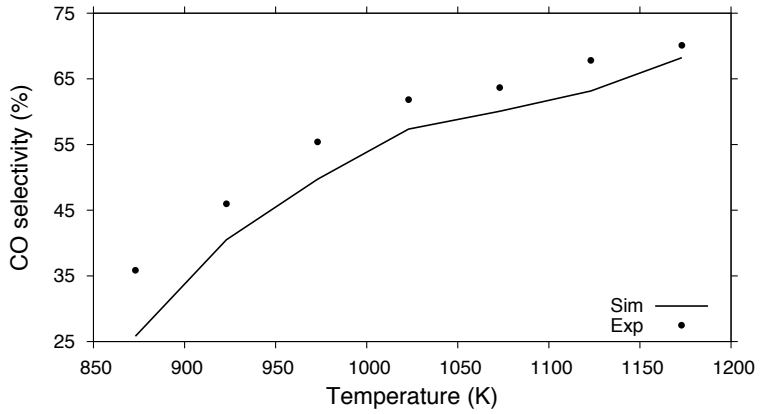

Figure 6.5: Comparison between CO experimental data (Exp) and model predictions (Sim). The experimental data is from[136]. The S/C ratio employed is~2.7 and CH_4/CO_2 ratio is 1.5.

In both cases the model predictions are in very good agreement with the experimental observations. For the given S/C ratio CO_2 participates in the reforming reaction only at temperatures higher than 1050 K. However, at 1050 K CH_4 conversion is almost 97% and therefore, the CO_2 production below 1050 K is probably due to water gas shift reaction. When the temperature exceeds 1050 K, the H_2 yield starts decreasing and the CO_2 conversion becomes positive; this indicates the occurrence of reverse water gas shift reaction. The reverse water gas shift reaction at high temperature is also confirmed by the increasing CO selectivity (Fig.6.5).

The kinetic model also able to reproduce the experiments reported by Kolbitsch et al., [45]. The experiments are performed in a fixed bed reactor with S/C ratio 2.2 and CH_4 to CO_2 ratio of 1.5. Figures. 6.6 and 6.7 shows the steady state model predictions and experimental observations of CH_4 and CO_2 conversions respectively. Again very good agreement is observed between the model predictions and the experimental observations of CH_4 conversions at temperatures above 1023 K. Deviations are obseved in CO_2 conversions, but model predictions of CO_2 conversions are within the themodynamic equilibrium limits. Figure 6.7 shows an increase in CO_2 conversion with temperature, which indicates dry reforming reaction. At higher temperatures, this reaction is favored and therefore CO_2 is consumed. For all these simulations CO and H atoms are found to be the major surface adsorbed species.

6.3.2 Model predictions with sulfur poisoning

Comparison between the model predicted and experimentally observed deactivation at 973 K and 1073 K is shown respectively, in Fig. 6.8 and Fig 6.9. The initial inlet mixture to the reactor contains 12.5%CH_4 , 8.4% CO_2 , 25.2% H_2O and 53.9% N_2 and the gas hourly space velocity is 3.35×10^4 h^{-1}. H_2S (20 and 50 ppm) is introduced after 1 hr into the experiments during which the reactor reaches steady state operation. The experiments simulated in this work represent the catalyst activity loss in terms of drop in CH_4 conversion. The 6 cm long fixed bed reactor is simulated using the reactor model resented earlier. At 973 K, the model very well captures the experimentally observed deactivation profile for 20 ppm H_2S in the feed gas, but an early deactivation for 50 ppm (Fig. 6.8). Nevertheless, the qualitative nature of the deactivation profile and steady state conversions are well predicted. At 1073 K, the model-predicted deactivation matches very well with the experimental observation (Fig. 6.9). Active surface area $A_{v0} = 18\times10^4$ m^{-1} is used at 973 K and A_{v0}

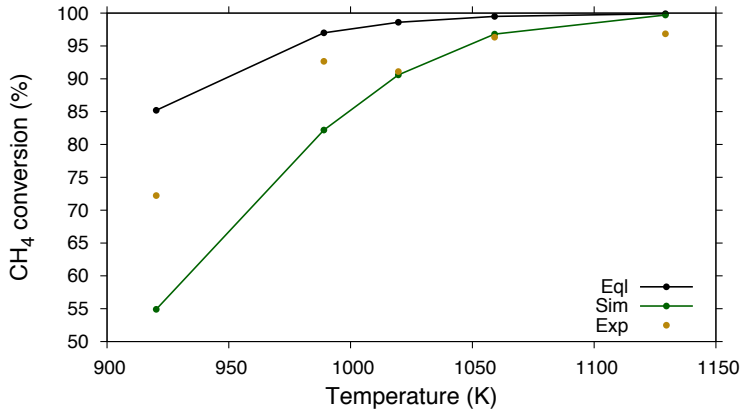

Figure 6.6: Comparison between CH_4 experimental data (Exp) and model predictions (Sim). The experimental data is from [45]. The S/C ratio employed is~2.2 and CH_4/CO_2 ratio is 1.5.

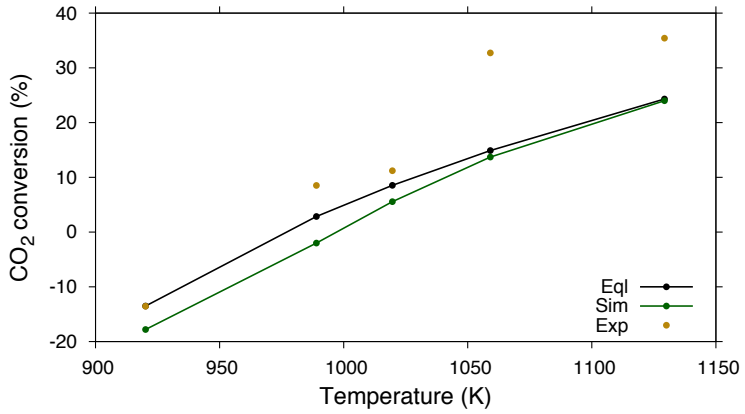

Figure 6.7: Comparison between CO_2 experimental data (Exp) and model predictions (Sim). The experimental data is from[45]. The S/C ratio employed is~2.2 and CH_4/CO_2 ratio is 1.5.

= 15×10^4 m^{-1} is used at 1073 K.

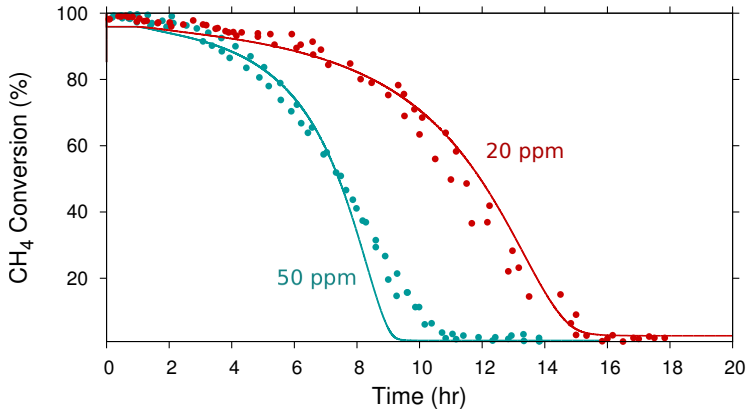

Figure 6.8: Comparison between the model predicted deactivation and experimental observations made at 973 K.

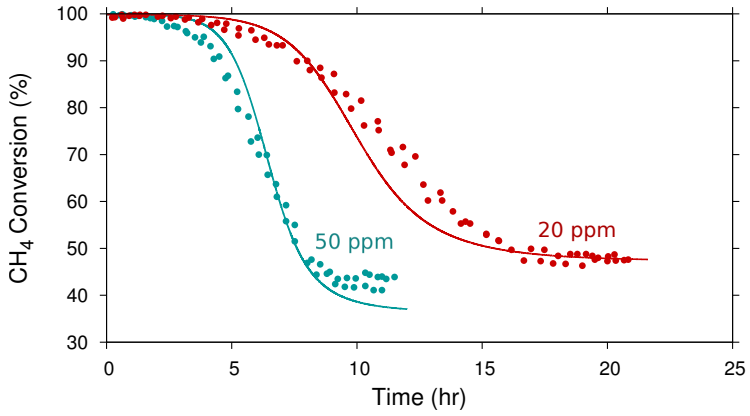

Figure 6.9: Comparison between the model predicted deactivation and experimental observations made at 1073 K.

The product composition from the reactor exit (on dry basis) during deactivation of the catalyst for 20 ppm and 50 ppm H_2S in the feed gas at 973 K is shown respectively in Fig. 6.10 and Fig. 6.11.

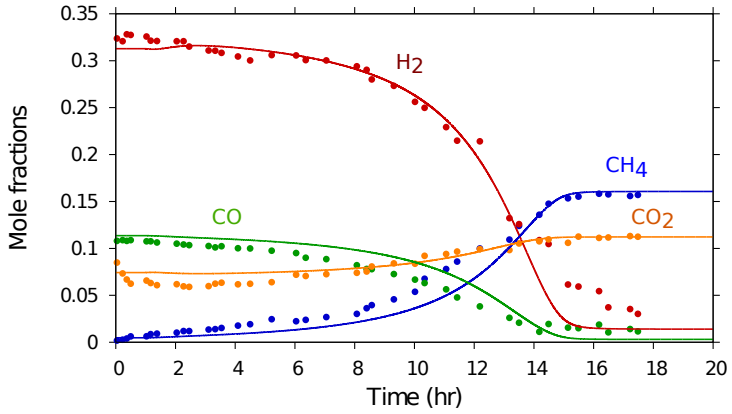

Figure 6.10: Comparison between the model predicted product composition during catalyst deactivation and experimental observations made at 973 K for 20 ppm H_2S in the feed.

The model predictions are in excellent agreement with the experimental measurements. At steady state the product mixture mainly contains H_2, CO, CO_2 and N_2, however, N_2 mole fractions are not shown in the figure. As soon as H_2S is introduced, the mole fractions of H_2 and CO starts to decrease and CO_2 and CH_4 starts to increase. This means that CO_2 also participated in the reforming reactions for the S/C ratio employed here (S/C=2.02). Generally CO_2 does not participate in reforming reactions at high S/C ratio; however, this is temperature dependent. For instance at 1023 K, CO_2 participates in reforming reaction only at S/C ratio below 2.5 [45]. The product mole fractions on dry basis for 20 ppm and 50 ppm H_2S at 1073 K are shown in Fig. 6.12 and Fig. 6.13. As observed at 973 K and 20 ppm, the mole fractions of H_2 and CO start to decrease after introducing H_2S. Due to 100% CH_4 conversion there is no significant difference in the steady state mole fractions of CO and H_2 before introducing H_2S compared to operation at 973 K. However, higher operating temperature is beneficial in maintaining catalytic activity. Unlike operating at 973 K, the catalytic activity is not fully compromised at 1073 K even with higher H_2S content in the feed gas (Fig. 6.9). This low

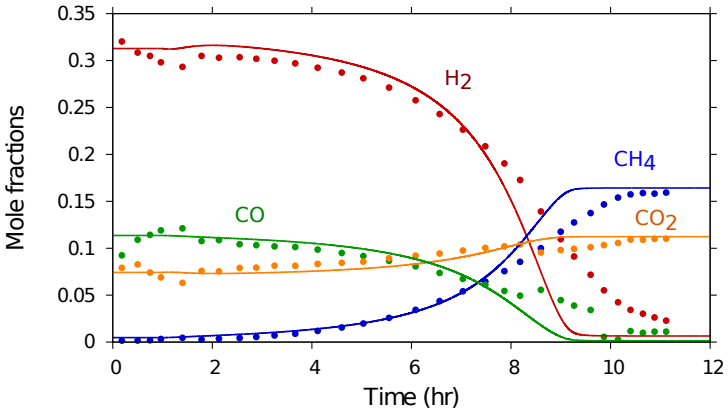

Figure 6.11: Comparison between the model predicted product composition during catalyst deactivation and experimental observations made at 973 K for 50 ppm H_2S in the feed.

degree of activity loss at high temperature is due to the exothermic nature of chemisorption reactions. This leads to higher CH_4 conversion and hence higher H_2 and CO mole fractions, after achieving the saturation sulfur coverage at 1073 K. However, at 1073 K there is a slight disagreement with the model predictions and experimental observation for the mole fractions of H_2 and CO_2 at steady state after poisoning. The model slightly under predicts H_2 and CO_2 for 20 ppm at steady state (Fig. 6.12). Similar behavior is observed for 50 ppm H_2S in the feed gas at 1073 K 6.13.

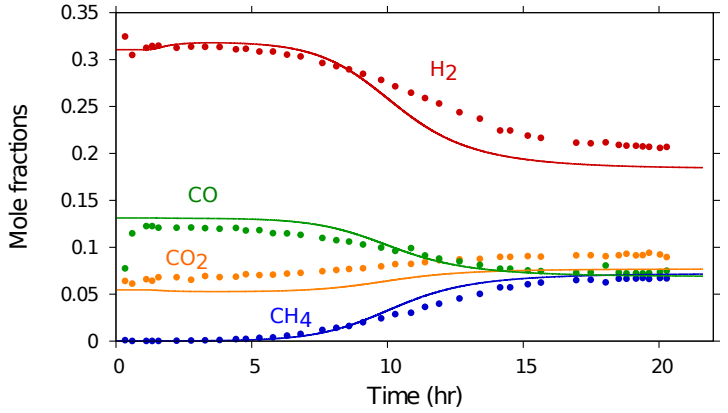

Figure 6.12: Comparison between the model predicted product composition during catalyst deactivation and experimental observations made at 1073 K for 20 ppm H_2S in the feed.

The average fractional surface coverage of various surface adsorbed species and free surface along the length of the reactor as a function of time for 973 K and 1073 K with 20 ppm H_2S in the feed mixture is shown respectively in Fig. 6.14 and Fig. 6.15. The major surface adsorbed species before introducing H_2S into the feed are CO and H atom and most of the surface remains open for adsorption. As soon as H_2S is introduced, sulfur starts to occupy most of the surface and the coverages of CO and H starts to decrease. After poisoning at 973 K, adsorbed sulfur occupies 92.0% of the surface with 4% open surface. CO and H atoms still remain as the other major species on the surface. The average fractional surface coverage of sulfur increases linearly and then reaches the steady state asymptotically. At 1073 K, sulfur occupies only 66% of

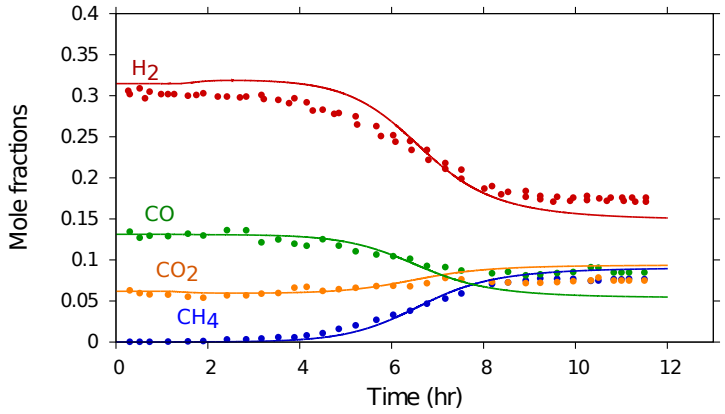

Figure 6.13: Comparison between the model predicted product composition during catalyst deactivation and experimental observations made at 1073 K for 50 ppm H_2S in the feed.

the surface with 16% open surface.

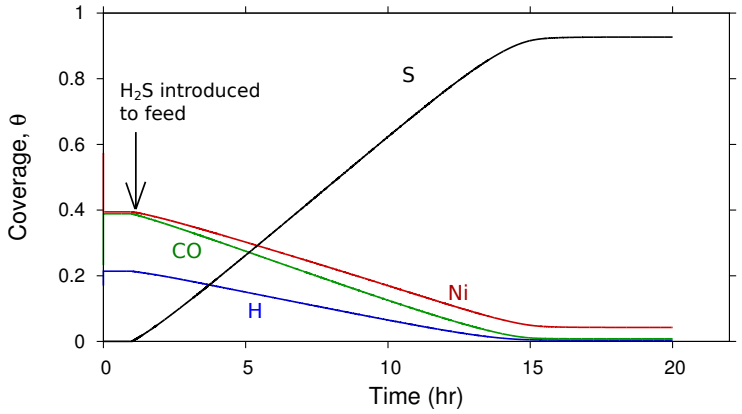

Figure 6.14: Average fractional coverage along the length for major surface adsorbed species and the free coverage as a function of time at 973 K. The inlet mixture contains 20 ppm H_2S.

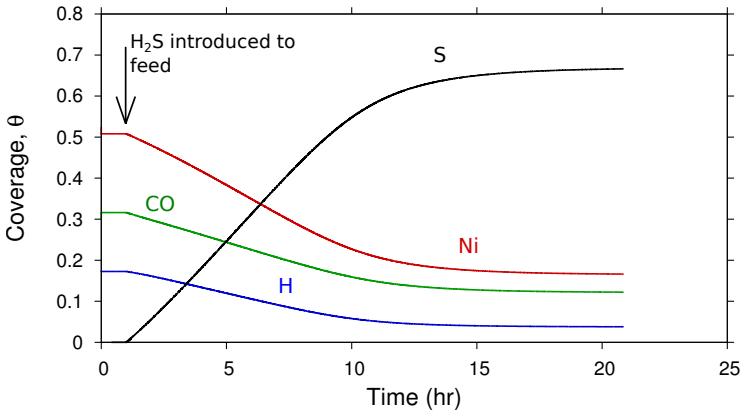

Figure 6.15: Average fractional coverage along the length for major surface adsorbed species and the free coverage as a function of time at 1073 K. The inlet mixture contains 20 ppm H_2S.

However along the length of the reactor, the poisoning is not uniform. Figures 6.16 and 6.17 shows the buildup of sulfur coverages at 973 K and 1073 K along the length of the reactor. At both temperatures, the poisoning occurs from inlet towards the exit of the reactor as time proceeds. In fact as the poisoning proceeds, the location of the methane reforming reaction moves downstream through the reactor length. This sort of wave behavior is typical for parallel poisoning [70].

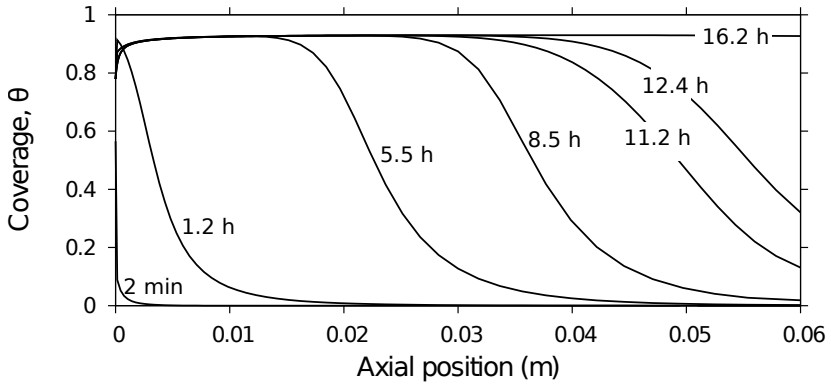

Figure 6.16: Transient fractional surface coverages of sulfur at 973 K. The inlet mixture contains 20 ppm H_2S.

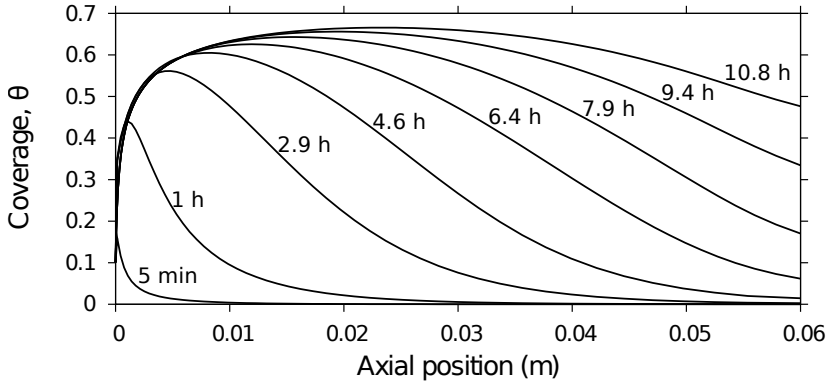

Figure 6.17: Transient fractional surface coverages of sulfur at 1073 K. The inlet mixture contains 20 ppm H_2S.

The predictive capability of the model is further explored by simulating the deactivation experiments reported by Ashrafi et al. [23]. The simulations are again performed using the fixed bed reactor model with CH_4 to CO ratio of 1.5 and S/C ratio is of ~3.0, for these simulations active surface area A_{v0} = 5520×10^3 m^{-1} is used. Figure 6.18 shows the model predictions against the experimentally observed CH_4 conversions for two different H_2S concentrations (31 ppm and 108 ppm) in the feed gas for reactor operating at 1073 K. The model very well predicts the experimentally observed CH_4 conversion for 31 ppm H_2S. However, for the 108 ppm case, the CH_4 conversions are over predicted. The model predicts 37% conversion, while the experimentally observed conversion is only 18%. This may be attributed to the inconsistencies in the reported experimental data. A careful examination of CH_4 conversions reported by Ashrafi et al. for 1073 K reveals some discrepancy in their data. In one case they report steady state CH_4 conversion of 32% at 1073 K with

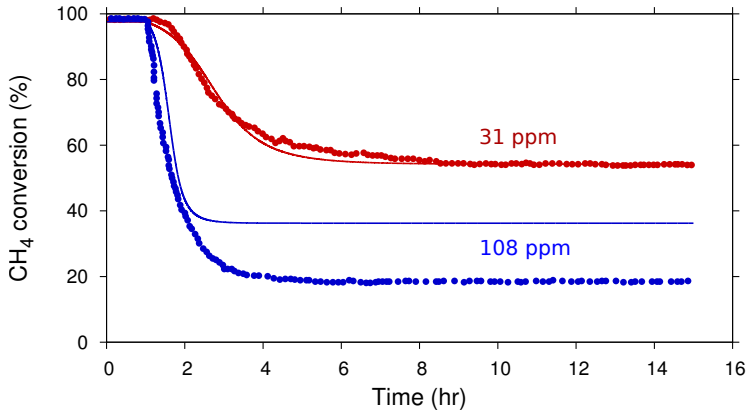

Figure 6.18: Comparison between the model prediction and experimental observation for CH4 conversion at 1073 K. Initial inlet mixture to the reactor contains CH_4 to CO_2 ratio of 1.5 and S/C ratio of ~3.

145 ppm H_2S in the feed mixture. In another case they report 18% conversion for 108 ppm H_2S in the feed gas. These two are contradictory results, if 108 ppm H_2S results in 18% CH_4 conversion, then 145 ppm must result in a lower CH_4 conversion. Therefore, it is most likely that the the error is in the data reported at 108 ppm and in fact 108 ppm must result in higher CH_4 conversion, which is consistent with the predictions of the present model. At 1173 K, the model predictions are in good agreement with experimental observations. Figure 6.19 shows the comparison between the model predictions and the experimentally measured data.

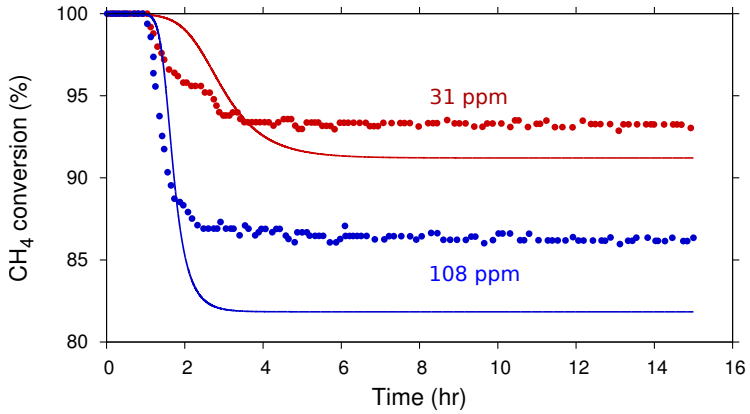

Figure 6.19: Comparison between the model prediction and experimental observation for CH4 conversion at 1173 K. Initial inlet mixture to the reactor contains CH_4 to CO_2 ratio of 1.5 and S/C ratio of ~3.

The model predicts 82% CH_4 conversion at 1173 K with 108 ppm H_2S in the feed gas, while the experimentally observed conversion is 86%. For 31 ppm, the model predicted conversion (91%) is very close the experimentally observed conversion of 93%. One may notice that the inlet composition used by Ashrafi et al. is different from the ones used in our own experiments. Thus, the model that is developed based on experiments conducted at one fixed composition, is able to predict catalyst deactivation at other conditions as well. Although the model predicts the deactivation profile for 108 ppm H_2S reported by Ashrafi et al. [23], it failed to predict the deactivation profiles with 100 ppm H_2S in the feed gas for our own experiments. Therefore, we can say that the confidence interval for the model is 20 to 50 ppm H_2S in the feed gas for 973-1123 K.

6.3.3 Model predictions with catalyst regeneration

Catalyst regeneration by H_2S removal

Experimentally it was possible to regenerate the catalyst by removing H_2S from the feed gas. The same is attempted in the simulations by removing H_2S from the feed gas at 1073 K. Figure 6.20 shows CH_4 conversion with time on stream for 20, 50, and 100 ppm H_2S. As observed in the experiments, the model predicted recovery in the catalyst activity. However, the model predicts slow regeneration compared to the experimental observations. The recovery in catalyst activity on removal of H_2S from the feed stream is due to the reversible nature of chemisorption reactions. Figure 6.21 shows for predicted mole fractions at reactor exit during the deactivation and regeneration. Before introducing H_2S in the feed CH_4 is completely converted by steam and dry reforming reactions. As soon as H_2S is introduced to the reactor, the reactants mole fraction starts to increase and the products mole fraction starts to decrease. The mole fraction of CH_4 and CO_2 increases and stabilizes respectively at 8.7% and 9.3%. After removing the H_2S from the feed, the reactants mole fractions starts to decrease and products molefractions starts to increase slowly. This indicates that the adsorbed sulfur is slowly oxidized by surface species and desorbed as SO_2 to the gas phase and more free surface becomes available to the steam and dry reforming reactions.

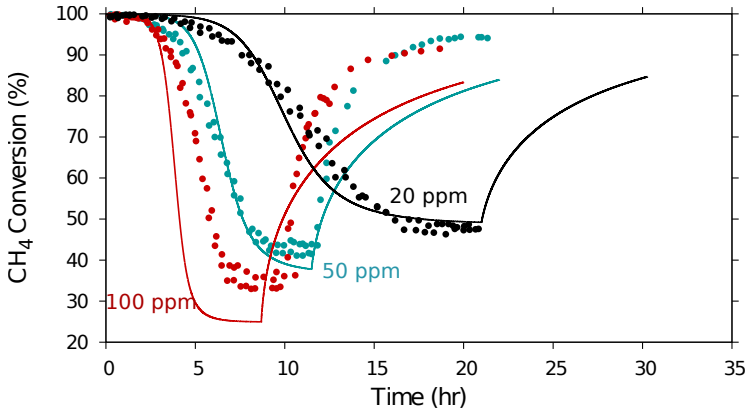

Figure 6.20: Comparison between the model prediction and experimental observations made at 1073 K. Different concentrations (ppm) of H_2S are introduced after reaching steady state.

Figures 6.22, 6.23, 6.24, and 6.25 shows the surface coverages along the length of the reactor at various time instances for the reactor operating at 1073 K with 50 ppm H_2S in the feed stream. The major surface adsorbed species before introducing H_2S in to the feed are CO and H atom and 50% of the surface remains open for reactions (Fig. 6.22). During the initial stages of poisoning (15 min after introducing H_2S), sulfur coverage is high near the reactor inlet (Fig. 6.23) and CO and H occupies most of the remaining surface. Figure. 6.24 shows steady state poisoning, and adsobed sulfur occupies 74% of the surface with 2% open surface. Figure 6.25 shows the surface profiles after 10.30 hrs catalyst regeneration. As soon as H_2S is removed from the feed stream the sulfur coverages start to decrease and CO and H occupy the most of the surface. The kinetic model predicts slow recovery of the catalyst as opposed to experimental observation.

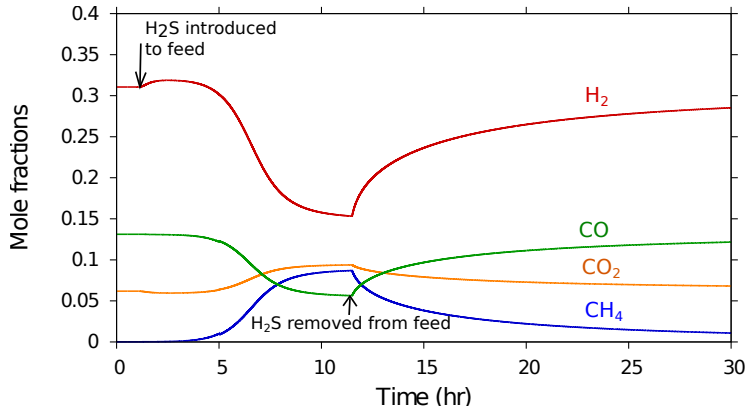

Figure 6.21: model predictions of reactor exit molefractions during catalyst deactivation and regeneration at 1073 K for 50 ppm H_2S in the feed.

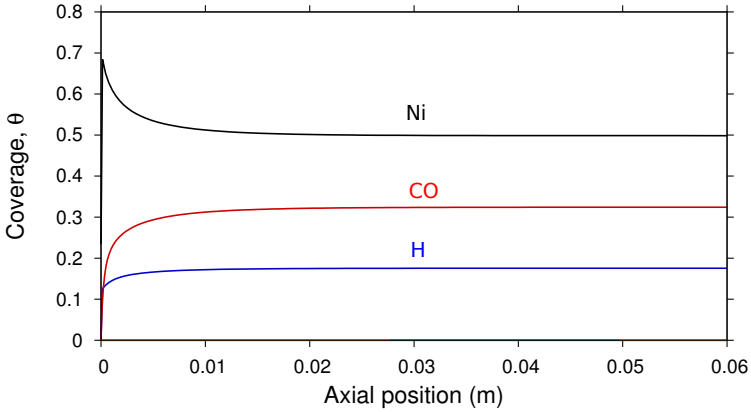

Figure 6.22: Fractional coverages of various surface adsorbed and free surface along the length of the reactor before introducing H_2S.

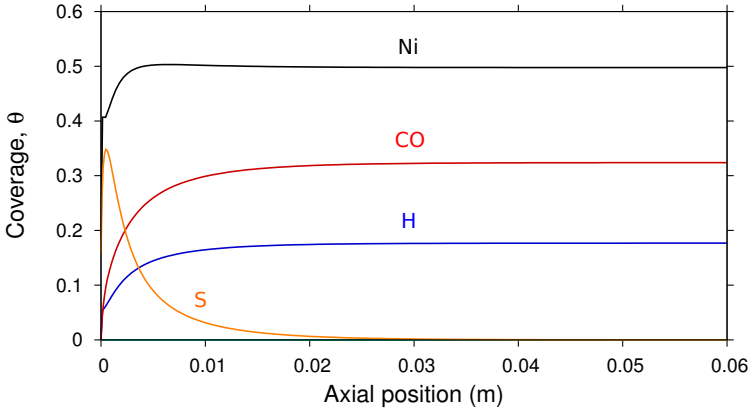

Figure 6.23: Fractional coverages of various surface adsorbed and free surface along the length of the reactor 15 min after introducing H_2S.

The fractional surface coverages of major species during the poisoning and regeneration is shown in Fig. 6.26. As soon as H_2S is introduced, sulfur starts to occupy most of the surface and the coverages of CO

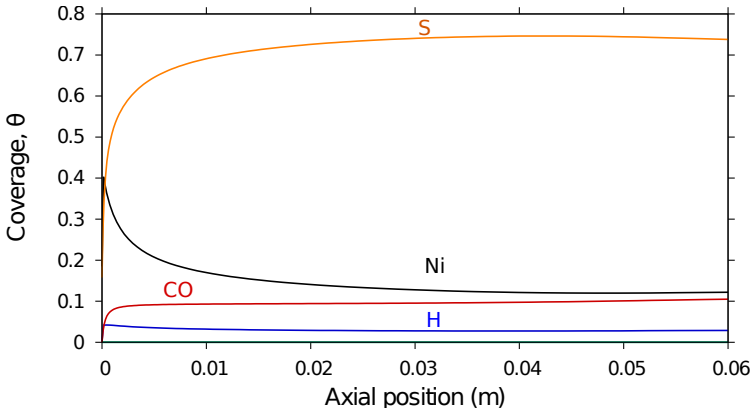

Figure 6.24: Steady state fractional coverages of various surface adsorbed and free surface along the length of the reactor after poisoning.

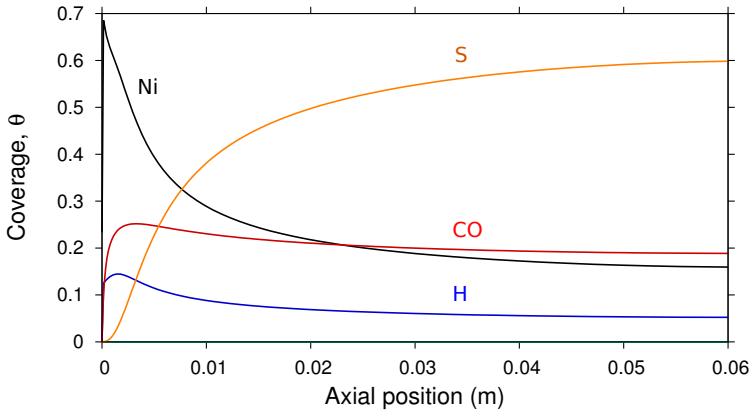

Figure 6.25: Fractional coverages of various surface adsorbed and free surface along the length of the reactor after 10.30 hrs of regeneration .

and H starts to decrease. After poisoning, adsorbed sulfur occupies 74% of the surface with 2% open surface. CO and H atoms still remain as the other major species on the surface. As soon as H_2S is removed from the feed stream the sulfur coverage starts to decrease. As sulfur coverages starts to decrease, CO and H begins to occupy most of the surface.

Catalyst regenration by temperature Enhancement

Since the chemisorption is exothermic, the activity of the catalyst can also be recovered by increasing the temperature [100]. Figure 6.27 shows the model predicted and experimentally observed CH_4 conversion during temperature enhancement from 973 K to 1073 K. The initial mixture contains 100 ppm H_2S and catalyst is fully poisoned at the first steady state. Although, the model predicts early loss in activity the steady state is well predicted. The second steady state is achieved by increasing the temperature from 973 K to 1073 K. The model slightly under predicts the CH4 conversion at second steady state. When the model predicted only 25% conversion, the experimentally observed conversion is 30%. From the second steady state, the catalyst activity is further recovered by removing H_2S from the feed gas. The model predicted very slow regeneration compared to the experiments. The corresponding model predicted and experimentally observed mole frac-

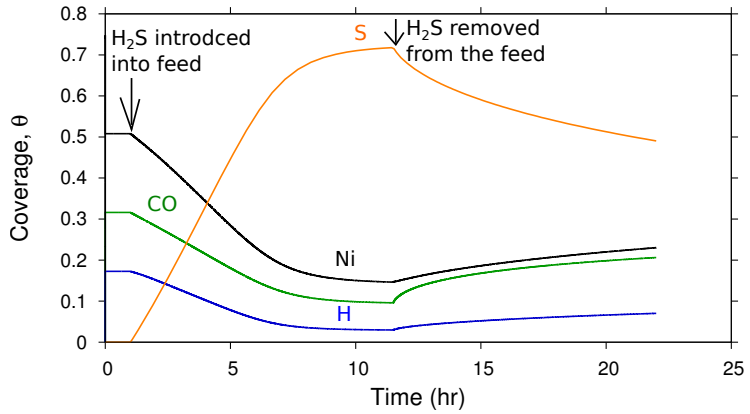

Figure 6.26: Average fractional coverage along the length for major surface adsorbed species and the free coverage as a function of time at 1073 K. The inlet mixture contains 50 ppm H_2S.

tions from the reactor are shown in Fig. 6.28. In all these cases, the model is able to predict the steady state reasonably well, however, fails to predict the time on stream behavior.

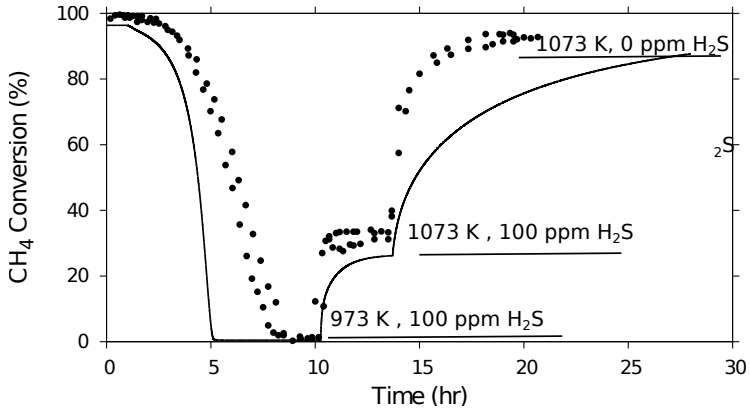

Figure 6.27: Comparison between the model prediction and experimental observation for catalyst regeneration by temperature enhancement.

6.3.4 Effect of steam to carbon ratio

The simulations are extended to study the deactivation behaviour at 50 ppm H_2S by varying steam to carbon ratio (S/C). Figure 6.29, 6.30 shows the conversion of methane as a function of time at diffrent S/C ratios. An increase in S/C ratio has no effect on methane conversion at 700 °C but has a positive effect at 800 °C. At 700 °C, the addition of steam may not effect the chemisorption equilibrium of sulfur [100]. Furthermore, the deactivation profile and steady state conversions are similar at various S/C ratios. The steady state converson of CH_4 after poisoning increases with increase in S/C ratio at 800 °C. The methane convesion at S/C = 2.02 is 37%, and at S/C = 4.0 is 55%. High steam concentration in the feed may produce sufficient OH(Ni) and O(Ni) species on the surface, and oxidize the adsorbed sulfur to SO_2. This may be further confirmed from Fig. 6.31, which shows decrease in average fractional sulfur coverages with increasing S/C ratios. For example, at S/C= 2.02 and 4.0, the average sulfur covergaes are 72% and 67% respectively.

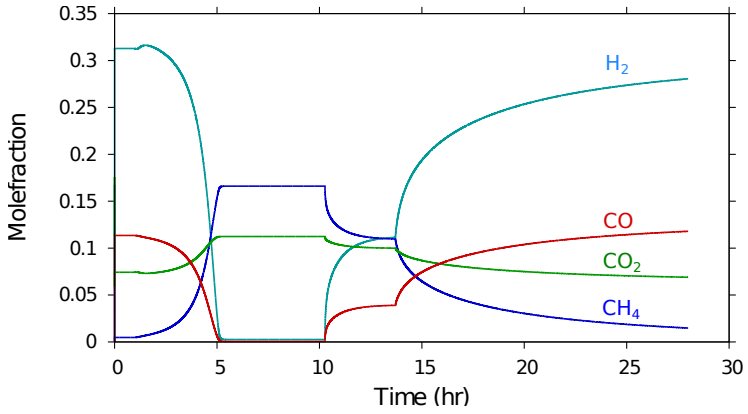

Figure 6.28: Comparision between model predicted gas phase compositions and experimental observations during catalyst deactivation and regeneration.

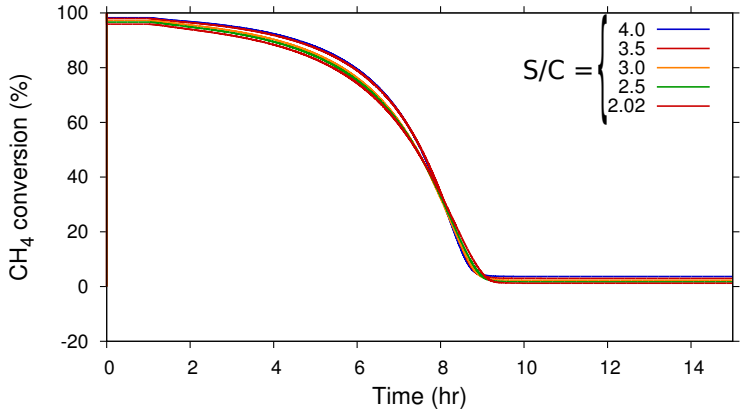

Figure 6.29: Model predictions of CH_4 converion at various S/C ratios at 700 °C.

Finally the saturation coverages predicted by the model at different temperatures are shown Fig. 6.32. These linear trends are very much similar to the experimental observation by Nielsen et al. [137]. Although a direct comparison is not possible due to the difference in composition of the feed gas that is reported in dry basis, a qualitative agreement can be observed between the model predictions and experimental observations reported in [137]. The dry gas composition reported in [137] contains all the chemical species considered in this work. The authors report saturation sulfur coverages higher than 90% at 973 K for 50, 10 and 2 ppm H_2S in the feed gas, and our model also predicts saturation coverages higher than 90% at 973 K. Similar to the experiments, the model also predicts a linear decrease in sulfur coverage with increase in temperature.

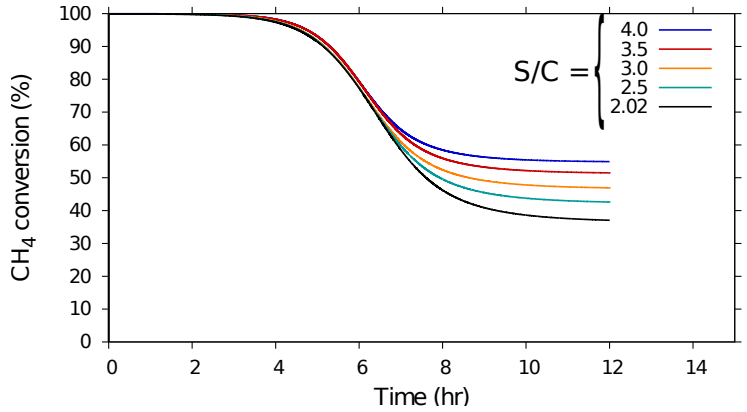

Figure 6.30: Model predictions of CH_4 converion at various S/C ratios at 800 °C

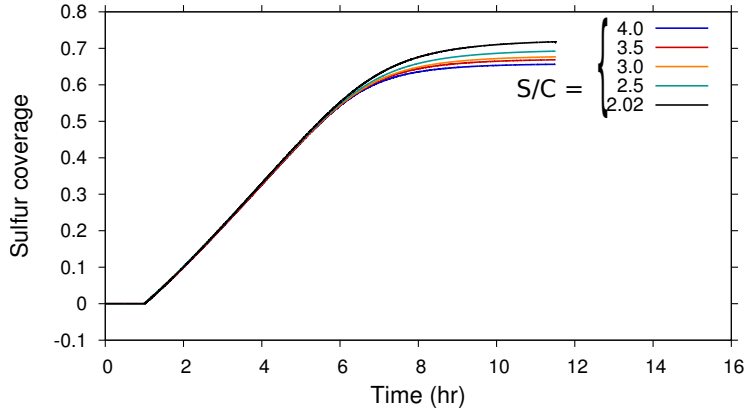

Figure 6.31: Average fractional sulfur coverages at various S/C ratios at 800 °C

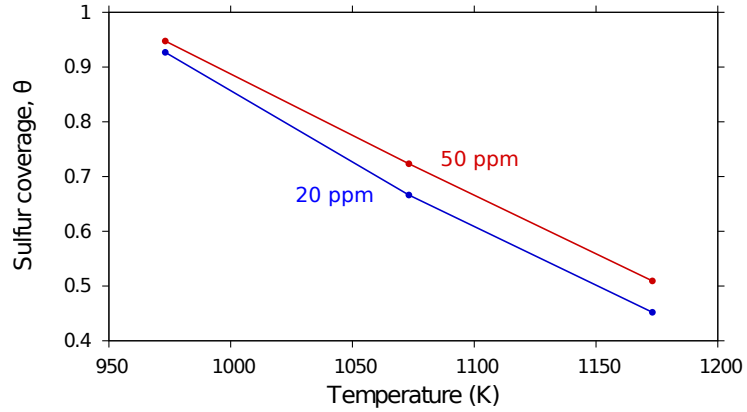

Figure 6.32: Model predicted saturation coverages at different temperatures.

6.4 Conclusions

A detailed kinetic model for simultaneous dry and steam reforming of biogas on Ni based catalyst is developed and validated against experimental data. The model can be used for simulating reforming of biogas

with and without H_2S. The catalyst deactivation is represented in terms of loss in CH_4 conversion at different temperatures and H_2S concentrations. The model is developed by fine tuning the pre-exponential factors to reproduce the experimental observations. The entire mechanism is made thermodynamically consistent by using method described in Chapter 5. Brute force sensitivity analysis is carried out to understand the influence of various reaction parameters on the formation of sulfur. It is found that the sticking and desorption reactions of H_2S are the most influential ones. An increase in sticking coefficient and decrease in the pre-exponential factor for desorption reaction facilitates the formation of surface adsorbed sulfur. The only adjustable parameter used in the simulations is the surface area available per unit volume A_{v0}. The model is able to predict accurately the time on stream drop in CH_4 conversions and the product mole fractions at the reactor exit. At high temperature, the deactivation profiles are very well predicted. Analysis of the fractional coverages along the reactor length reveals that during the initial stages of poisoning, the sulfur coverages are high near the reactor inlet. However, during the later stages, the surface coverage of sulfur increase towards the reactor exit. Since our experiments are conducted at one fixed composition the predictive capability of the kinetic model is further confirmed by simulating the experiments reported by Ashrafi et al. [23], which are performed for a different composition. The model also qualitatively predicts the recovery of the catalyst activity on removal of H_2S and temperature enhancement. At high temperature, the deactivation profiles are very well predicted, however, predicts slow recovery of the catalyst as opposed to experimental observation. In general the model is capable of predicting reforming of H_2S free biogas in the temperature range from 873-1200 K. However, the transients of deactivation are validated only in the temperature range of 973-1173 K and H_2S compositions from 20-50 ppm in the feed stream. Finally, although for a different composition, the model predicted saturation coverages are comparable to experimentally observed values.

Table 6.2: Detailed kinetic model for reforming of Biogas

R No	Reaction	A(cm,mol,s)	β	E_a [a]
R1	H_2 + (Ni) + (Ni) → H(Ni) + H(Ni)	0.01[b]	0	0
R2	O_2 +(Ni) +(Ni) → O(Ni) +O(Ni)	0.01[b]	0	0
R3	CH_4 +(Ni) → CH_4(Ni)	0.008[b]	0	0
R4	H_2O +(Ni) → H_2O(Ni)	0.1[b]	0	0
R5	CO_2 +(Ni) → CO_2(Ni)	1×10^{-05}[b]	0	0
R6	CO +(Ni) → CO(Ni)	0.5[b]	0	0
R7	H_2S +(Ni) → H_2 S(Ni)	0.6[b]	0	0
R8	SO_2 +(Ni) → SO_2(Ni)	0.02[b]	0	0
R9	H(Ni) +H(Ni) → (Ni) +(Ni) +H_2	2.676×10^{19}	0	81.40
R10	O(Ni) +O(Ni) → (Ni) +(Ni) +O_2	4.143×10^{23}	0	474.93
R11	CH_4(Ni) → (Ni) +CH_4	8.386×10^{15}	0	37.46
R12	H_2O(Ni) → (Ni) +H_2O	3.823×10^{12}	0	60.78
R13	CO_2(Ni) → (Ni) +CO_2	6.483×10^{07}	0	25.95
R14	CO(Ni) → (Ni) +CO	3.677×10^{11}	0	111.39
		$\epsilon_{CO(s)}$ [c]		-50
R15	O(Ni) +H(Ni) → OH(Ni) +(Ni)	5×10^{22}	0	97.90
R16	OH(Ni) +(Ni) → O(Ni) +H(Ni)	1.793×10^{21}	0	36.14
R17	OH(Ni) +H(Ni) → H_2O(Ni) +(Ni)	3×10^{20}	0	42.70
R18	H_2O(Ni) +(Ni) → OH(Ni) +H(Ni)	2.251×10^{21}	0	91.79
R19	OH(Ni) +OH(Ni) → O(Ni) +H_2O(Ni)	3×10^{21}	0	100.00
R20	O(Ni) +H_2O(Ni) → OH(Ni) +OH(Ni)	6.276×10^{23}	0	210.85
R21	O(Ni) +C(Ni) → CO(Ni) +(Ni)	5.2×10^{23}	0	148.10
R22	CO(Ni) +(Ni) → O(Ni) +C(Ni)	1.344×10^{22}	-3	116.06
		$\epsilon_{CO(s)}$ [c]		-50
R23	O(Ni) +CO(Ni) → CO_2(Ni) +(Ni)	2×10^{19}	0	123.60
		$\epsilon_{CO(s)}$ [c]		-50
R24	CO_2(Ni) +(Ni) → O(Ni) +CO(Ni)	4.627×10^{23}	-1	89.35
R25	HCO(Ni) +(Ni) → CO(Ni) +H(Ni)	3.7×10^{21}	0	0.00
		$\epsilon_{CO(s)}$ [c]		50
R26	CO(Ni) +H(Ni) → HCO(Ni) +(Ni)	3.903×10^{20}	-1	132.20
R27	HCO(Ni) +(Ni) → O(Ni) +CH(Ni)	3.7×10^{24}	-3	95.80
R28	O(Ni) +CH(Ni) → HCO(Ni) +(Ni)	4.741×10^{20}	0	110.00
R29	CH_4(Ni) +(Ni) → CH_3(Ni) +H(Ni)	3.7×10^{21}	0	57.70
R30	CH_3(Ni) +H(Ni) → CH_4(Ni) +(Ni)	5.903×10^{21}	0	61.51
R31	CH_3(Ni) +(Ni) → CH_2(Ni) +H(Ni)	3.7×10^{24}	0	100.00
R32	CH_2(Ni) +H(Ni) → CH_3(Ni) +(Ni)	1.265×10^{23}	0	55.26
R33	CH_2(Ni) +(Ni) → CH(Ni) +H(Ni)	3.7×10^{24}	0	97.10

[a] Arrhenius parameters for the rate constants written in the form: k = AT^{β} exp(-E_a/RT) The units of A are given in terms of moles, centimeters, and seconds. E_a is in kJ/mol

[b] Sticking coefficient. Total available surface site density is $\Gamma=2.66\times10^{-9}$ mol/cm^2

[c] Coverage dependent activation energy

R34	CH(Ni) +H(Ni) → CH_2(Ni) +(Ni)	4.001×10^{24}	0	79.11
R35	CH(Ni) +(Ni) → C(Ni) +H(Ni)	3.7×10^{21}	0	18.80
R36	C(Ni) +H(Ni) → CH(Ni) +(Ni)	4.529×10^{22}	0	161.06
R37	O(Ni) +CH_4(Ni) → CH_3(Ni) +OH(Ni)	1.7×10^{24}	0	88.30
R38	CH_3(Ni) +OH(Ni) → O(Ni) +CH_4(Ni)	9.728×10^{22}	0	30.35
R39	O(Ni) +CH_3(Ni) → CH_2(Ni) +OH(Ni)	3.7×10^{24}	0	130.10
R40	CH_2(Ni) +OH(Ni) → O(Ni) +CH_3(Ni)	4.538×10^{21}	0	23.60
R41	O(Ni) +CH_2(Ni) → CH(Ni) +OH(Ni)	3.7×10^{24}	0	126.80
R42	CH(Ni) +OH(Ni) → O(Ni) +CH_2(Ni)	1.435×10^{23}	0	47.05
R43	O(Ni) +CH(Ni) → C(Ni) +OH(Ni)	3.7×10^{21}	0	48.10
R44	C(Ni) +OH(Ni) → O(Ni) +CH(Ni)	1.624×10^{21}	0	128.60
R45	H_2S(Ni) → H_2S +(Ni)	1.108×10^{10}	-0.8	69.47
R46	SO_2(Ni) → SO_2 +(Ni)	2.709×10^{09}	0	102.50
R47	H_2S(Ni) +(Ni) → SH(Ni) +H(Ni)	5.5×10^{4}	1.2	29.31
R48	SH(Ni) +H(Ni) → H_2S(Ni) +(Ni)	1.291×10^{13}	0	106.19
R49	SH(Ni) +(Ni) → S(Ni) +H(Ni)	7.9×10^{11}	0	25.79
R50	S(Ni) +H(Ni) → SH(Ni) +(Ni)	6.375×10^{15}	0	142.94
R51	SH(Ni) +OH(Ni) → H_2S(Ni) +O(Ni)	1.053×10^{13}	0	29.72
R52	H_2S(Ni) +O(Ni) → SH(Ni) +OH(Ni)	8×10^{11}	-0.5	27.84
R53	S(Ni) +O(Ni) → SO(Ni) +(Ni)	1×10^{18}	1	296.82
R54	SO(Ni) +(Ni) → S(Ni) +O(Ni)	1.775×10^{12}	0	0.00
R55	SH(Ni) +O(Ni) → SO(Ni) +H(Ni)	1×10^{14}	-1	206.05
R56	SO(Ni) +H(Ni) → SH(Ni) +O(Ni)	2.115×10^{5}	0	0
R57	S(Ni) +OH(Ni) → SO(Ni) +H(Ni)	1×10^{21}	1	229.02
R58	SO(Ni) +H(Ni) → S(Ni) +OH(Ni)	3.352×10^{23}	-2.0	0.00
R59	SO_2(Ni) +(Ni) → SO(Ni) +O(Ni)	1×10^{18}	-0.5	106.31
R60	SO(Ni) +O(Ni) → SO_2(Ni) +(Ni)	9.029×10^{09}	1.5	0.00
R61	S(Ni) +H_2O(Ni) → SH(Ni) +OH(Ni)	1×10^{10}	0	143.37
R62	SH(Ni) +OH(Ni) → S(Ni) +H_2O(Ni)	1.652×10^{5}	0	0.00
R63	SH(Ni) +CO(Ni) → S(Ni) +HCO(Ni)	1.0×10^{4}	0	61.82
		$\epsilon_{CO(s)}$[c]		-50
R64	S(Ni) +HCO(Ni) → SH(Ni) +CO(Ni)	1.991×10^{12}	0	54.55
R65	SH(Ni) +CO(Ni) → SO(Ni) +CH(Ni)	1×10^{23}	0	223.41
		$\epsilon_{CO(s)}$[c]		-50
R66	SO(Ni) +CH(Ni) → SH(Ni) +CO(Ni)	3.066×10^{28}	0	0
R67	S(Ni) +CO(Ni) → SO(Ni) +C(Ni)	1×10^{13}	0	206.12
		$\epsilon_{CO(s)}$[c]		-50
R68	SO(Ni) +C(Ni) → S(Ni) +CO(Ni)	4.651×10^{15}	0	0

Chapter 7

Summary and outlook

Conventional fossil fuel reserves are limited and are being depleted at a faster rate, and the production and use of conventional fuels have adverse environmental impacts. Researchers are striving hard to replace conventional fuels with renewable fuels. In the recent past biogas systems have received considerable attention as an attractive source of renewable fuel, that is clean, environment friendly, and cheap. Biogas technology offers a very attractive route for decentralized applications in rural areas for meeting the energy needs. Biogas is an ideal gas for distributed power generation using Solid-Oxide Fuel Cells (SOFC). However, one of the major challenges in utilizing biogas for any applications is presence of H_2S. For example, the presence of H_2S or other sulfur containing compounds is a major problem for reforming of biogas due to its poisoning effect on most transition metals.

In this study, catalyst deactivation and regeneration during the biogas reforming on Ni catalyst was investigated. For consistent results,the catalysts were prepared in one batch and used throughout the experiments. In general, Ni catalysts showed better activity and stability during biogas steam reforming in non poisoning atmosphere. No obvious catalyst deactivation or carbon formation was observed during the stability experiments at 700 and 800 °C.

The deactivation studies were performed at three different H_2S concentrations(20, 50, and 100 ppm) and two different temperatures (700 and 800 °C). It was found that even low concentration (20 ppm) of H_2S in the feed can completely poison the catalyst at 700 °C, whereas at 800 °C the catalyst maintained some residual activity. It was found that the rate of deactivation depends on the H_2S concentration in the feed and operating temperature. Lower operating temperature and higher H_2S concentration leads to faster deactivation of the catalyst. At 800 °C, the activity of the catalyst was partially recovered just by removing H_2S from the feed gas. However, this method did not recover the catalyst activity at 700 °C. The acivity of the poisoned catalyst at 700 °C can be effectively recovered by increasing the temperature or steam treatment. In conclusion, with in the scope of this thesis, application of high temperatures was identified as the only effective means to enhance the sulphur resistance of nickel catalysts.

The experimental results were further used to develop a micro-kinetic model of biogas steam reforming in the presence of H_2S. The detailed kinetic model contains 68 reactions among 8 gas-phase species and 18 surface adsorbed species including the catalytic surface. The model can be used to simulate reforming

of biogas with and without H_2S in feed gas. The model was developed by fine tuning the pre-exponential factors to reproduce the experimental observations and entire mechanism was made thermodynamically consistent by using method described in Chapter 5. Brute force sensitivity analysis was carried out to study the influence of various kinetic parameters on formation of sulfur. The most sensitive reactions for the formation of adsorbed sulfur were the H_2S sticking reaction and H_2S desorption reaction. An increase in sticking coefficient resulted in higher sulfur coverage, whereas an increase in H_2S desorption pre-exponential factor resulted in lower sulfur coverage. In addition to these reactions, hydrogen abstraction reaction from H_2S and the reaction between adsorbed H_2S and O atom were also found to be influencing the formation of adsorbed sulfur. Increasing the pre-exponential factors of above reactions also resulted in faster deactivation.

The kinetic model was able to capture the time on stream behaviors of drop in CH_4 conversions and product mole fractions at the reactor exit. The model predicted that during the initial stages of poisoning sulfur coverages are high near the reactor inlet, however, as the reaction proceeds further sulfur coverages increase towards the reactor exit. At steady state the sulfur coverage increases asymptotically towards the reactor exit. The predictive capability of the kinetic model was further confirmed by simulating the experiments reported in the literature. In general the model was capable of predicting reforming of H_2S free biogas in the temperature range from 873-1200 K. However, the transients of deactivation were validated only in the temperature range of 973-1173 K and H_2S compositions from 20-50 ppm in the feed stream. Although, the kinetic model successfully predicts the deactivation on time on stream, it failed to predict the catalyst regeneration. The kinetic model model also predicted a linear decrease in sulfur coverage with increase in temperature, which were consistent with the experimental literature.

Future scope

The experiments were conducted at a fixed S/C ratio of 2.02. Due to the constant S/C ratio employed, it was not possible to assess the effect of H_2O on sulfur poisoning. Although, the kinetic model can be used to predict the influence of H_2O on saturation sulfur coverage, it needs to be validated. Therfore, one may extend these studies with varying S/C ratio. At a low S/C ratio and in the presence of H_2S catalyst may be deactivated simultaneously by carbon and sulfur species. Experiments were carried out only in the range of 20-100 ppm H_2S in the feed gas. This work may be further extended to study the Ni catalyst deactivation in the range of 1-20 ppm. Experiments at very low concentration of H_2S (1 ppm or even less) may be more useful to evaluate the performance of industrial reformers. Finally, In-situ studies concerning the interaction of sulfur with well defined metal and oxide surfaces should be conducted to elucidate changes in the structural, morphological, and electronic properties. Such studies will help in the better scientific design of catalysts, resistant to sulfur poisoning during the biogas reforming.

The present kinetic model has to be improved to capture regeneration in the concentration ranges studied. At present the model very well predicts catalyst deactivation in the range of 20-50 ppm H_2S concentration and qualitatively predicts the catalyst regeneration. One may extended this model to predict catalyst deactivation simultaneously with formation of carbon and sulfur species on the catalytic surface. It is worth mentioning that during the simulations it was found that, increasing the pre-exponential factor of the reaction S + CO $\rightleftharpoons$ SO + C leads to carbon and sulfur species formation on the catalytic surface.

References

[1] EPA, Climate Change Indicators in the United States, Tech. Rep. December, United States Environmental Protection Agency, USA (2012).

[2] UK Renewable Energy Roadmap, Tech. Rep. July, Department of Energy & Climate change, London (2011).

[3] S. Rasi, a. Veijanen, J. Rintala, Trace compounds of biogas from different biogas production plants, Energy 32 (2007) 1375–1380.

[4] Renewable energy sources, Tech. Rep. March, Federal Ministry for the Environment, Nature Conservation and Nuclear safety (2011).

[5] S. K. Singal, Review of augmentation of energy needs using renewable energy sources in India, Renewable Sustainable Energy Rev. 11 (2007) 1607–1615.

[6] A. Demirbas, Biofuels sources, biofuel policy, biofuel economy and global biofuel projections, Energy Convers. Manage. 49 (2008) 2106–2116.

[7] R. Alvarez, S. Villca, G. Liden, Biogas production from llama and cow manure at high altitude, Biomass Bioenergy 30 (2006) 66–75.

[8] J. Xuan, M. K. Leung, D. Y. Leung, M. Ni, A review of biomass-derived fuel processors for fuel cell systems, Renewable Sustainable Energy Rev. 13 (2009) 1301–1313.

[9] S. Delsinne, R. Nedelec, M. Riotte, O. Salvi, C. Thiébaut, Biogas safety & regulation, Tech. Rep. November, Ineris, Paris (2010).

[10] B. Agochukwu, The future roles of lanfill gas and biogas, Tech. Rep. December, Cranfield University (2010).

[11] A. Wellinger, A. Linberg, Biogas Upgrading and Utilization - IEA Bioenergy Task 24., Tech. rep. (2000).

[12] N. Muradov, Smith, Franklyn, Traissi, N. Muradov, A. T-Raissi, Hydrogen production by catalytic processing of renewable methane-rich gases, Int. J. Hydrogen Energy 33 (2008) 2023–2035.

[13] M. Benito, S. Garc, L. Garc, L. Daza, Development of biogas reforming Ni-La-Al catalysts for fuel cells , J. Power Sources 169 (2007) 177–183.

[14] P. Weiland, Biogas production: current state and perspectives., Appl. Microbiol. Biotechnol. 85 (2010) 849–60.

[15] G. Eliasson, Biogas as transportation fuel, Tech. rep., Swedish Biogas Association; SBGF, Stockholm (2010).

[16] T. Moulik, Biogas Program, Royal swedish academy of sciences 14 (2013) 288–292.

[17] G. Marbán, T. Valdés-Solís, Towards the hydrogen economy?, Int. J. Hydrogen Energy 32 (2007) 1625–1637.

[18] T. Shishido, M. Sukenobu, H. Morioka, M. Kondo, Y. Wang, K. Takaki, K. Takehira, Partial oxidation of methane over Ni/Mg-Al oxide catalysts prepared by solid phase crystallization method from Mg-Al hydrotalcite-like precursors, Appl. Catal., A: General 223 (2002) 35–42.

[19] M. Ratcliff, R. Bain, Fuel Cell Integration A Study of the Impacts of Gas Quality and Impurities Milestone, Tech. Rep. June, National Renwable Energy Laboratory, Department of Energy Laboratory, USA (2001).

[20] C. Bartholomew, Mechanisms of catalyst deactivation, Appl. Catal., A: General 212 (2001) 17–60.

[21] P. Forzatti, Catalyst deactivation, Catal. Today 52 (1999) 165–181.

[22] J. Butt, E. Petersen, Activation, deactivation and poisoning of catalysts, Academic press Inc, New York, 1988.

[23] M. Ashrafi, C. Pfeifer, T. Pro, H. Hofbauer, Experimental Study of Model Biogas Catalytic Steam Reforming : 2 . Impact of Sulfur on the Deactivation and Regeneration of Ni-Based Catalysts, Energy Fuels 22 (2008) 4190–4195.

[24] L. Li, C. Howard, D. L. King, M. Gerber, R. Dagle, D. Stevens, Regeneration of Sulfur Deactivated Ni-Based Biomass Syngas Cleaning Catalysts, Ind. Eng. Chem. Res. 49 (2010) 10144–10148.

[25] H. Özdemir, M. Faruk Öksüzömer, M. Ali Gürkaynak, Preparation and characterization of Ni based catalysts for the catalytic partial oxidation of methane: Effect of support basicity on H2/CO ratio and carbon deposition, International Journal of Hydrogen Energy 35 (22) (2010) 12147–12160.

[26] N. Tippayawong, P. Thanompongchart, Biogas quality upgrade by simultaneous removal of CO2 and H2S in a packed column reactor, Energy 35 (2010) 4531–4535.

[27] Capstone Turbine Corporation, The Capstone C30 MicroTurbine Generator (2002).

[28] L. Deng, H. Chen, Z. Chen, Y. Liu, X. Pu, L. Song, Process of simultaneous hydrogen sulfide removal from biogas and nitrogen removal from swine wastewater., Bioresour. Technol. 100 (2009) 5600–5608.

[29] S. McKinsey, Removal of Hydrogen Sulphide from Biogas using cow-manure compost., Ph.D. thesis, Cornell University, USA (2003).

[30] Laura Bailon, Jorgen Hinge, Biogas and bio-syngas upgrading, Tech. Rep. December, Danish technological institute, Denmark (2012).

[31] S. P. Hernández, M. Chiappero, N. Russo, D. Fino, A novel ZnO-based adsorbent for biogas purification in H2 production systems, Chem. Eng. J. 176-177 (2011) 272–279.

[32] M. Syed, G. Soreanu, P. Falletta, M. Béland, Removal of hydrogen sulfide from gas streams using biological processes - A review, Can. Biosyst. Eng. 48 (2006) 14.

[33] J. Rostrup-Nielsen, Syngas in perspective, Catal. Today 71 (2002) 243–247.

[34] S. Araki, N. Hino, T. Mori, S. Hikazudani, Autothermal reforming of biogas over a monolithic catalyst, Journal of Natural Gas Chemistry 19 (5) (2010) 477–481.

[35] S. Cimino, G. Landi, L. Lisi, G. Russo, Development of a dual functional structured catalyst for partial oxidation of methane to syngas, Catalysis Today 105 (3-4) (2005) 718–723.

[36] L. Li, D. L. King, H2S removal with ZnO during fuel processing for PEM fuel cell applications, Catalysis Today 116 (4) (2006) 537–541.

[37] D. Sun, X. Li, S. Ji, L. Cao, Effect of O2 and H2O on the tri-reforming of the simulated biogas to syngas over Ni-based SBA-15 catalysts, J. Nat. Gas Chem. 19 (2010) 369–374.

[38] O. A. Bereketidou, M. A. Goula, Biogas reforming for syngas production over nickel supported on ceria alumina catalysts, Catal. Today 195 (2012) 93– 100.

[39] J. Richardson, S. Paripatyadar, Carbon dioxide reforming of methane with supported rhodium, Applied Catalysis 61 (1) (1990) 293–309.

[40] S. L. Lakhapatri, M. a. Abraham, Analysis of catalyst deactivation during steam reforming of jet fuel on Ni-(PdRh)/γ-Al2O3 catalyst, Appl. Catal., A 405 (2011) 149–159.

[41] N. Lakshminarayanan, U. S. Ozkan, Effect of H2O on sulfur poisoning and catalytic activity of NiYSZ catalysts, Applied Catalysis A: General 393 (1-2) (2011) 138–145.

[42] A. Erdhelyi, A. ErdÅhelyi, K. Fodor, T. s. Szailer, Effect of H2S on the reaction of methane with carbon dioxide over supported Rh catalysts, Appl. Catal., B 53 (2004) 153–160.

[43] A. Effendi, Z. Zhang, K. Hellgardt, K. Honda, T. Yoshida, Steam reforming of a clean model biogas over Ni/Al2O3 in fluidized- and fixed-bed reactors, Catal. Today 77 (2002) 181–189.

[44] A. Effendi, K. Hellgardt, Z. Zhang, T. Yoshida, Optimising H2 production from model biogas via combined steam reforming and CO shift reactions, Fuel 84 (2005) 869–874.

[45] P. Kolbitsch, C. Pfeifer, H. Hofbauer, Catalytic steam reforming of model biogas, Fuel 87 (2008) 701–706.

[46] S. Araki, N. Hino, T. Mori, S. Hikazudani, Durability of a Ni based monolithic catalyst in the autothermal reforming of biogas, Int. J. Hydrogen Energy 34 (2009) 4727–4734.

[47] S. Araki, N. Hino, T. Mori, S. Hikazudani, Start-up procedures in autothermal reforming of biogas over a Ni based catalytic monolith, Catal. Commun. 10 (2009) 1300–1304.

[48] J. Xu, W. Zhou, Z. Li, J. Wang, J. Ma, Biogas reforming for hydrogen production over nickel and cobalt bimetallic catalysts, Int. J. Hydrogen Energy 34 (2009) 6646–6654.

[49] J. Xu, W. Zhou, Z. Li, J. Wang, J. Ma, Biogas reforming for hydrogen production over a NiCo bimetallic catalyst: Effect of operating conditions, Int. J. Hydrogen Energy 35 (2010) 13013–13020.

[50] A. F. Lucrédio, J. M. Assaf, E. M. Assaf, Reforming of a model biogas on Ni and Rh Ni catalysts : Effect of adding La, Fuel Process. Technol. 102 (2012) 124–131.

[51] U. Izquierdo, V. L. Barrio, J. Requies, J. F. Cambra, M. B. Gu, P. L. Arias, Tri-reforming : A new biogas process for synthesis gas and hydrogen production, Int. J. Hydrogen Energy 38 (2012) 7623–7631.

[52] J. R. Rostrup-nielsen, Some principals relating to the regeneration of sulfur poisoned nickel catalysts, J. Catal. 21 (1971) 171–178.

[53] J. h. Wang, M. Liu, Surface regeneration of sulfur-poisoned Ni surfaces under SOFC operation conditions predicted by first-principles-based thermodynamic calculations, J. Power Sources 176 (2008) 23–30.

[54] N. S. Nasri, J. M. Jones, V. A. Dupont, A. Williams, A Comparative Study of Sulfur Poisoning and Regeneration of Precious-Metal Catalysts, Energy 12 (1998) 1130–1134.

[55] J. Rostrup-Nielsen, Catalytic Steam Reforming, in: M. Anderson, JohnR and Boudart (Ed.), Catalysis, Springer, Heidelberg, 1984, pp. 1–117.

[56] C. H. Bartholomew, P. K. Agrawal, J. R. Katzer, Sulfur Poisoning of Metals, Vol. 31 of Advances in Catalysis, Academic Press, 1982, pp. 135–242.

[57] E. J. Erekson, C. H. Bartholomrw, Sulfur poisoning of nickel methanation catalysts: II. Effects of H2S concentration, CO and H2O partial pressures and temperature on reactivation rates, Appl. Catal., A 5 (1983) 323–336.

[58] A. D. Moeller, C. H. Bartholomew, Deactivation by Carbon of Nickel, Nickel-Ruthenium, and Nickel-Molybdenum Methanation Catalysts, Ind. Eng. Chem. Prod. Res. Dev., 21 (1982) 390–397.

[59] J. Rostrup Nielsen, Coking on nickel catalysts for steam reforming of hydrocarbons, J. Catal. 33 (1974) 184–201.

[60] D. L. Trimm, Catalyst design for reduced coking (review), Appl. Catal., 5 (1983) 263–290.

[61] J. R. Rostrup Nielsen, J. H. B. Hansen, CO2-Reforming of Methane over Transition Metals, J. Catal. 144 (1993) 38–49.

[62] S. Katta, D. L. Kealrns, Study of Kinetics of Carbon Gasification Reactions, Ind. Eng. Chem. Fundam., 20 (1981) 6–13.

[63] D. Trimm, Catalysts for the control of coking during steam reforming, Catal. Today 49 (1999) 3–10.

[64] Trimm;DL, Formation and removal of coke from nickel catalyst, Cat. Rev. - Sci. Eng. 16 (1977) 155–189.

[65] R. W. B. Engle, C.J, Hydrogen Transfer over Silica- Alumina catalysts, Ind. Eng. Chem. Res. 43 (2) (1951) 494–501.

[66] A. T. Ashcroft, A. K. Cheetham, M. L. H. Green, P. D. F. Vernon, Partial oxidation of methane to synthesis gas using carbon dioxide, Nature 352 (1991) 225–226.

[67] V. Choudhary, K. Mondal, T. Choudhary, Methane reforming over a high temperature stable-NiCoMgOx supported on zirconiahafnia catalyst, Chem. Eng. J. 121 (2006) 73–77.

[68] S. M. Augustine, G. N. Alameddin, W. M. H. Sachtler, The effect of Re, S, and Cl on the deactivation of Ptγ-Al2O3 reforming catalysts, J. Catal. 115 (1989) 217–232.

[69] Jens Rostrup-Nielsen, Mechanisms of Carbon Formation, J. Catal. 48 (1977) 155– 165.

[70] G. Froment, Modeling of catalyst deactivation, Appl. Catal., A 212 (2001) 117–128.

[71] A. O. E. Beyne, G. F. Froment, A percolation approach for the modeling of deactivation of zeolite catalysts by coke formation: diffusional limitations and finite rate of coke growth, Chem. Eng. Sci. 48 (1993) 503–511.

[72] L. Gruber, B. Y. H. L. Gruber, Chemisorption studies on supported platinum, J. Phys. Chem. 66 (1980) 48–54.

[73] R. W. Misson, C. A. Mims, B. A. Saville, Chemical Reaction Engineering and Kinetics, John wiley and Sons, Inc, New York, 1999.

[74] D. L. Trimm, Thermal Stability of Catalyst Supports, in: C. H. Bartholomew, J. B. Butt (Eds.), Catalyst Deactivation 1991 Proceedings of the 5th International Symposium, Vol. 68 of Stud. Surf. Sci. Catal., Elsevier, 1991, pp. 29–51.

[75] F. Abild-pedersen, O. Lytken, J. Engbae k, G. Nielsen, I. Chorkendorff, J. K. Norskov, Methane activation on Ni (1 1 1): Effects of poisons and step defects, Surf. Sci. 590 (2005) 127–137.

[76] J. Rostrup-Nielsen, Sulfur-passivated nickel catalysts for carbon-free steam reforming of methane, J. Catal. 85 (1984) 31–43.

[77] J. Biswas, G. M. Bickle, P. G. Gray, D. D. Do, The Role of Crystallite Structure on Mechanisms of Coke and Sulphur Poisoning in Catalytic Reforming, in: B. Delmon, G. F. Froment (Eds.), Studies in Surface Science and Catalysis, Vol. 34 of Studies in Surface Science and Catalysis, Elsevier, 1987, pp. 553–565.

[78] P. Marecot, E. Paraiso, J. Dumas, J. Barbier, Deactivation of nickel catalysts by sulphur compoundsII. Chemisorption of hydrogen sulphide, Appl. Catal., A 80 (1992) 89–97.

[79] L. Oliphant, R. W. Fowler, R. B. Pannell, C. H. Bartholomew, Chemisorption of Hydrogen Sulfide on Nickel and Ruthenium Catalysts I. Desorption Isotherms, J. Catal. 242 (1978) 229–242.

[80] J. R. Rostrup-nielsen, Chemisorption of H2S on a Supported Nickel catalyst, Journal of Catalysis 11 (1968) 220–227.

[81] J. Rostrup-Nielsen, High Temperature Hydrogen Sulfide Chemisorption on Nickel Catalysts, Appl. Catal., 1 (1981) 303–314.

[82] A. Erdhelyi, Effect of H2S on the reaction of methane with carbon dioxide over supported Rh catalysts, Appl. Catal., B 53 (3) (2004) 153–160.

[83] C. R. Apesteguía, J. Barbier, The role of catalyst presulfurization in some reactions of catalytic reforming and hydrogenolysis, J. Catal. 78 (1982) 352–359.

[84] J. A. Moulijn, A. E. V. Diepen, F. Kapteijn, Catalyst deactivation : is it predictable ? What to do ?, Appl. Catal., A 212 (2001) 3–16.

[85] R. I. Hegde, J. M. White, Chemisorption and Decomposition of H2S on Rh(100), J. Phys. Chem. 90 (1986) 296–300.

[86] D. Huntley, The reaction of H2S with surface oxygen on Ni(110), Surf. Sci. 240 (1990) 24–36.

[87] J. Andersen, Adsorption of H2S on Ni(100): Kinetics and structure, Surf. Sci. 192 (1987) 583–596.

[88] J. Y. Zhou, Chemisorption of H2S on clean and S-, D- and O-covered Ni(100) *, Surf. Sci. 183 (1987) 363–376.

[89] R. I. Hegde, J. M. White, Chemisorption and Decomposition of H2S on Rh(100), J. Phys. Chem. 78712 (1986) 296–300.

[90] D. R. Alfonso, Surface Science First-principles studies of H2S adsorption and dissociation on metal surfaces, Surf. Sci. 602 (2008) 2758–2768.

[91] I. D. Besten, P. Selwood, The Chemisorption of Hydrogen Sulfide, Methyl Sulfide, and Cyclohexene on Supported Nickel Catalysts, J. Catal. 1 (1962) 93–102.

[92] M. Twigg, Catalyst handbook, 2nd Edition, Monson Publications, London, 1996.

[93] B. Roy, K. Loganathan, H. Pham, a.K. Datye, C. Leclerc, Surface modification of solution combustion synthesized Ni/Al2O3 catalyst for aqueous-phase reforming of ethanol, Int. J. Hydrogen Energy 35 (2010) 11700–11708.

[94] A. Cimino, M. Lo Jacono, M. Schiavello, Structural, magnetic, and optical properties of nickel oxide supported on .eta.- and .gamma.-aluminas, J. Phys. Chem. 75 (1971) 1044–1050.

[95] J. N. Kuhn, N. Lakshminarayanan, U. S. Ozkan, Effect of hydrogen sulfide on the catalytic activity of Ni-YSZ cermets, J. Mol. Catal. A: Chem. 282 (2008) 9–21.

[96] J. Chen, R. Wang, J. Zhang, F. He, S. Han, Effects of preparation methods on properties of Ni/CeO2Al2O3 catalysts for methane reforming with carbon dioxide, Journal of Molecular Catalysis A: Chemical 235 (2005) 302–310.

[97] C. E. Quincoces, A. Diaz, M. Montes, E. N. Ponzi, M. G. Gonzalez, CO2 reforming of methane. Effect of NiSiO2 interactions on carbon deposition, in: G. W. R. J.J. Spivey, B. H. Davis (Eds.), Catalyst Deactivation 2001 Proceedings of the 9th International Symposium, Vol. 139 of Studies in Surface Science and Catalysis, Elsevier, 2001, pp. 85–92.

[98] A. Aguinaga, J. C. D. L. Cal, J. M. Asúa, M. Montes, Effect of the preparation on the activity and selectivity of supported nickel catalysts, Appl. Catal., 51 (1989) 1–11.

[99] O. Deutschmann, S. Tischer, V. M. Janardhanan, C. Correa, D. Chatterjee, N. Mladenov, H. D. Minh, DETCHEM User manual, Tech. rep., University of Karlsruhe, Karlsruhe (2007).

[100] J. R. Rostrup-Nielsen, Some principles relating to the regeneration of sulfur-poisoned nickel catalyst, J. Catal. 21 (1971) 171–178.

[101] V. M. Janardhanan, A Detailed Approach to Model Transport, Heterogeneous Chemistry, and Electrochemistry in Solid-Oxide Fuel Cells, Ph.D. thesis, KIT, Germany (2007).

[102] R. Van Santen, M. Neurock, Molecular heterogeneous catalysis, WILEY-VCHVerlag GmbH & Co. KGaA, Weinheim, 2006.

[103] O. Deutschmann, Interactions between transport and chemistryin catalytic reactors, Ph.D. thesis, Fakultat fur Chemie der Ruprecht-Karls-Universit, Heidelberg, habilitation thesis (2001).

[104] R. J. Kee, M. E. Coltrin, P. Glarborg, Chemically reacting flow: Theory and Practice, John Wiley & Sons, 2003.

[105] S. Appari, V. M. Janardhanan, S. Jayanti, L. Maier, S. Tischer, O. Deutschmann, Micro-kinetic modeling of NH3 decomposition on Ni and its application to solid oxide fuel cells, Chem. Eng. Sci. 66 (2011) 5184–5191.

[106] V. M. Janardhanan, O. Deutschmann, Modeling of Solid-Oxide Fuel Cells, Z. Phys. Chem 221 (2007) 443–478.

[107] V. M. Janardhanan, O. Deutschmann, Modeling diffusion limitation in solid-oxide fuel cells, Electrochim. Acta 56 (2011) 9775–9782.

[108] K. Y. Kung, P. Chen, F. Wei, Y. R. Shen, G. A. Somorjai, Sum-frequency generation spectroscopic study of {CO} adsorption and dissociation on Pt(111) at high pressure and temperature, Surf. Sci. 463 (2000) L627 – L633.

[109] A. B. Mhadeshwar, H. Wang, D. G. Vlachos, Thermodynamic Consistency in Microkinetic Development of Surface Reaction Mechanisms, J. Phys. Chem. B 107 (2003) 12721–12733.

[110] D. Mantri, P. Aghalayam, Detailed surface reaction mechanism for reduction of NO by CO, Catal. Today 119 (2007) 88–93.

[111] E. Shustorovich, H. Sellers, The UBI-QEP method: A practical theoretical approach to understanding chemistry on transition metal surfaces, Surf. Sci. Rep. 31 (1998) 1–119.

[112] M. Head gordon, Quantum Chemistry and Molecular Processes, J. Phys. Chem. 100 (1996) 13213–13225.

[113] P. Olivera, E. Patrito, H. Sellers, Direct synthesis of methanol over metallic catalysts, Surf. Sci. 327 (1995) 330–357.

[114] E. Shustorovich, A. T. Bell, An analysis of methanol synthesis from CO and CO , on Cu and Pd surfaces by the bond-order-conservation-Morse-potential approach, Surf. Sci. 253 (1991) 386–394.

[115] P. Olivera, E. M. Patrito, H. Sellers, Hydrogen peroxide synthesis over metallic catalysts, Surf. Sci. 313 (1994) 25–40.

[116] E. Shustorovich, A. T. Bell, Synthesis and decomposition of ammonia on transition metal surfaces :, Surf. Sci. 259 (2001) 0–5.

[117] E. Shustorovich, A. T. Bell, Decomposition and reduction of NO on transition metal surfaces: bond order conservation Morse potential analysis, Surf. Sci. 289 (1993) 127–138.

[118] M. Moqadam, M. Rahmani, Z. Karimi, a. Naderifar, A UBI-QEP Microkinetic Study for Fischer-Tropsch Synthesis on Iron Catalysts, Procedia Eng. 42 (2012) 34–44.

[119] E. Shustorovich, A. T. Bell, An analysis of Fischer-Tropsch synthesis by the bond-order-conservation-Morse-potential approach, Surf. Sci. 248 (3).

[120] H. Seller, Coordination modes and bonding of sulfur oxides on transition metal surfaces: combined ab initio and BOC-MP results, Surface Science 346 (1996) 322–336.

[121] H. Sellers, E. Shustorovich, Chemistry of sulfur oxides on transition metal surfaces: a bond order conservation-Morse potential modeling perspective, Surf. Sci. 356 (1996) 209–221.

[122] A. Bell, Theory and Applications to Heterogeneous Catalysis, Chemisorption, and Surface Diffusion, shustorovich, evgeny (ed.) Edition, VCH Publishers, Inc., 1991.

[123] E. Shustrovich, The Bond-Order Conservation Approach to Chemisorption and Heterogeneous Catalysis: Applications and Implications, Adv. Catal. 37 (1990) 101–163.

[124] D. R. Huntley, The decomposition of H2S on Ni (110), Surf. Sci. 240 (1990) 13–23.

[125] H. Sellers, E. Shustorovich, Chemistry of sulfur oxides on transition metal surfaces : BOC-MP analysis, J. Mol. Catal. A 119 (1997) 367–375.

[126] R. D. Cortright, J. A. Dumesic, Kinetics of Heterogeneous Catalytic Reactions : Analysis, Advances In Catalysis 46 (2001) 161–264.

[127] J. A. Dumesic, D. F. Rudd, L. M. Aparicio, J. E. Rekoske, A. A. Trevino, The Microkinetics of heterogeneous catalysis, ACS Professional Reference Book, Washington, DC, 1993.

[128] P. Stoltze, Microkinetic simulation of catalytic reactions irreversible step, Prog. Surf. Sci. 65 (2000) 65–150.

[129] P. Aghalayam, Y. K. Park, D. G. Vlachos, Construction and optimization of complex surface-reaction mechanisms, AIChE Journal 46 (2000) 2017–2029.

[130] G. Schmitz, Thermodynamic consistency of reaction mechanisms and null cycles, J. Chem. Phys. 112 (2000) 10714.

[131] L. Maier, B. Schadel, K. Herrera Delgada, S. Tisher, O. Deutchmann, Steam Reforming of Methane Over Nickel : Development of a Multi-Step Surface Reaction Mechanism, Top. Catal. (2011) 845–858.

[132] V. M. Janardhanan, O. Deutschmann, CFD analysis of a solid oxide fuel cell with internal reforming : Coupled interactions of transport , heterogeneous catalysis and electrochemical processes, J. Power Sources 162 (2006) 1192–1202.

[133] R. B. Bird, W. E. Stewart, E. N. Lightfoot, Transport Phenomena, 2nd Edition, John Wiley & Sons, 2002.

[134] A. Hindmarsh, P. Brown, K. Grant, S. Lee, R. Serban, D. Shumaker, C. Woodward, SUNDIALS: Suite of nonlinear and differential/algebraic equation solvers, ACM Transactions on Mathematical Software 31 (2005) 363–396.

[135] J. R. Nielsen, Chemisorption of Hydrogen Sulfide on a supported nickel catalyst, J. Catal. 227 (1968) 220–227.

[136] M. Ashrafi, T. Proll, C. Pfeifer, H. Hofbauer, Experimental Study of Model Biogas Catalytic Steam Reforming : 1 . Thermodynamic Optimization, Energy Fuels 22 (2008) 4182–4189.

[137] J. R. Rostrup-nielsen, J. B. Hansen, S. Helveg, N. Christiansen, A. Jannasch, Sites for catalysis and electrochemistry in solid oxide fuel cell (SOFC) anode, Appl. Phys.A: Material Science and Processing 85 (2006) 427–430.

List of Publications

Refereed journal papers

1. Srinivas Appari, Vinod M. Janardhanan, Ranjit Bauri, Sreenivas Jayanti, and Olaf Deutchmann, A detailed kinetic model for biogas steam reforming on Ni and catalyst deactivation due to sulfur poisoning. Appl. Catal., A (471) 118-125 (2014).

2. Srinivas Appari, Vinod M. Janardhanan, Ranjit Bauri, and Sreenivas Jayanti, Deactivation and regeneration of Ni catalyst during steam reforming of model biogas: An experimental investigation. Int. J. Hydrogen. Energy (39) 297-304 (2014).

3. Srinivas Appari, Vinod M. Janardhanan, Sreenivas Jayanti, Steffen Tischer and Olaf Deutschmann, Micro-kinetic modeling of NH_3 decomposition on Ni and its application to solid-oxide fuel cells. Chem. Eng. Sci. (66) 21, 5184-5191 (2011).

4. Vinod M. Janardhanan, Srinivas Appari, Sreenivas Jayanti and Olaf Deutschmann, Numerical study of on-board fuel reforming in a catalytic plate reactor for solid-oxide fuel cells. Chem. Eng. Sci.(66) 3, 490-498 (2011).

International conference papers

1. Srinivas Appari, Olaf Deutschmann, Vinod M. Janardhanan, Microkinetic modeling of catalyst poisoning and regeneration during biogas reforming, ISCRE-22, Spt. 2-5, 2012, Maastricht, The Netherlands.

2. Srinivas Appari, Vinod M. Janardhanan, and Sreenivas Jayanti, A detailed kinetic model for ammonia decomposition on Pt catalysts, Ist International Science Congress, Dec. 24-25, 2011, Indore, India.

3. Srinivas Appari, Vinod M. Janardhanan, and Sreenivas Jayanthi, Modeling of direct ammonia solid oxide fuel cells, International conference in Chemical Engineering, REACH, Dec.2- 4, 2010, IIT Madras.